Exploring Porphyrin Triads as Molecular Compasses

A Thesis submitted for the Honour School of Chemistry

Part II 2025

Sam Leggatt

Worcester College

Summary

The remarkable navigation of night-migratory songbirds, guided by their ability to sense the Earth's magnetic field, has inspired the development of biomimetic molecular compasses.[1] These compasses harness the evolution of a spin-correlated radical pair, generated through photoinduced electron transfer, to achieve highly sensitive and optically detectable magnetic sensing (Figure 1).[2] The typical compass structure, a donor-chromophore-acceptor triad, must meet a stringent set of criteria. Consequently, only one molecular compass that operates under Earth-strength fields has been reported.[2]

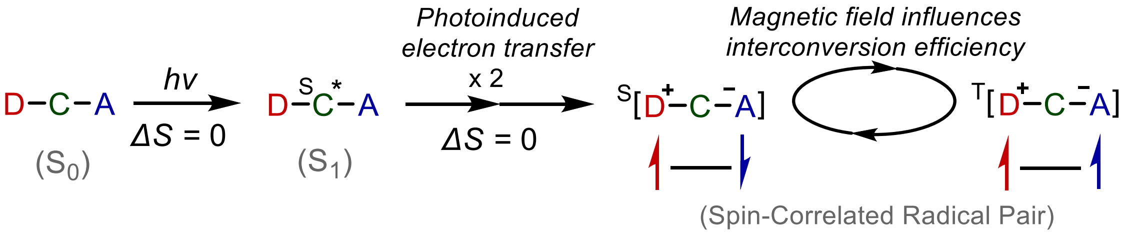

Figure 1 Simplified photochemical scheme for magnetic sensing using a spin-correlated radical pair. D-C-A = donor-chromophore-acceptor triad.

To guide the design of new molecular compasses, a broad range of triad components must be screened. Therefore, this thesis explores a modular approach to the synthesis and spectroscopic characterisation of molecular compass candidates, inspired by the axial assembly of aluminium porphyrin triads developed by Poddutoori, van der Est *et al.*[3]

Initially, an aluminium porphyrin triad was synthesised from three separate components (Figure 2). A fullerene-based electron acceptor was synthesised via the Prato reaction, and it reacted with the aluminium porphyrin in quantitative yield. A triarylamine donor was synthesised via successive Ullmann couplings. The binding of the donor to the aluminium porphyrin was monitored by UV-Vis titration (K_a = 2.7 x 10^6 M^{-1}).

In the triad, fluorescence was quenched relative to reference aluminium porphyrin complexes, which is consistent with photoinduced electron transfer. This conclusion was

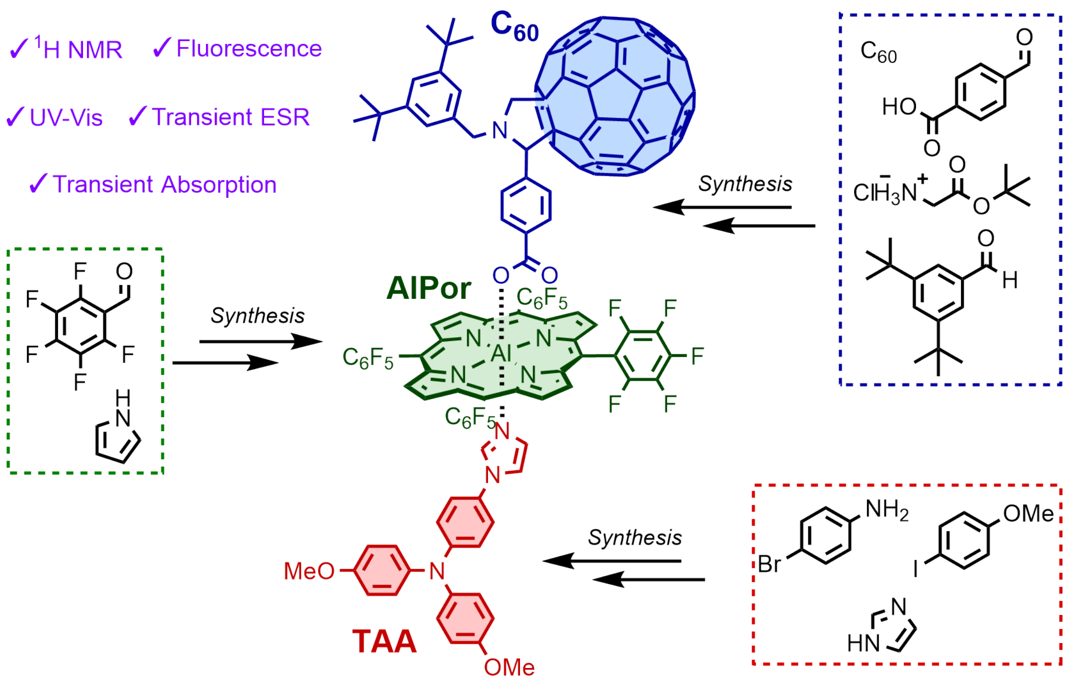

Figure 2 Structure of the final triad. The synthesis of each of the triad components is illustrated.

supported by transient absorption spectroscopy, which showed radical pair formation before rapid recombination (< 1 ns) at room temperature (Figure 3). The short radical pair lifetime makes this triad unsuitable for magnetic sensing. The rapid recombination was investigated by comparing the transient ESR spectra of porphyrin triplets. This revealed that the C_{60} acceptor is ineffective in the triad. By studying a series of dyads and reference complexes alongside the triad, this thesis demonstrates the value of modularity in both the synthesis and spectroscopic characterisation of molecular compass candidates.

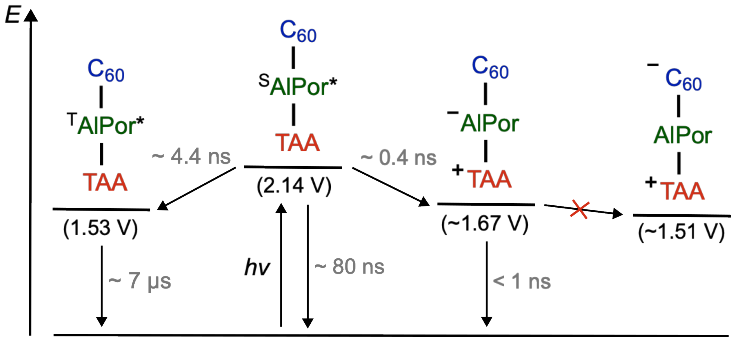

Figure 3 Energy level diagram for the triad, based on the results of this thesis. Literature redox potentials were used to estimate the energy levels.[3]

References

1. Hore, P. J.; Mouritsen, H., *Annu. Rev. Biophys.*, 2016, **45**, 299–344.
2. Kerpal, C *et al.*, *Nat. Commun.*, 2019, **10**, 3707.
3. Zarrabi, N. *et al.*, *J. Am. Chem. Soc.*, 2020, **142**, 10008–10024.

Acknowledgments

First of all, I would like to thank Professor Harry Anderson for giving me the opportunity to undertake my Part II in his group, and for his encouragement throughout the year. I am grateful for the patient guidance and support that he gave each week.

Thank you to all the members of the HLA group for creating a friendly and supportive lab environment. I am especially grateful to Lene Godde for her excellent day-to-day supervision and much-appreciated optimism. Likewise, I am very grateful to Dr Gabriel Moise for generously dedicating his time to our measurement sessions, and for teaching me about triplets, flame sealing and the importance of O-rings. Thank you to Dr Sili Qiu as well for his help with fluorescence, and to Jake Holmes, Edward Champness, Dr Kavita Rani, and my fellow Part II, Ross Clark, for many entertaining conversations.

I would also like to thank Professor Christiane Timmel for kindly allowing me to collaborate with her group and for the helpful advice she provided during the project. I am grateful to the welcoming members of her group, particularly Damyan Frantzov for teaching me about triads and measuring many compounds. Thank you also to Dr Kevin Henbest for his help with TA.

I am grateful for the brilliant memories that I have shared with my friends and fellow Worcester chemists over the past four years, and I would like to thank them all. Finally, I would like to thank my family and Manami for their love and support throughout my time in Oxford.

Supplement to Statement of Authorship

The transient absorption spectra presented in **Chapter 3** were measured by Damyan Frantzov and Dr Kevin Henbest (from the group of Professor Christiane Timmel, University of Oxford). The spectra were processed and analysed by Damyan Frantzov.

The transient electron spin resonance spectra presented in **Chapter 4** were measured, processed and simulated in collaboration with Dr Gabriel Moise and Damyan Frantzov (from the group of Professor Christiane Timmel, University of Oxford).

List of Abbreviations

A	Absorbance
A/E	Absorptive/Emissive
Ar	Aryl
CPF	Carotenoid-Porphyrin-Fullerene
CW	Continuous Wave
D-C-A	Donor-Chromophore-Acceptor
DDQ	2,3-Dichloro-5,6-dicyano-1,4-benzoquinone
DFT	Density Functional Theory
DMF	Dimethylformamide
ESI	Electrospray Ionisation
FT-IR	Fourier-Transform Infrared
HOMO	Highest Occupied Molecular Orbital
IRF	Instrument Response Function
ISC	Intersystem Crossing
J	Exchange Coupling Constant
λ	Wavelength
LUMO	Lowest Unoccupied Molecular Orbital
MALDI-TOF	Matrix-Assisted Laser Desorption/Ionization-Time Of Flight
MeIm	1-Methylimidazole
2-MeTHF	2-Methyltetrahydrofuran
MFE	Magnetic Field Effect
Ms	Total Spin Magnetic Quantum Number
NMR	Nuclear Magnetic Resonance
o-DCB	1,2-Dichlorobenzene
PET	Photoinduced Electron Transfer
Ph	Phenyl
py	Pyridine
QE	Quenching Efficiency
R_f	Retention Factor
RPM	Radical Pair Mechanism
S	Total Spin Quantum Number
SCRP	Spin-Correlated Radical Pair
TA	Transient Absorption
TCSPC	Time-Correlated Single Photon Counting
TFA	Trifluoroacetic Acid
THF	Tetrahydrofuran
TLC	Thin-layer Chromatography
TPN	Triarylamine-Palladium(II)porphodimethenato-Napthalenediimide
trESR	Transient Electron Spin Resonance
UV-Vis	Ultraviolet-Visible
ZFS	Zero-Field Splitting
δ	Chemical Shift

Table of Contents

Summary I

Acknowledgments III

Supplement to Statement of Authorship IV

List of Abbreviations V

1 Introduction 1

1.1 The Radical Pair Mechanism of Magnetoreception 1

1.2 Molecular Compasses 4

1.3 Aluminium Porphyrin Complexes 7

1.4 Project Aims and Molecular Design 11

2 Synthesis of an Aluminium Porphyrin Triad 12

2.1 Synthesis of Reference Complexes 12

2.2 Synthesis and Binding of the Fullerene Acceptor 15

2.2.1 Synthesis of **C_{60}COOH** 15

2.2.2 Attempted Condensation of **C_{60}COOH** *with* **AlPor^{t}BuOH** 16

2.2.3 Redesign and Synthesis of **C_{60}BnCOOH** 18

2.2.4 Binding of **C_{60}BnCOOH** 19

2.3 Synthesis and Binding of the Triarylamine Donor 22

2.3.1 Synthesis of **TAAIm** 22

2.3.2 Binding of **TAAIm** 23

3 Investigating Radical Pairs in Aluminium Porphyrin Complexes 25

3.1 Introduction to Fluorescence in Triads 25

3.2 Steady-State Fluorescence Spectroscopy 26

3.2.1 Mirror Image Emission Spectrum 26

3.2.2 Fluorescence Quenching in the Triad 26

3.2.3 Fluorescence Quantum Yields 30

3.3 Time-Correlated Single Photon Counting 31

3.4 Transient Absorption Spectroscopy 33

3.4.1 Introduction to TA Spectroscopy 33

3.4.2 **AlPorF$_{20}$C$_{60}$** (*Chromophore-Acceptor Dyad)* 33

3.4.3 **TAAIm-AlPorF$_{20}$C$_{60}$** (*Donor-Chromophore-Acceptor Triad)* 34

3.5 Summary and Discussion 35
4 Investigating Triplet States in Aluminium Porphyrin Complexes 37
4.1 Introduction to trESR 37
4.2 Triplet States in Aluminium Porphyrin Reference Complexes 40
*4.2.*1 **AlPorPh** 40
*4.2.*2 **AlPorF$_{20}$Ph** 42
4.3 Triplet States in Aluminium Porphyrin Dyads 44
4.3.1 **AlPorF$_{20}$C$_{60}$** *(Chromophore-Acceptor Dyad)* 44
4.3.2 **TAAIm-AlPorF$_{20}$C$_{60}$** *(Donor-Chromophore Dyad)* 46
4.4 Triplet States in an Aluminium Porphyrin Triad 47
4.5 Summary and Discussion 49
5 Conclusions 51
6 Experimental Procedures 52
6.1 General Methods 52
6.2 Synthetic Procedures 52
6.3 UV-Vis and Fluorescence Spectroscopy 58
6.4 Electron Spin Resonance Spectroscopy 58
Bibliography 59
Appendix I: Experimental Procedures for the Synthesis of Known Compounds .. 61
Appendix II: Characterisation Data of New Compounds 71
Appendix III: Supporting UV-Vis and trESR Spectra 78

1 Introduction

1.1 The Radical Pair Mechanism of Magnetoreception

Every autumn, night-migratory songbirds travel thousands of kilometres to their wintering sites, many of them making this journey for the first time.[1] Despite their unfamiliarity with the route, these young songbirds often travel alone and without training.[1] To accomplish this navigation these species use a number of orientational cues, including a compass-like sensitivity to the direction of the Earth's magnetic field.[2] The birds' ability to detect weak (50 μT) magnetic fields with high accuracy is remarkable. Therefore, avian magnetoreception is actively being researched for the biomimetic development of accurate, tunable and scalable magnetic sensors.

In the last 25 years, the radical pair mechanism (RPM), first proposed by Schulten (1978),[3] has emerged as the leading hypothesis for avian magnetoreception following research into both artificial systems and biological systems.[1] The RPM occurs in the cryptochrome photoreceptor protein, located in the birds' eyes, and involves the magnetic field-dependent evolution of a spin-correlated radical pair (SCRP).[3]

The RPM can be understood by considering a model triad system containing an electron donor (D), a chromophore (C) and an electron acceptor (A). While the RPM is somewhat different for molecular triads and cryptochromes, the general spin physics is similar. Upon photoexcitation, the chromophore is promoted to its excited singlet (S = 0) state due to the $\Delta S = 0$ selection rule. The singlet excited chromophore then undergoes stepwise photoinduced electron transfer (PET) to form a radical pair (Figure 1.1). If the

PET steps are fast on the timescale of spin dynamics, the total spin is conserved. In this case, the radical pair is generated in a singlet state and it is said to be spin-correlated.

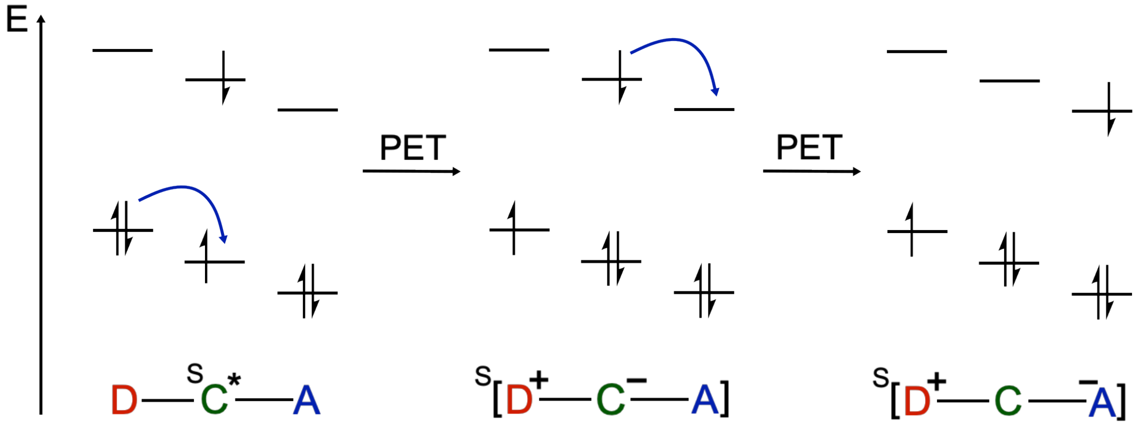

Figure 1.1 Energy level diagram for stepwise photoinduced electron transfer (PET) in a model donor-chromophore-acceptor system. Spin is conserved because the PET steps are faster than spin dynamics.

However, the singlet radical pair state is not an eigenstate of the spin Hamiltonian for two reasons: the spatially separated electrons in the SCRP have weak dipolar and exchange couplings; and each electron experiences a different local magnetic field due to their (hyperfine) interactions with local spin-active nuclei.[4] Assuming the electron-electron interactions are equal to zero, a spin Hamiltonian can be constructed as:

$$\hat{H} = \omega_1 \hat{S}_{1z} + \omega_2 \hat{S}_{2z} + \sum_{i=1}^{2} \sum_{j=1}^{N} \hat{\mathbf{I}}_j A_{ij} \hat{\mathbf{S}}_i \qquad \text{Equation 1.1}$$

where: $\omega_i = \mu_B g_i B$ represents the Zeeman interaction of electron i with a magnetic field of strength B; and A_{ij} is the hyperfine tensor for the hyperfine interaction of electron i with nucleus j.[5]

The singlet state is composed of a linear combination of the eigenstates of $\hat{H}$: $|S\rangle = \sum_n c_n |n\rangle$ where $|n\rangle$ are the eigenstates and c_n are the coefficients. As a non-eigenstate, the singlet state is non-stationary and evolves through time in accordance with the integrated time-dependent Schrödinger equation (Equation 1.2). This evolution manifests itself in the interconversion of singlet and triplet character in the SCRP (Figure 1.2).[5,6]

$$|\psi(t)\rangle = \exp\left(-\frac{i}{\hbar}\hat{H}t\right)|S\rangle \qquad \text{Equation 1.2}$$

In the absence of a magnetic field, $\omega_i = 0$ and so the eigenstates are split solely by hyperfine interactions. The introduction of a weak magnetic field ($\omega_i \neq 0$) produces a Zeeman interaction that lifts the degeneracies between some of the eigenstates.[5,7] This increases the number of pathways for singlet-triplet interconversion, increasing the efficiency of the interconversion.[7] This magnetic field effect (MFE) is orientation-dependent because the hyperfine tensor (A_{ij}) is typically anisotropic.[8] The distribution of radical recombination products is influenced by the singlet-triplet interconversion efficiency, which itself is influenced by the strength and orientation of an external magnetic field (Figure 1.2).[9]

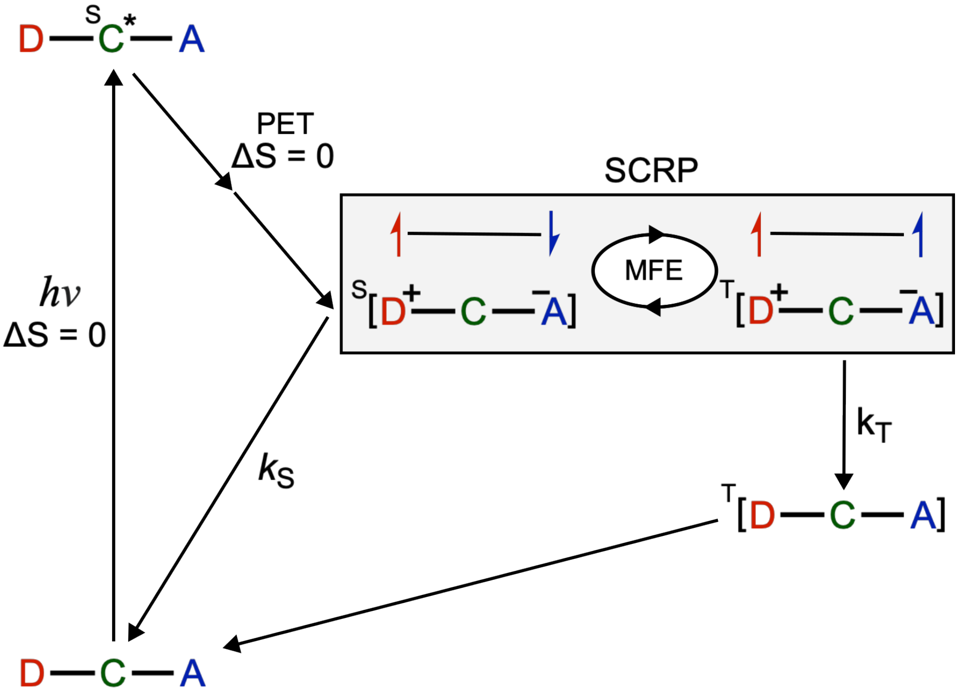

Figure 1.2 Simplified scheme for the radical pair mechanism in a model donor-chromophore-acceptor (D-C-A) triad. Photoexcitation of the chromophore obeys the spin selection rule. The singlet-excited chromophore undergoes rapid photoinduced electron transfer (PET) to generate a spin-correlated radical pair (SCRP) in the singlet state. Singlet-triplet interconversion in the SCRP displays a magnetic field effect (MFE) which influences the distribution of radical recombination products.

The sensitivity of the RPM to magnetic fields has sparked interest from spin chemists because the molecular magnetic interactions are much weaker than the thermal energy, $k_B T$. The key to the sensitivity arises from the fact that the SCRP is generated in a non-Boltzmann state far from thermal equilibrium. As a result, small perturbations to the system, like the application of a weak magnetic field, have significant consequences.[8]

1.2 Molecular Compasses

Model donor-chromophore-acceptor triads have been used to establish the principles of the radical pair mechanism and untangle the mystery of avian magnetoreception.[9,10] Seeking inspiration from nature, there is growing interest in using model triads to develop molecular compasses for the next generation of quantum sensing technologies.[11,12]

When designing a molecular compass capable of displaying orientation-dependent magnetic field effects, there are several criteria that must be met:[9]

a) Under photoexcitation, the molecule must generate a SCRP with good yield.

b) The electrons in the SCRP should be sufficiently well-separated that electron-electron interactions are negligible (c.a. 1 nm). Otherwise, the singlet state is an eigenstate of the spin Hamiltonian and no spin evolution occurs.

c) The hyperfine couplings in the SCRP should be asymmetric (strong for one electron and weak for the other). This promotes spin mixing as the local magnetic fields experienced by each electron are different.

d) The SCRP should have a lifetime on the timescale of hyperfine-driven singlet-triplet interconversion (c.a. 100 ns).

e) The MFE must be measurable. The singlet and triplet radical pairs should recombine to give products with identifiable spectroscopic signatures.

With this stringent list of requirements and the need for bespoke spectrometers to measure MFEs[9], it is unsurprising that few molecular compasses have been reported. The only triad that has shown orientation-dependent MFEs in Earth-strength fields is the carotenoid-porphyrin-fullerene (CPF) triad (Figure 1.3), first synthesised by Kodis *et al.* and measured by Maeda *et al* from the groups of Prof. Gust and Prof. Timmel.[9,10,13]

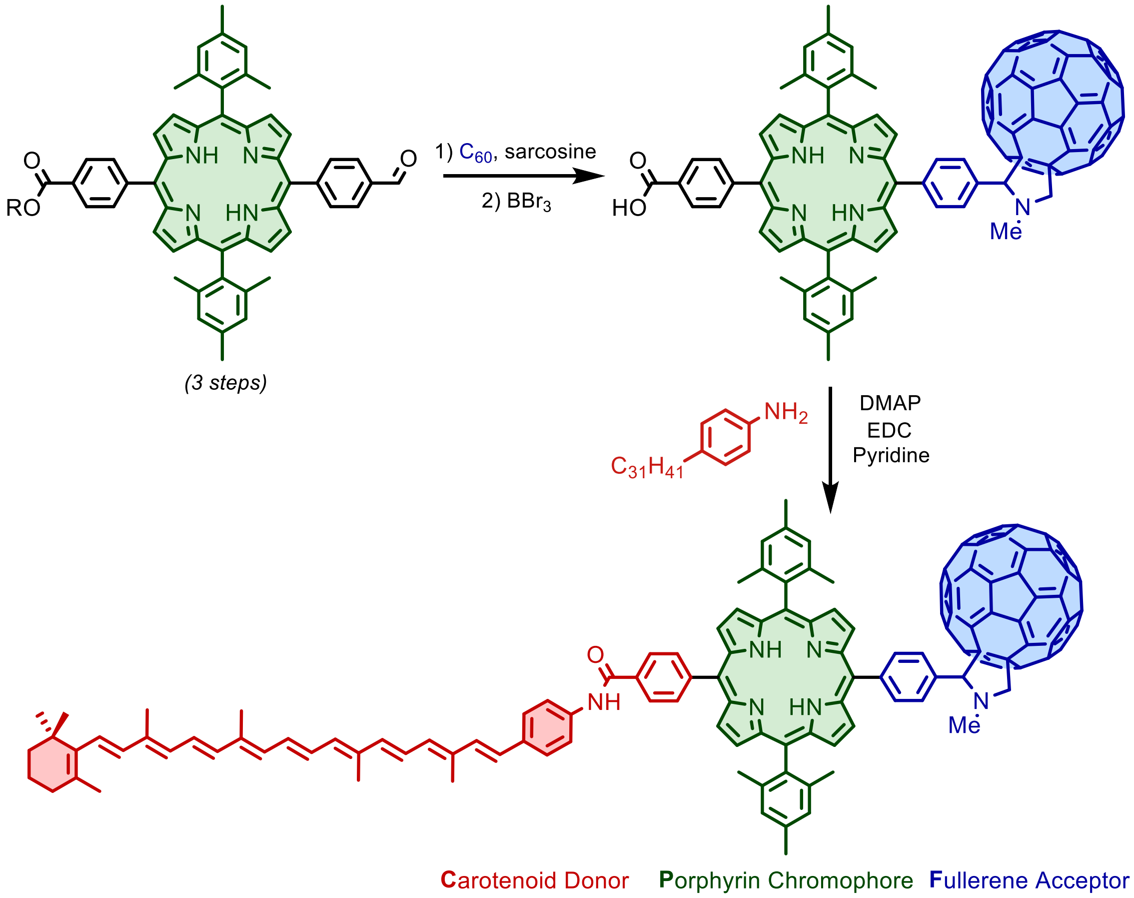

Figure 1.3 Synthetic scheme for the carotenoid-porphyrin-fullerene triad (CPF), first reported by Kodis *et al.*[13] DMAP = 4-dimethylaminopyridine. EDC = 1-ethyl-3-(3-dimethylaminopropyl)carbodiimide.

The structure of CPF is well-suited for magnetic field effects. The donor and acceptor are bonded to the porphyrin at opposite *meso*-positions, which ensures spatial separation of the electrons in the radical pair. Additionally, the abundance of ^{1}H nuclei ($I = ½$) on the carotenoid and their absence on the fullerene acceptor provides asymmetric hyperfine couplings in the SCRP.[10]

At larger magnetic fields (4-1000 mT), Riese *et al.* reported strong magnetic field effects in a triarylamine-palladium(II)porphodimethenato-napthalenediimide (TPN) triad (Figure 1.4).[14]

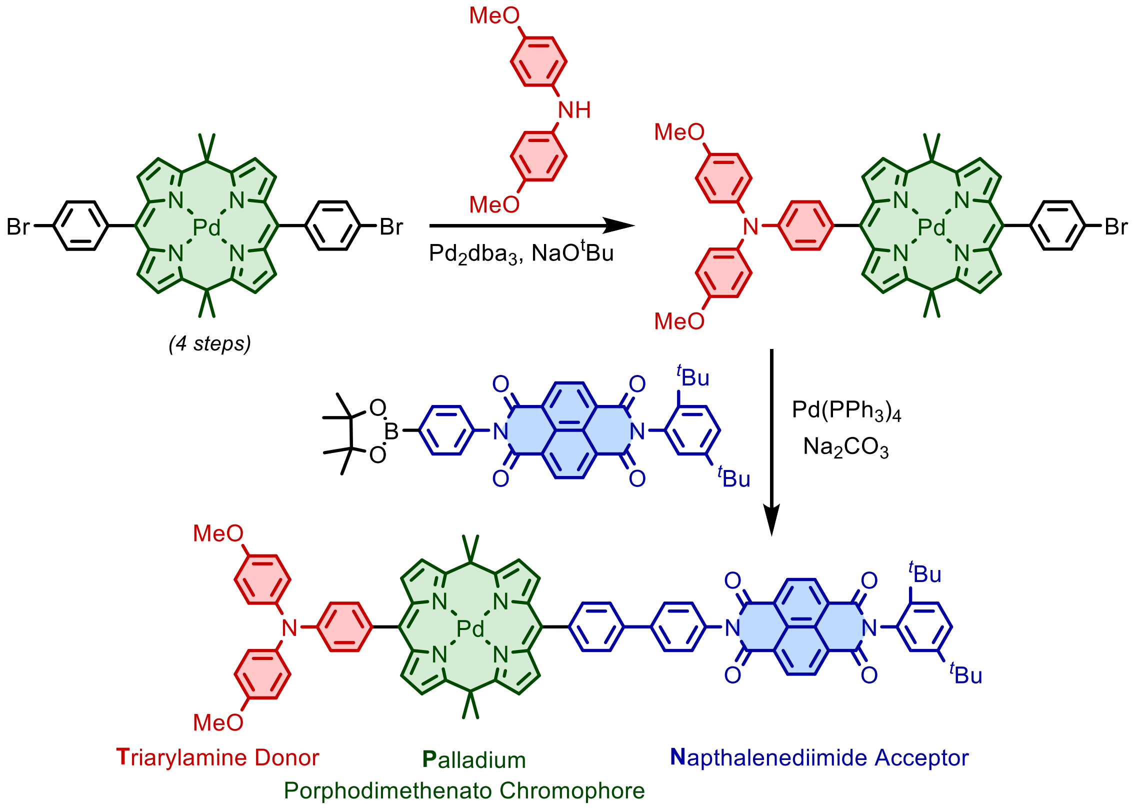

Figure 1.4 Synthetic scheme for the triarylamine-palladium(II)porphodimethenato-napthalenediimide triad (TPN), first reported by Riese *et al.*[14]

This triad shares many of the same design principles as CPF. The donor and acceptor are bonded on opposite sides of the chromophore and separated with phenyl spacers, so that the electrons in the SCRP are spatially separated. A bridged porphodimethenato complex was chosen as the chromophore over a palladium(II) porphyrin, because the high oxidation potential of the porphyrin gave a poor driving force for PET. No MFE was observed at low magnetic fields (< 300 µT). The authors were unable to find a reason for the lack of low field MFEs, which demonstrates the need for further investigation into the structural factors affecting MFEs.[14]

The design of a molecular compass requires a delicate balance of features. To design new molecular compasses, it would be beneficial to determine structure-property relationships by screening different combinations of chromophores, donors and acceptors. The synthesis of triads typically involves sequential reactions that require case-by-case optimisation (Figures 1.3 and 1.4). This makes the current synthetic routes towards triads unsuitable for screening large numbers of triad components. To circumvent this obstacle, we investigated a modular approach to the synthesis of molecular compasses through axial assembly, inspired by the work of Poddutoori, van der Est *et al.*

1.3 Aluminium Porphyrin Complexes

Porphyrins are desirable chromophores for molecular compasses. Delocalisation of their 26 π-electrons produces a small HOMO-LUMO gap, and so they absorb strongly in the visible region. Two absorption bands are typically observed, which are assigned to two π-π^* transitions (Figure 1.5).[15] To tweak the electronic properties of the porphyrin, substituents can be introduced to the *meso-* and *β*-positions (Figure 1.5). Additionally, various metals can be inserted into the centre of the porphyrin that further alter the properties of the porphyrin and provide new sites for axial bond-formation.

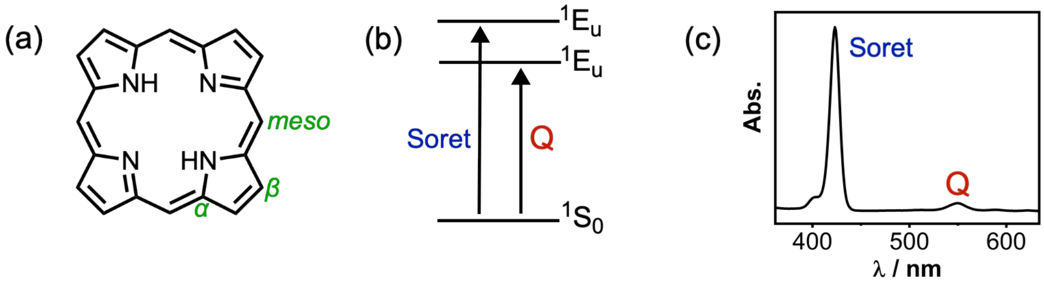

Figure 1.5 (a) Nomenclature convention for porphyrin substituents. (b) Naming convention for porphyrin π-π^* transitions. (c) Annotated UV-Vis absorbance spectrum (1,2-dichlorobenzene, 293 K) of zinc tetraphenylporphyrin (structure and synthesis given in the appendix).

The axial bonding exhibited by metalloporphyrins varies according to the chemistry of the metal (Figure 1.6). Several metalloporphyrins can bind ligands on both faces, enabling the assembly of triads through the metal atom.[16,17] Of these dual-binding complexes, aluminium porphyrins are advantageous because they feature two orthogonal binding modes (referred to as covalent and dative in this thesis). By using different donor atoms (oxygen and nitrogen), two different ligands can bind to the aluminium without the need for a statistical approach (which relies on 1:1:1 stoichiometry).[18]

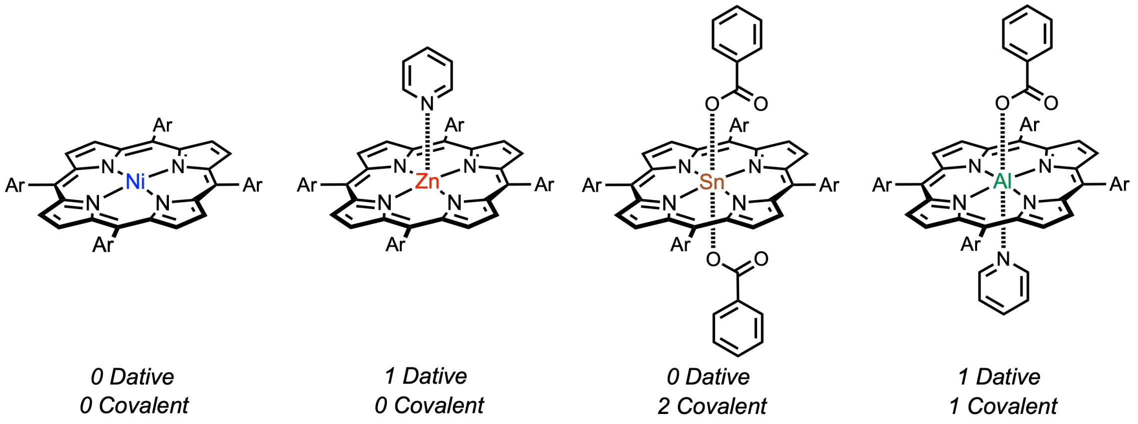

Figure 1.6 Typical coordination geometries of selected metalloporphyrins.[16,17]

The synthesis of aluminium porphyrins, through treatment of the freebase porphyrin with trimethylaluminium at room temperature, was reported by Davidson *et al.* in the Sanders group (Figure 1.7).[19] This produces a methylated aluminium porphyrin which is highly reactive. Quenching with water gives the hydrolysed aluminium porphyrin, a stable intermediate complex that was used by the Sanders group to construct supramolecular assemblies (see below).

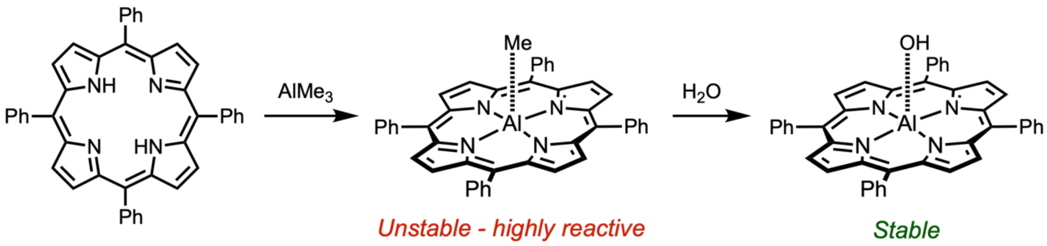

Figure 1.7 Synthetic scheme for a stable aluminium porphyrin complex, reported by Davidson *et al.*[19]

The hydroxyl ligand can be substituted for a carboxylic acid or alcohol with a condensation reaction (Figure 1.8).[18] Reports on the stability of this product vary, with conflicting claims about its moisture sensitivity.[19,20] Dative binding on the other face of the aluminium porphyrin is weaker, requiring an excess of the Lewis base in solution (Figure 1.8). While the substitution of benzoic acid has little effect on the electronic structure of the porphyrin, the binding of a Lewis base pulls the aluminium down into the plane of the porphyrin, which allows the dative binding to be monitored by UV-Vis.[19]

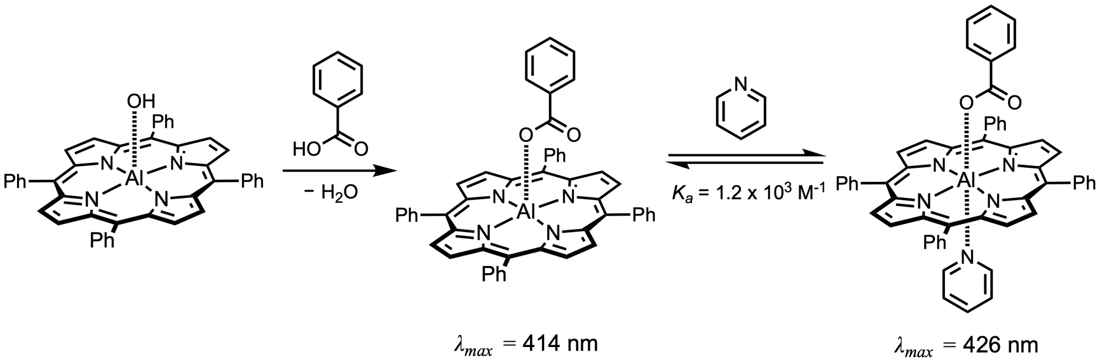

Figure 1.8 Synthetic scheme for an aluminium porphyrin with ligands bound on each face, reported by Davidson *et al.*[19] The pyridine binding constant was reported by Poddutoori *et al.*[18]

Davidson *et al.* (2008) were the first to exploit the dual binding modes of an aluminium porphyrin to generate supramolecular structures, using isonicotinic acid to generate oligomeric chains (Figure 1.9).[21] A similar approach was later used in the Anderson group to synthesise a Russian doll structure consisting of two concentric porphyrin nanorings.[22]

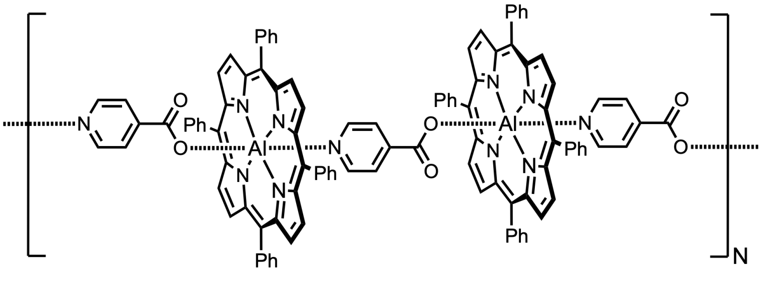

Figure 1.9 Coordination polymer based on an aluminium porphyrin, reported by Davidson *et al.*[21]

Over the last 15 years, Poddutoori and co-workers have synthesised a series of aluminium porphyrin triads to create model photosynthetic reaction centres. Many of these triads are capable of ultrafast PET, and so this work is a valuable starting point for the design of molecular compasses. The reported kinetics of PET and radical recombination in these triads depend strongly on the redox potentials of the donor, acceptor and porphyrin, and the donor-acceptor distance (Figure 1.10).[18,23–27] Magnetic field effects have never been reported in aluminium porphyrin triads.

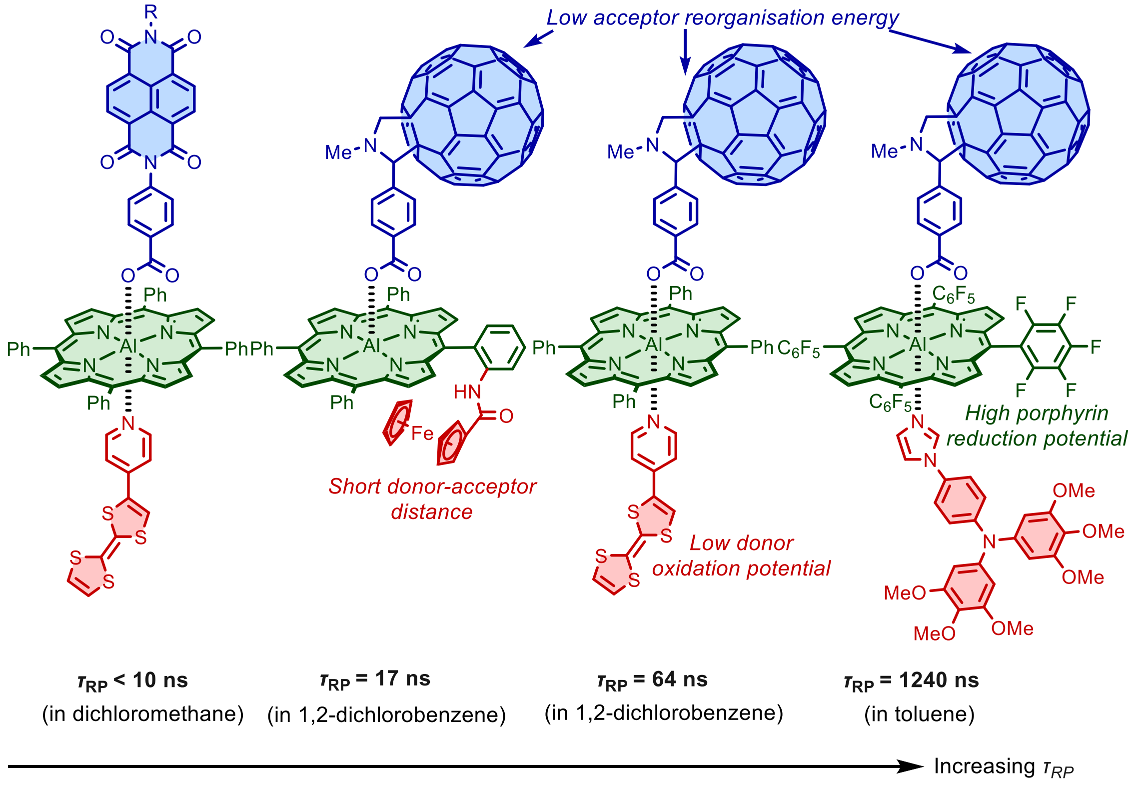

Figure 1.10 A selection of triads synthesised by Poddutoori *et al.*[18, 23-27], annotated with their key features. τ_{RP} = radical pair lifetime at 293 K.

A limitation of these systems is that the radical pairs produced from PET are typically short lived (lifetime < 100 ns), which is not optimal for MFEs (see Section 1.2, requirement d). The only reported triad with a sufficiently long-lived radical pair features pentafluorophenyl *meso-* side chains (rightmost triad in Figure 1.10). The electron-withdrawing groups reduce the electronic coupling between the porphyrin-based orbitals and the donor-based orbitals, which decelerates radical pair recombination.[26]

1.4 Project Aims and Molecular Design

To assess the viability of aluminium porphyrin-based modular triads for magnetic sensing, this thesis explores the synthesis of a prototype target triad alongside several reference compounds. To complement this synthetic work, the research in this thesis also employs a variety of spectroscopic tools (UV-Vis spectroscopy, fluorescence spectroscopy, transient electron spin resonance spectroscopy and transient absorption spectroscopy) to characterise the excited state behaviour of the target compounds.

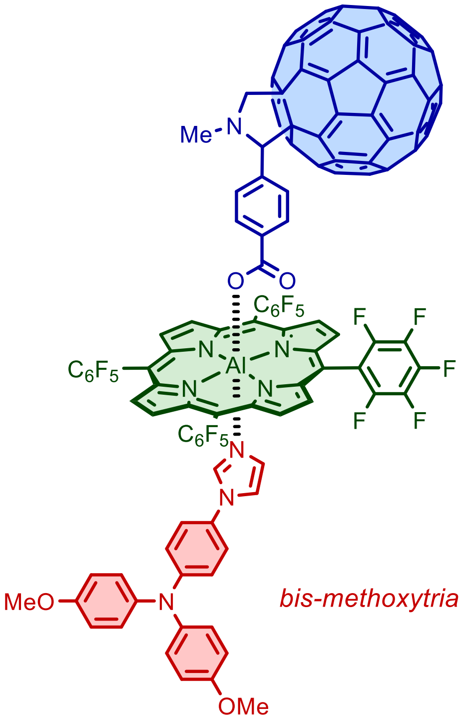

C_{60} electron acceptor from CPF triad

C_6F_5 meso- side chains to decelerate radical pair recombination

bis-methoxytriarylamine donor from TPN triad

Figure 1.11 Target triad molecule, annotated with its key design features.

With the aim of fitting the molecular compass criteria, the target molecule (in Figure 1.11) was designed through careful examination of the existing literature – particularly the work of Poddutoori *et al.* The choice of acceptor and donor was inspired by the molecular compasses CPF and TPN respectively.[10,14] The donor was appended with an imidazole binding group, because the binding of imidazole is reportedly stronger than pyridine.[18] The pentafluorophenyl *meso-* side chains were chosen as they reportedly increase the lifetime of the radical pair.[26]

2 Synthesis of an Aluminium Porphyrin Triad

2.1 Synthesis of Reference Complexes

The free-base porphyrins **H_2Por^{t}Bu** and **H_2PorF$_{20}$** were synthesised using literature procedures (Figure 2.1).[26,28] Aluminium insertion was achieved with trimethylaluminium and confirmed by the disappearance of the free-base N-H protons by ^{1}H NMR.

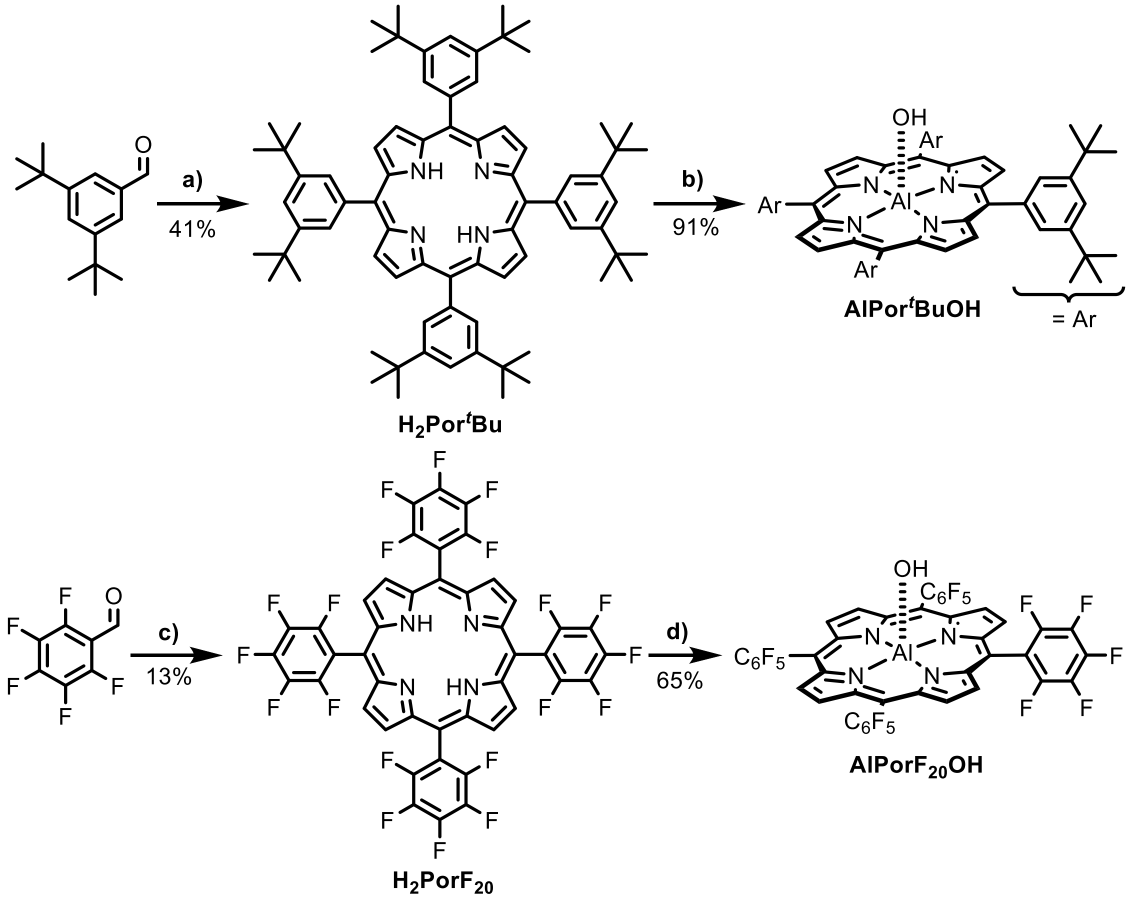

Figure 2.1 Synthetic routes to **AlPor^{t}BuOH** and **AlPorF$_{20}$OH**. Reaction conditions: a) Pyrrole then TFA then DDQ, CH_2Cl_2, 20 °C, 41%[28]; b) $AlMe_3$ then H_2O, toluene, 20 °C, 91%[19]; c) Pyrrole then BF_3•OEt_2 then DDQ, CH_2Cl_2, 20 °C, 13%[26], d) $AlMe_3$ then H_2O, toluene, 20 °C, 65%[26].

Condensation of **AlPor^{t}BuPh** and **AlPorF$_{20}$OH** with benzoic acid was achieved by stirring at room temperature in the presence of anhydrous sodium sulfate (Figure 2.2).[19] Binding was confirmed by the shielding of the benzoate protons in the ^{1}H NMR spectrum (Figure 2.2). Proton *b,* closest to the porphyrin, is shielded most ($\Delta\delta = 3.0$ ppm).

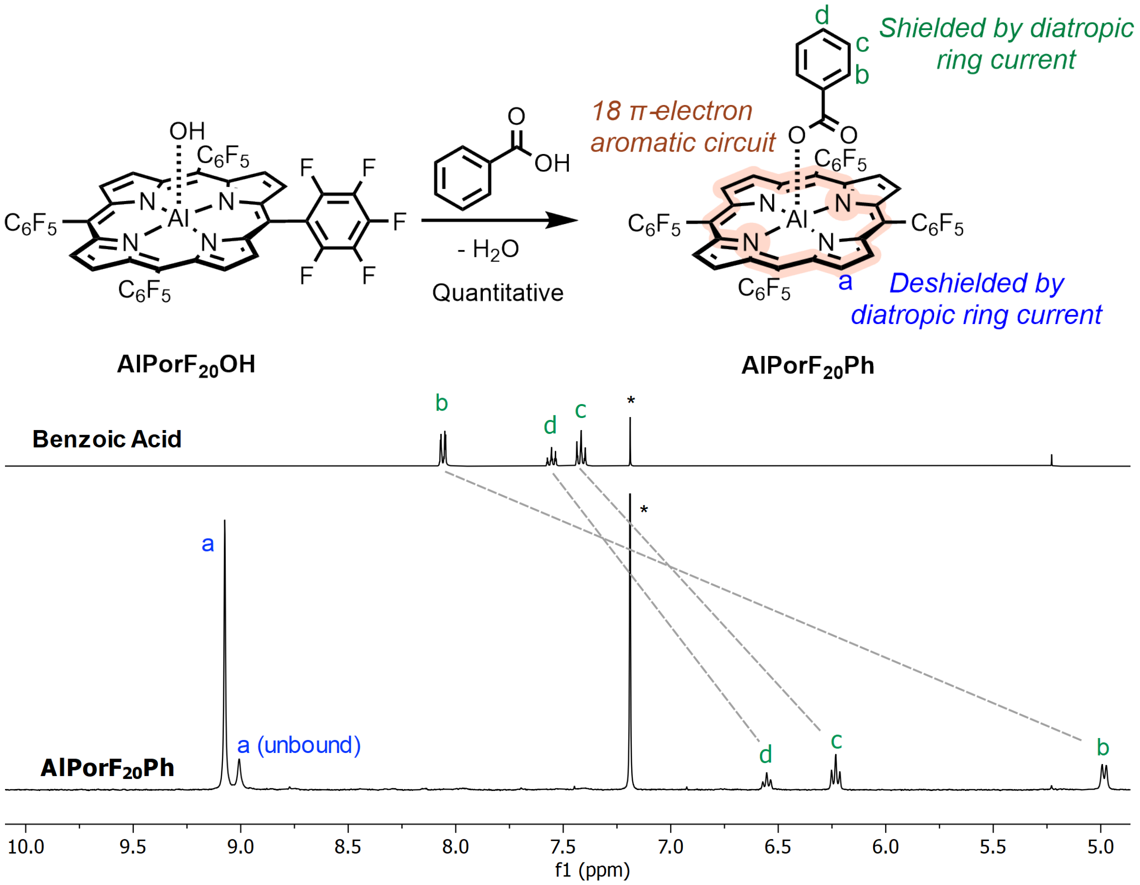

Figure 2.2 Top: synthetic scheme for the condensation reaction to produce **AlPorF₂₀Ph**. The product is annotated to show its aromaticity and the impact of the ring current on the chemical shift of the surrounding protons. Bottom: ^{1}H NMR (400 MHz, $CDCl_3$) spectra of benzoic acid and **AlPorF₂₀Ph** showing the shielding of the benzoate protons. * = $CHCl_3$.

Separation of excess benzoic acid from the benzoate complexes was challenging. Purification by silica and alumina column chromatography led to removal of the benzoate ligand. Separation by size exclusion chromatography was poor. The reported purification of these complexes involves solvent washes, relying on differences in solubility.[19,23]

The dative binding of pyridine (py) and 1-methylimidazole (MeIm) to **AlPor^{t}BuPh** and **AlPorF₂₀Ph** was tracked by UV-Vis titration (Figure 2.3). The presence of isosbestic points confirm that the binding is 1:1. The binding equilibrium constants, K_a, were determined by fitting the experimental data to a 1:1 binding isotherm. Figure 2.3 shows the binding titration of **AlPor^{t}BuPh** with py. Other titrations are shown in the appendix.

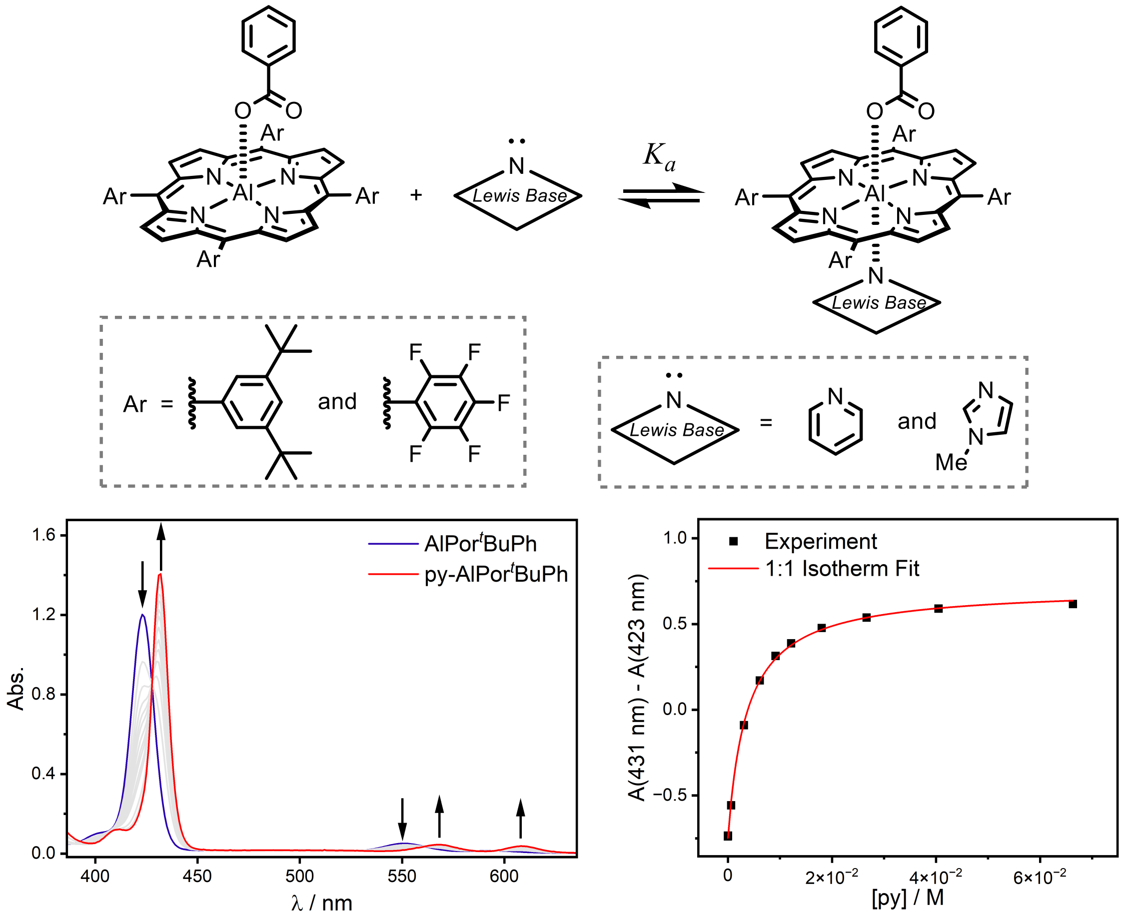

Figure 2.3 Top: scheme for the dative binding of Lewis bases to aluminium porphyrin reference complexes. Bottom left: UV-Vis (o-DCB, 293 K) titration of **AlPor^{t}BuPh** (5 µM) with pyridine, added up to 66 mM in increments. Isosbestic points are present at 428 nm, 561 nm and 589 nm. UV-Vis titrations for the other complexes are shown in the appendix. Bottom right: binding curve for the UV-Vis titration, showing the absorbance difference between the peaks of the Soret bands (423 and 431 nm) against increasing pyridine concentration. The best fit obtained with a 1:1 binding isotherm is shown in red.

Table 2.1 Binding constants (o-DCB, 293 K), determined by fitting the UV-Vis titration binding curves to a 1:1 binding isotherm. For **AlPor^{t}BuPh** the titrations were performed twice, so the reported binding constant is the mean and the uncertainty is the standard deviation. a = error estimated from the fitting of one titration.

Compound	Lewis Base	K_a / M^{-1}
AlPor^{t}BuPh	Pyridine	$(3.0 \pm 0.3) \times 10^2$
	Methylimidazole	$(8.5 \pm 3.0) \times 10^4$
AlPorF$_{20}$Ph	Pyridine	$(2.5 \pm 0.2^{a}) \times 10^4$
	Methylimidazole	$(1.3 \pm 0.1^{a}) \times 10^6$

In line with the literature, the binding of 1-methylimidazole was found to be stronger than pyridine (Table 2.1).[18] This was helpful in confirming the molecular design decision to append the donor with imidazole. The stronger binding of both Lewis bases to **AlPorF$_{20}$Ph** over **AlPor^{t}BuPh** reflects the greater Lewis acidity of the aluminium, due to the electron-withdrawing pentafluorophenyl *meso*- side chains.

The UV-Vis titrations were carried out in 1,2-dichlorobenzene (o-DCB), as this was the solvent used later in spectroscopic work. UV-Vis evidence of binding was also observed in other non-coordinating solvents such as chloroform and toluene. In coordinating solvents like methanol, 2-methyltetrahydrofuran and acetonitrile, binding was not observed with equivalent concentrations of the Lewis bases. This is attributed to preferential coordination of the solvent to the aluminium.

2.2 Synthesis and Binding of the Fullerene Acceptor

2.2.1 Synthesis of **C$_{60}$COOH**

The target electron acceptor, **C$_{60}$COOH**, is a fullerene derivative. The functionalisation of C_{60} can be achieved with the Prato reaction – the 1,3-dipolar cycloaddition of an azomethine ylide to the fullerene.[29] The ylide is generated *in-situ* from the reaction of an aldehyde with a glycine derivative, by heating to reflux in toluene.

To synthesise **C$_{60}$COOH**, the direct reaction of C_{60} with N-methylglycine and sarcosine was initially attempted (Figure 2.4).[23] Whilst TLC suggested that the reaction was successful, the poor solubility of **C$_{60}$COOH** made purification by silica column chromatography challenging.

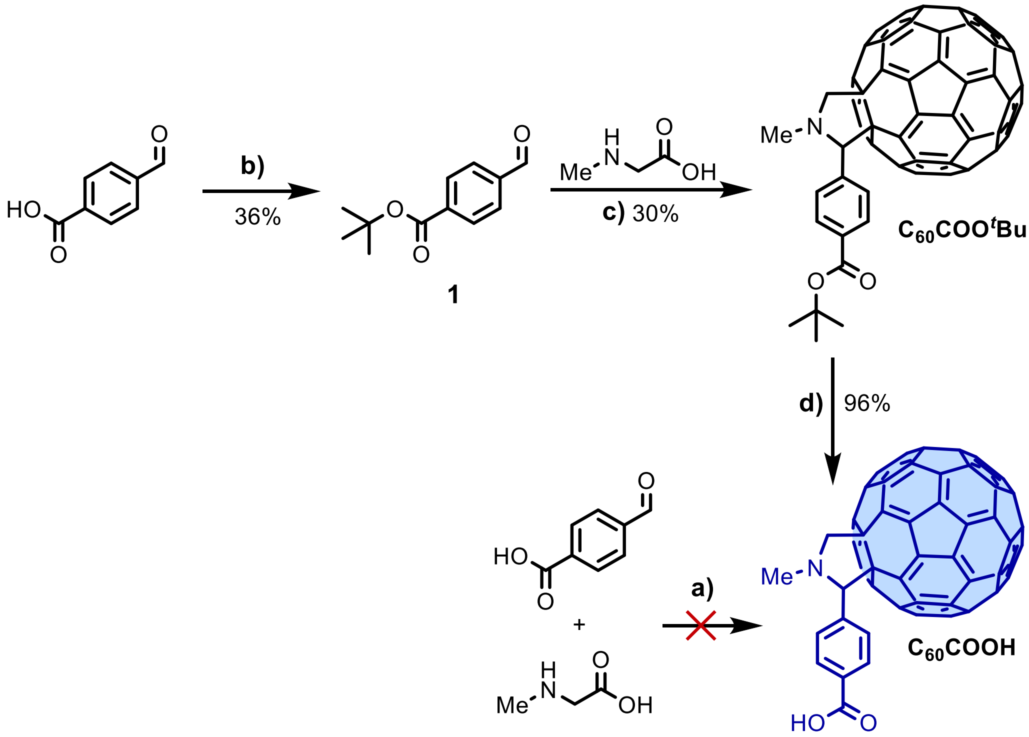

Figure 2.4 Synthetic scheme for the routes towards **C$_{60}$COOH**. Reaction conditions: a) C$_{60}$, toluene, reflux, purification was not possible[23]; b) *tert*-butyl 2,2,2-trichloroacetimidate, BF_3•OEt_2, cyclohexane/THF = 7:3 *v/v*, 20 °C, 36%[49]; c) C$_{60}$, toluene, reflux, 30%[23]; d) TFA/CH_2CH_2 = 1:4 *v/v*, 20 °C, 96%[47].

To resolve the purification problems, the carboxylic acid was protected as a *tert*-butyl ester. **C$_{60}$COO^{t}Bu** was synthesised by adapting the previous Prato reaction conditions (Figure 2.4). Deprotection of the ester was performed in trifluoroacetic acid / dichloromethane (1:4 *v/v*) to give the desired product **C$_{60}$COOH** (Figure 2.4). The product is poorly soluble in chloroform and toluene, but THF-d$_8$ provided adequate solubility for a ^{1}H NMR spectrum to be recorded (reference spectrum in Figure 2.6).

2.2.2 *Attempted Condensation of* **C$_{60}$COOH** *with* **AlPor^{t}BuOH**

The condensation reaction between **C$_{60}$COOH** and **AlPor^{t}BuOH** was attempted (Figure 2.5). Literature conditions for the binding of **C$_{60}$COOH** to aluminium porphyrins involve heating to 80 °C in toluene, presumably to encourage **C$_{60}$COOH** to dissolve.[25] For this reaction, these conditions did not lead to product formation (by ^{1}H NMR spectroscopy).

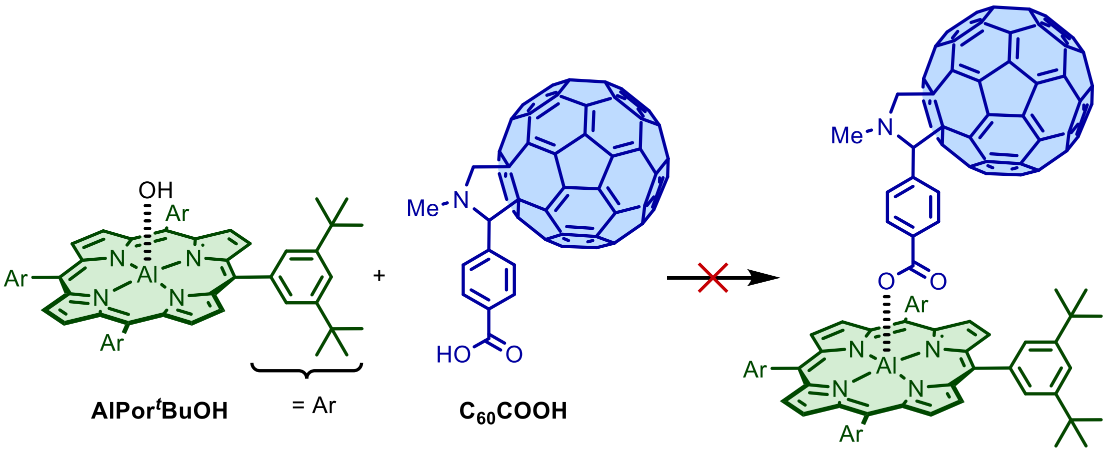

Figure 2.5 Synthetic scheme for the unsuccessful reaction between **AlPor^{t}BuOH** and **C$_{60}$COOH**. The attempted conditions are summarised in Table 2.2.

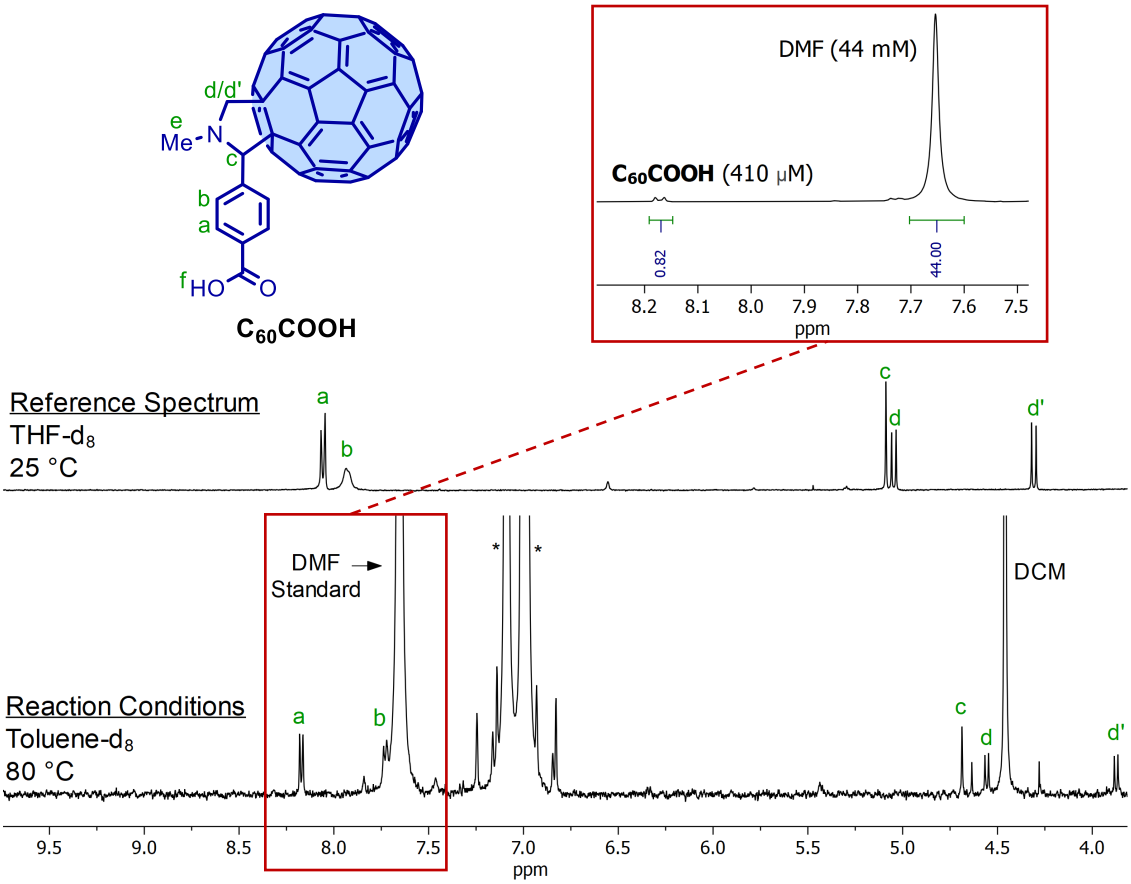

Figure 2.6 Top: reference ^{1}H NMR (400 MHz, THF-d$_8$) spectrum of **C$_{60}$COOH**. Bottom: ^{1}H NMR (500 MHz, toluene-d$_8$) spectrum of **C$_{60}$COOH** with an internal reference standard of DMF (44 mM). The measurement conditions replicated the literature reaction conditions. The solution was saturated with **C$_{60}$COOH**. * = toluene (solvent) peaks.

To understand the lack of reactivity, the NMR spectrum of **C$_{60}$COOH** was recorded, saturated in toluene-d$_8$ at 80 °C (replicating the literature reaction conditions) (Figure

2.6). An internal standard of DMF (44 mM) was included to enable quantification of the **C$_{60}$COOH** concentration. Weak signals are assigned to **C$_{60}$COOH** through comparison with the NMR spectrum in THF-d_8. The calculated concentration of dissolved **C$_{60}$COOH** (410 μM) is significantly lower than the nominal concentration (5.0 mM). This shows that **C$_{60}$COOH** fails to fully dissolve in these conditions – a possible reason for the lack of reactivity.

In light of this, further conditions were tested to try to get **C$_{60}$COOH** to dissolve (Table 2.2). Heating the reaction mixture to reflux in toluene still gave no product (entry 2). THF was tested as a reaction solvent, because **C$_{60}$COOH** exhibits better solubility in it, but no reaction was observed again (entries 3-4). Presumably, this was due to coordination of the solvent to the aluminium, as noted in Section 2.1.

Table 2.2 Reaction conditions tested for the condensation reaction of **C$_{60}$COOH** with **AlPor^{t}BuOH**. Product formation was determined by ^{1}H NMR spectroscopy.

Entry	Solvent	Temp / °C	Time	[C$_{60}$COOH]^a / mM	[AlPor^{t}BuOH] / mM	Product Formed ?
1[25]	Toluene	80	17 hours	5.0	5.0	No
2	Toluene	110	3 days	25.0	5.0	No
3	THF	50	17 hours	1.5	1.0	No
4	Toluene / THF (2:1 *v/v*)	60	17 hours	5.0	3.0	No

a = nominal concentration of **C$_{60}$COOH**. The true concentration of the **C$_{60}$COOH**-saturated solution is assumed to be lower given the results of Figure 2.6.

2.2.3 *Redesign and Synthesis of* **C$_{60}$BnCOOH**

The failure of **C$_{60}$COOH** to react, attributed to its poor solubility, led to the redesign of the target molecule. The solubility of the fullerene derivative was improved by replacing the methyl substituent at the *N*- position with a bulky 3,5-di-*tert*-butylbenzyl group.

The solubilising group was introduced through reductive amination, prior to the Prato reaction (Figure 2.7). The carboxylic acid was again protected as a *tert*-butyl ester to aid in purification by silica column chromatography (Figure 2.7). The solubility of the final product, **C$_{60}$BnCOOH**, was better than **C$_{60}$COOH** in chloroform and toluene.

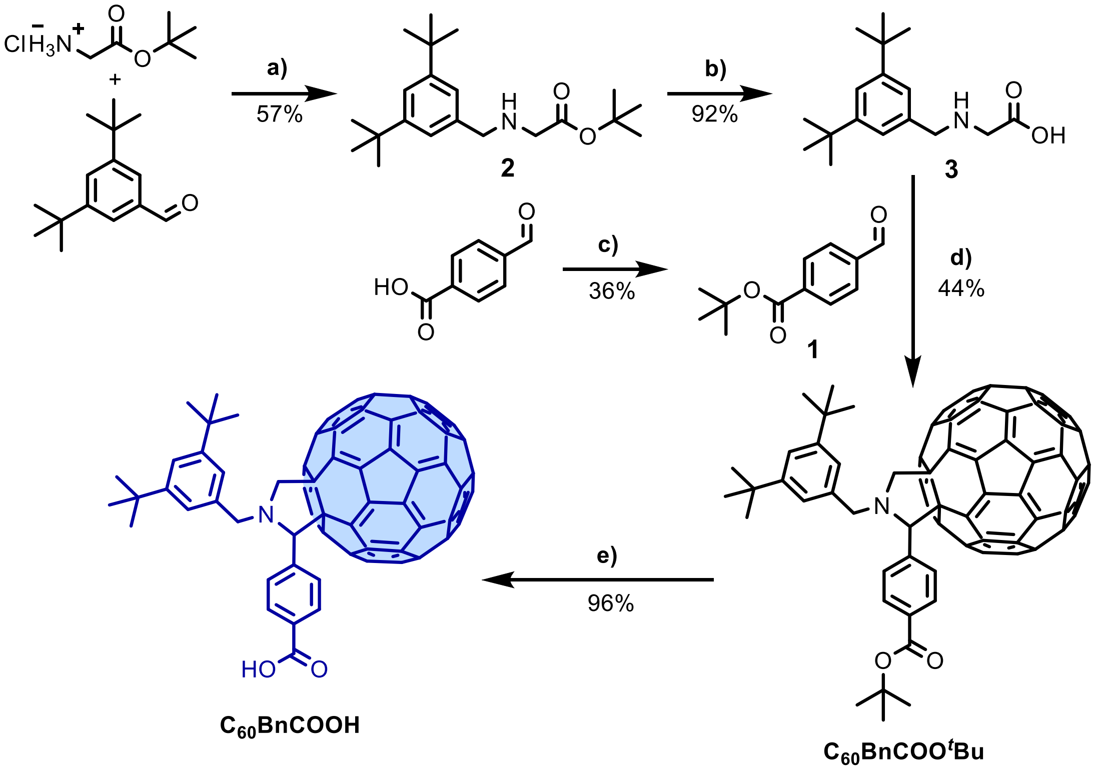

Figure 2.7 Synthetic scheme for the route towards **C$_{60}$BnCOOH**. Reaction conditions: a) 3,5-di-*tert*-butyl benzaldehyde and NEt$_3$ then NaBH$_4$, CH$_3$OH, 0 °C → r.t., 36%[50]; b) TFA/CH$_2$CH$_2$ = 1:1 *v/v*, 20 °C, 92%[51]; c) *tert*-butyl 2,2,2-trichloroacetimidate then BF$_3$•OEt$_2$, cyclohexane/THF = 7:3 *v/v,* 20 °C, 36%[49]; d) C$_{60}$, toluene, reflux, 44%[23]; e) TFA/CH$_2$CH$_2$ = 1:4 *v/v*, 20 °C, 96%[47].

2.2.4 Binding of **C$_{60}$BnCOOH**

The condensation reaction between **C$_{60}$BnCOOH** and **AlPorF$_{20}$OH**, to give the dyad **AlPorF$_{20}$C$_{60}$**, was achieved by stirring the two reactants in chloroform at room temperature (Figure 2.8). The addition of anhydrous sodium sulfate and the use of an excess of **C$_{60}$BnCOOH** (1.5 equivalents) helped drive the equilibrium. Attempts to remove the excess **C$_{60}$BnCOOH** with solvent washes (hexane, methanol and water) were unsuccessful, as the bound ligand tended to be removed from the complex as well. The presence of unbound **C$_{60}$BnCOOH** did not hinder the subsequent spectroscopic investigations, as the measurements were initiated by porphyrin photoexcitation. Formation of **AlPorF$_{20}$C$_{60}$** was confirmed by NMR spectroscopy (Figures 2.9 and 2.10), MALDI-TOF and UV-Vis (**AlPorF$_{20}$OH** is insoluble in toluene, **AlPorF$_{20}$C$_{60}$** is not).

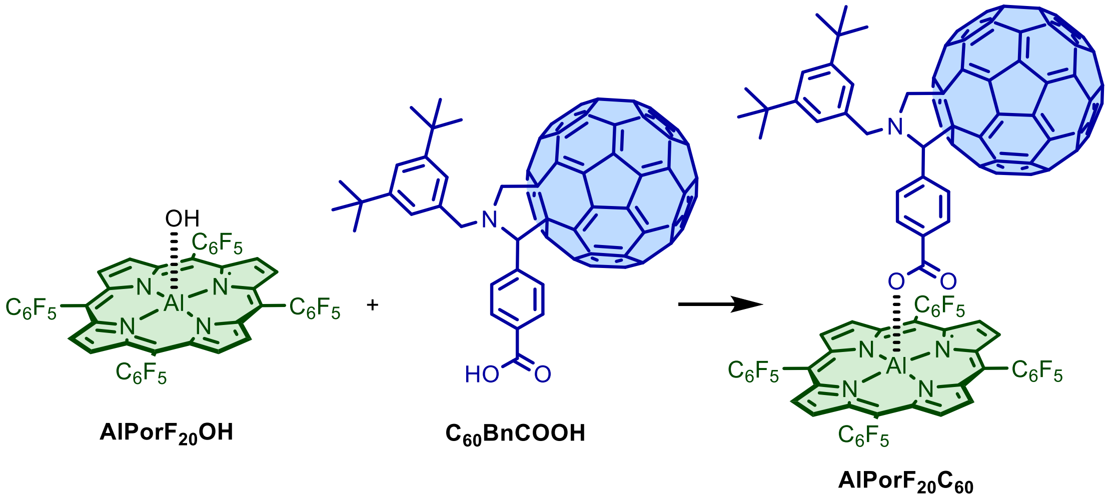

Figure 2.8 Synthetic scheme for the condensation of **AlPorF$_{20}$OH** and **C$_{60}$BnCOOH** to produce **AlPorF$_{20}$C$_{60}$**. Reaction conditions: $CHCl_3$, 20 °C, quantitative.

In the ^{1}H NMR spectrum, the protons of the carboxylic acid derivative are shielded upon binding to the aluminium porphyrin (Figure 2.9). Protons *a* and *b*, which are closest to the porphyrin, experience the greatest shielding. The peaks for *a* and *b* are broad in both complexes, which is attributed to intermediate phenyl bond rotation on the NMR timescale (illustrated in Figure 2.9). The increase in broadening upon coordination to the aluminium porphyrin reflects either: slower bond rotation due to the steric bulk of the porphyrin; or a greater chemical shift difference between the two sides of the phenyl ring due to the ring current of the porphyrin. Similar broadening and chemical shift values have been reported in the fullerene-coordinated aluminium porphyrins synthesised by Poddutoori *et al.*[23]

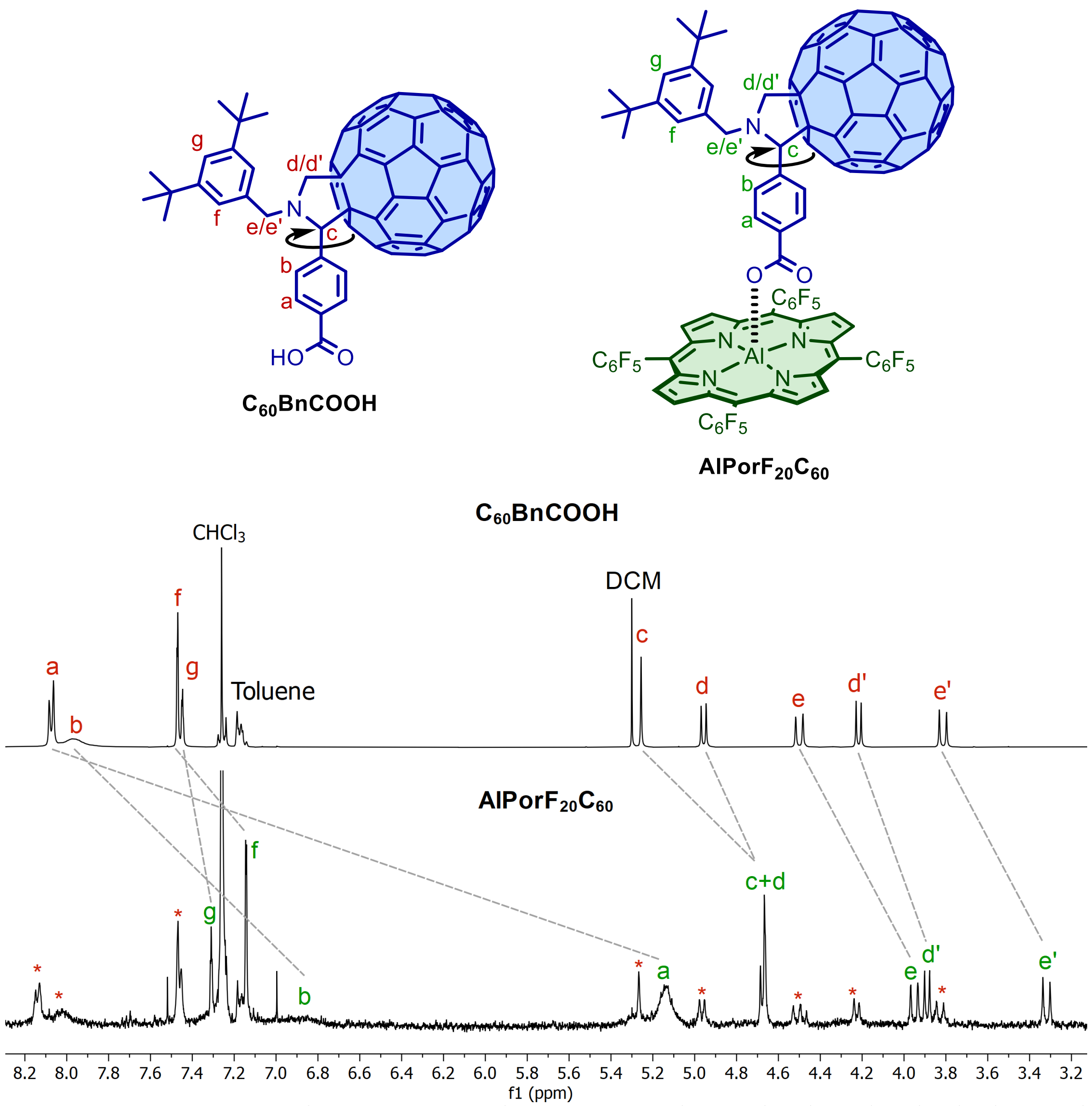

Figure 2.9 Top: structures of **C_{60}BnCOOH** and **AlPorF$_{20}$C$_{60}$**. The C-C bond rotation that leads to peak broadening is illustrated with an arrow. Bottom: ^{1}H NMR (400 MHz, CDCl$_3$, 298 K) spectra of **C_{60}BnCOOH** and **AlPorF$_{20}$C$_{60}$**. The shielding of the **C_{60}BnCOOH** protons, upon binding, is demonstrated by the dashed lines. * = signals assigned to unbound **C_{60}BnCOOH**.

The ^{19}F NMR spectrum of **AlPorF$_{20}$C$_{60}$** shows differences to **AlPorF$_{20}$OH** (Figure 2.10). For **AlPorF$_{20}$OH**, just three fluorine environments are present. The coalescence of *ortho*/*ortho'* and *meta*/*meta'* environments is attributed to opposite-face water exchange (shown in Figure 2.10), which is rapid at the NMR timescale. For **AlPorF$_{20}$C$_{60}$**, five fluorine environments are present. The lack of coalescence is attributed to either: slower exchange due to the stronger binding of **C_{60}COOH**; or a larger chemical shift difference between the two sides of the phenyl ring due to the presence of **C_{60}COOH**.

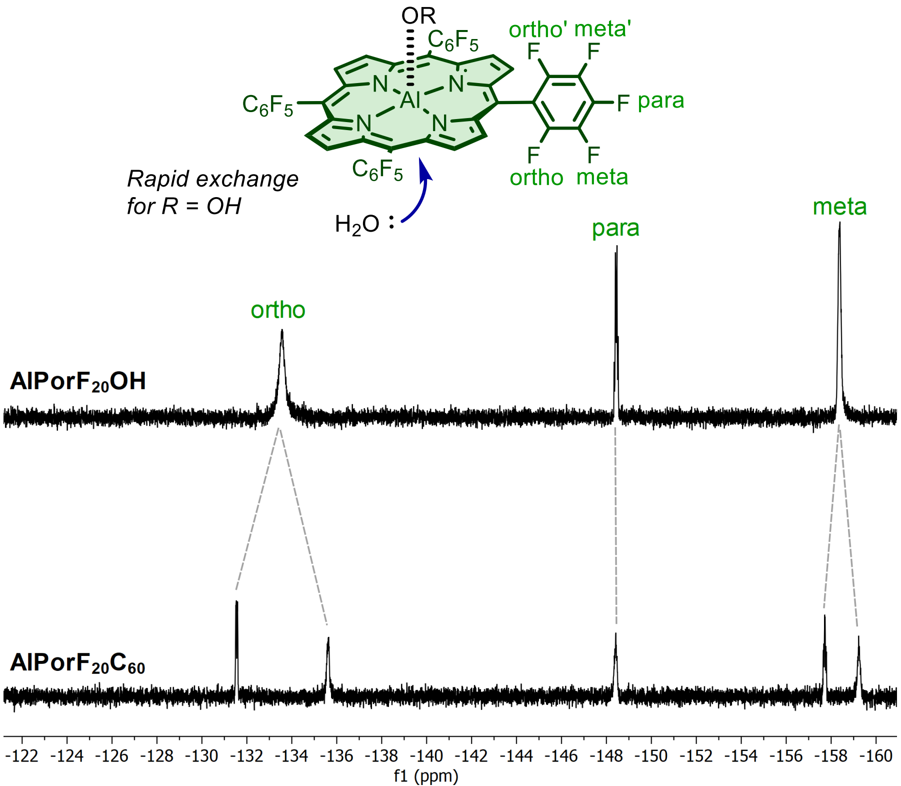

Figure 2.10 ^{19}F NMR (376 MHz, $CDCl_3$ / CD_3OD = 9:1 *v/v*, 298 K) spectra of **AlPorF$_{20}$OH** and **AlPorF$_{20}$C$_{60}$**, referenced so that the chemical shifts of the *para-* fluorine environments are equal.

2.3 Synthesis and Binding of the Triarylamine Donor

2.3.1 Synthesis of **TAAIm**

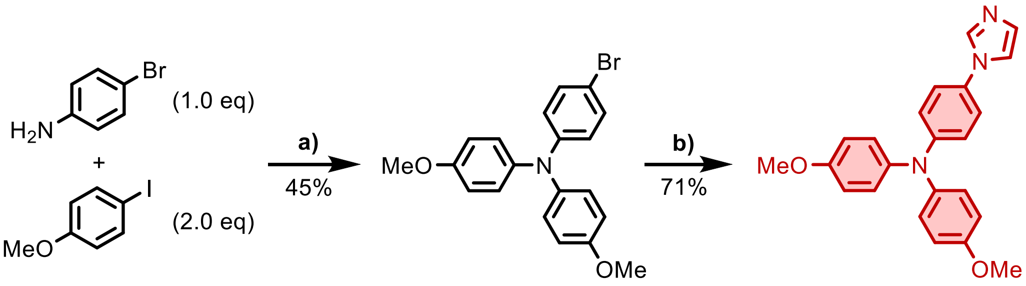

4

TAAIm

Figure 2.11 Synthetic scheme for the synthesis of **TAAIm**. Reaction conditions: a) CuI, 1,10-phenanthroline, KOH, toluene, reflux, 45%[30]; b) CuI, 1,10-phenanthroline, K_2CO_3, DMF, 150 °C, 71%.

TAAIm was synthesised by employing two successive Ullmann reactions (Figure 2.11). In the first step, literature conditions were used to ensure selective activation of the C-I bond over C-Br.[30] For the second step, the literature conditions were modified by raising the temperature from 110 °C to 150 °C (and increasing concentration) to drive oxidative addition at the C-Br bond.

2.3.2 Binding of **TAAIm**

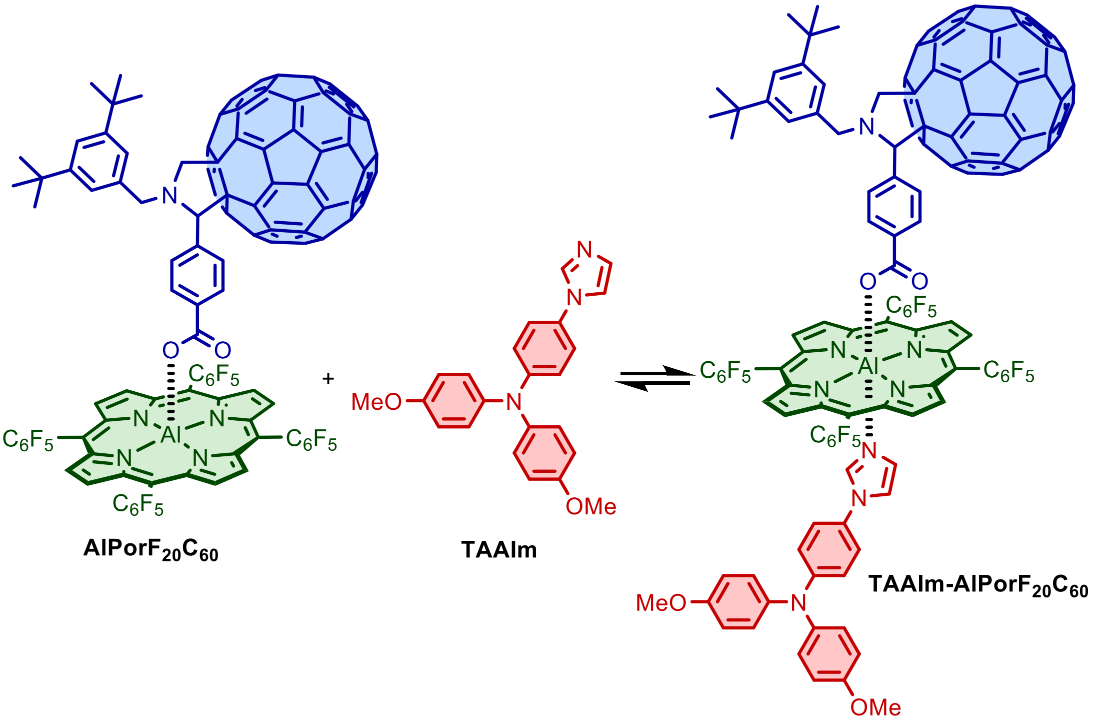

Figure 2.12 Binding of **TAAIm** to **AlPorF$_{20}$C$_{60}$** to form the triad **TAAIm-AlPorF$_{20}$C$_{60}$**.

Binding of **TAAIm** to **AlPorF$_{20}$C$_{60}$**, to form the triad **TAAIm-AlPorF$_{20}$C$_{60}$**, was tracked by UV-Vis titration (Figure 2.13). Fitting to a 1:1 binding isotherm produces a binding constant of $K_a = (2.7 \pm 0.6) \times 10^6$ M^{-1}, which is the same order of magnitude as the binding constant for 1-methylimidazole with **AlPorF$_{20}$Ph** (Table 2.1).

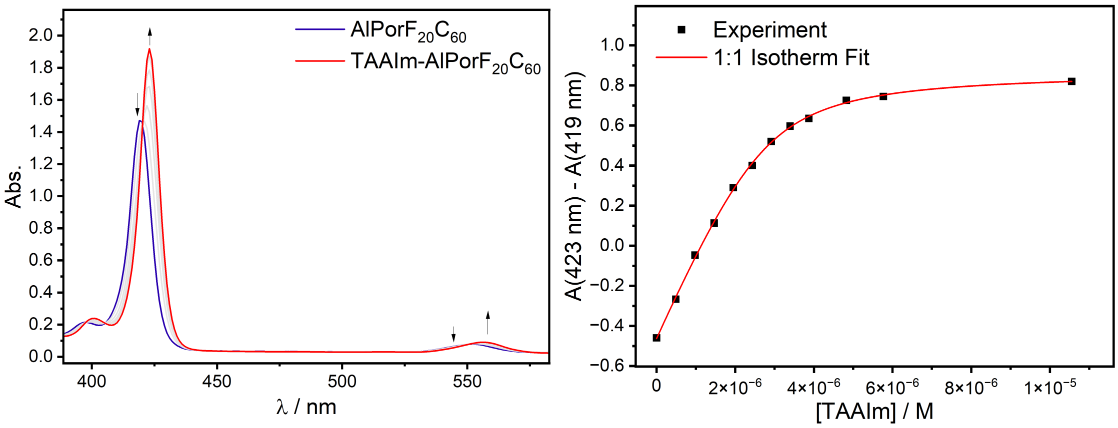

Figure 2.13 Left: UV-Vis (o-DCB, 293 K) titration of **AlPorF$_{20}$C$_{60}$** (c.a. 3.0 µM) with **TAAIm**, added up to 11 µM in 0.5 µM increments. Isosbestic points are present at 420 nm and 550 nm. Right: Binding curve for the UV-Vis titration, showing the absorbance difference between the peaks of the Soret bands (419 nm and 423 nm) against increasing **TAAIm** concentration. The titration was performed twice – the reported binding constant is the mean, and the uncertainty is the standard deviation.

The binding of **TAAIm** was also tracked with ^{1}H NMR spectroscopy (at [**TAAIm-AlPorF$_{20}$C$_{60}$**] ≈ 5 mM). With the addition of one equivalent of **TAAIm** to an NMR sample of **AlPorF$_{20}$C$_{60}$**, the **TAAIm** protons are shielded, confirming that binding takes place (Figure 2.14). The protons nearest the porphyrin (*j, k, m* and *n*) are shielded more than the protons which are further from the porphyrin (*h, i* and *l*). Proton *o* is unaccounted for in the ^{1}H NMR spectrum, likely due to peak broadening (the other **TAAIm** peaks broaden upon coordination).

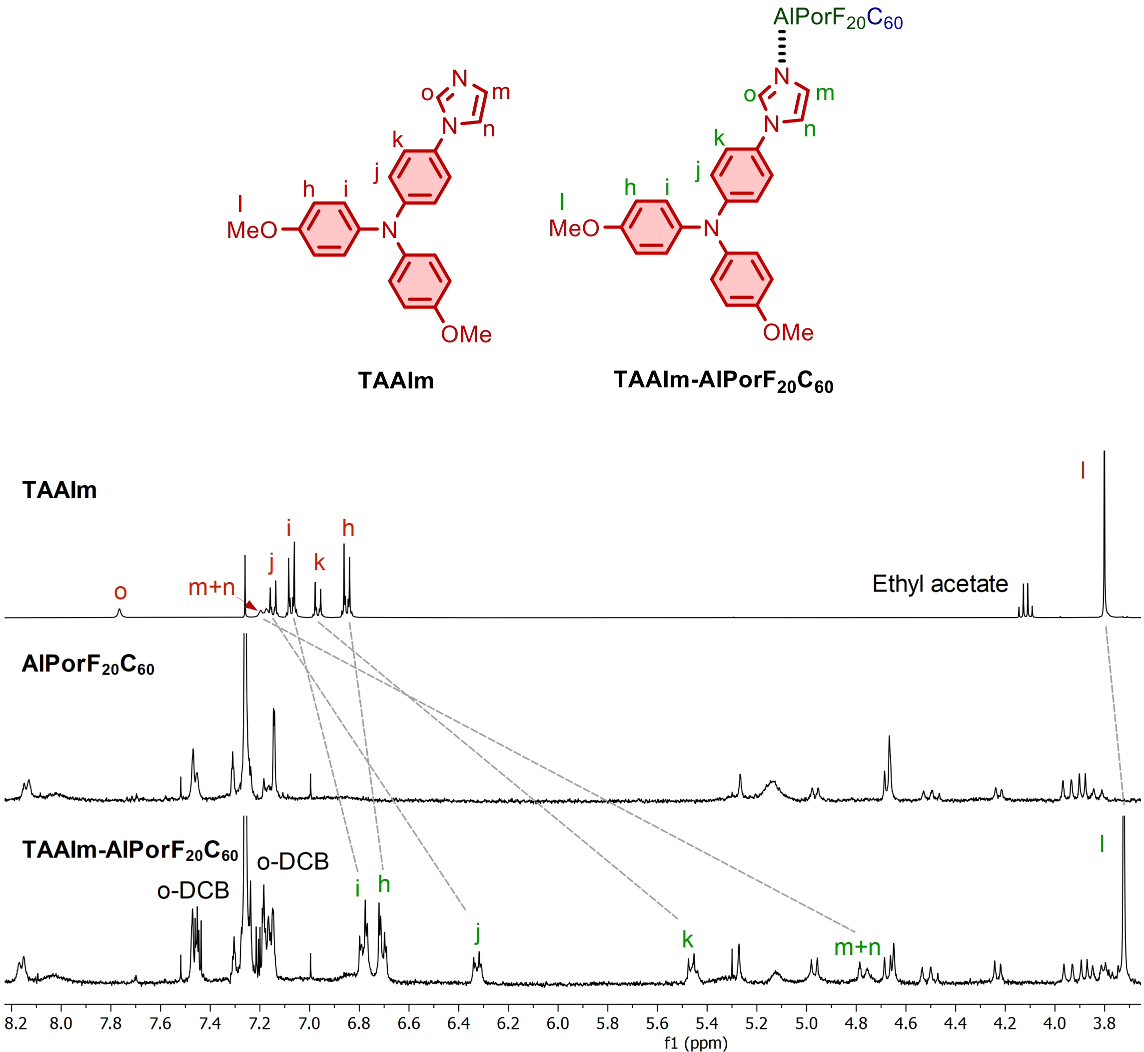

Figure 2.14 ^{1}H NMR (400 MHz, CDCl$_3$, 298 K) spectra of **TAAIm**, **AlPorF$_{20}$C$_{60}$**, and the triad **TAAIm-AlPorF$_{20}$C$_{60}$**. The shielding of the **TAAIm** protons in the triad is illustrated with dashed lines.

3 Investigating Radical Pairs in Aluminium Porphyrin Complexes

Fluorescence and transient absorption spectroscopy were performed on the porphyrin complexes to investigate PET – key in the formation of a SCRP for magnetic sensing.

3.1 Introduction to Fluorescence in Triads

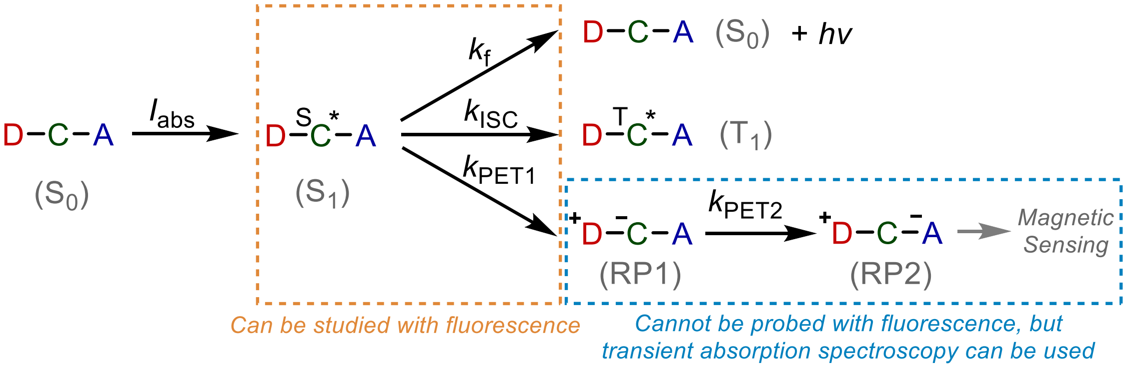

Figure 3.1 Simplified scheme showing the photochemical pathways of a donor-chromophore-acceptor (D-C-A) triad. For simplicity, the only S_1 decay processes are fluorescence (f), intersystem crossing (ISC) and photoinduced electron transfer (PET). I_{abs} is the rate of photon absorption. The order of sequential PET is assumed to be D→C followed by C→A, but the opposite ordering is also possible.

In triads, PET produces fluorescence quenching by introducing an additional pathway for the decay of the first excited chromophore state, S_1 (Figure 3.1).[23,31] When $k_{\mathrm{PET1}} \neq 0$, the fluorescence quantum yield, Φ_{f}, decreases (Equation 3.1). The decrease in Φ_{f} can be monitored experimentally through a decrease in the steady-state fluorescence intensity.

$$\Phi_{\mathrm{f}} = \frac{k_{\mathrm{f}}}{k_{\mathrm{f}} + k_{\mathrm{ISC}} + k_{\mathrm{PET1}}} \qquad \text{Equation 3.1}$$

The introduction of a PET decay pathway also reduces the fluorescence lifetime, τ_f (Equation 3.2). Experimentally, fluorescence lifetimes are obtained by fitting exponential decays (of the form of Equation 3.2) to time-correlated single photon counting (TCSPC) measurements.

$$I(t) = I(0)\exp[-(k_\mathrm{f} + k_\mathrm{ISC} + k_\mathrm{PET1})t] = I(0)\exp\left[-\frac{t}{\tau_\mathrm{f}}\right] \qquad \text{Equation 3.2}$$

where $I(t)$ = fluorescence intensity at time t, and $\tau_\mathrm{f} = \frac{1}{k_\mathrm{f} + k_\mathrm{ISC} + k_\mathrm{PET1}} = \Phi_\mathrm{f}\,\tau_{natural}$.

3.2 Steady-State Fluorescence Spectroscopy

3.2.1 Mirror Image Emission Spectrum

Photoexcitation of aluminium porphyrin complexes in the Q-band produces a mirror image emission spectrum (Figure 3.2). To confirm that the emission arises from the porphyrin, an excitation scan was performed (Figure 3.2). The similarity between the absorption and excitation spectra of **AlPorF$_{20}$C$_{60}$** confirms that the emissive species is indeed the porphyrin, and not a fluorescent impurity.

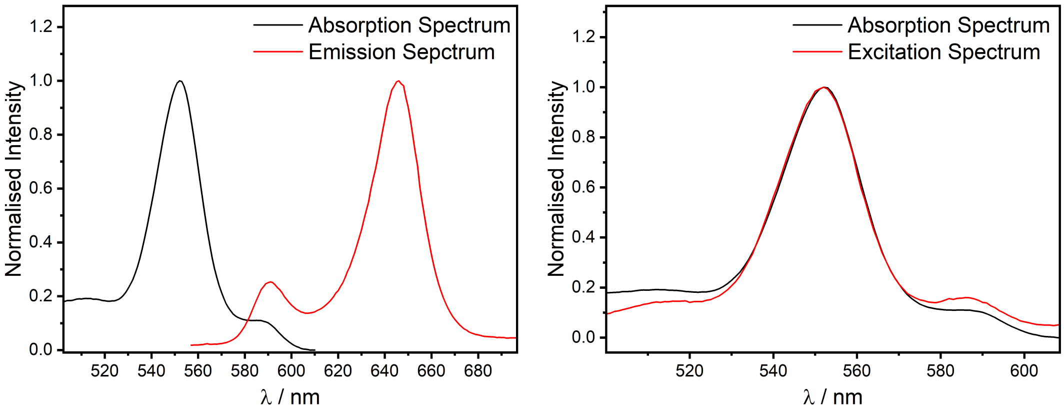

Figure 3.2 Left: Overlayed UV-Vis and emission spectra (o-DCB, 293 K, λ_{ex} = 550 nm) of **AlPorF$_{20}$C$_{60}$**, showing the mirror image relationship. Right: Overlayed UV-Vis and excitation spectra (o-DCB, 293 K) of **AlPorF$_{20}$C$_{60}$**, showing the absorption contribution of the fluorescent species to the UV-Vis spectrum. For the excitation scan, λ_{det} = 650 nm (peak of the emission spectrum).

3.2.2 Fluorescence Quenching in the Triad

To investigate fluorescence quenching in the triad, a simultaneous UV-Vis and fluorescence titration was performed. In this experiment, [**TAAIm**] was raised through successive additions to a solution of **AlPorF$_{20}$C$_{60}$**. Binding of **TAAIm** was tracked by UV-Vis, and quantified by fitting the data to a 1:1 binding isotherm (to give percentage binding). For each addition, an emission spectrum was recorded, with the excitation wavelength fixed at the isosbestic point in the Q-band. At this excitation wavelength, the extinction coefficients of the bound and unbound species are equal, and so fluorescence quenching could be tracked through the relative emission intensity. To quantify this, the quenching efficiency (QE) was defined as: $\mathrm{QE} = 1 - \frac{\int I_x(\upsilon)d\upsilon}{\int I_0(\upsilon)d\upsilon}$ where $\int I_x(\upsilon)d\upsilon$ is the integrated fluorescence emission intensity at a given point of the titration and $\int I_0(\upsilon)d\upsilon$ is the integrated fluorescence emission intensity at the first point of the titration.

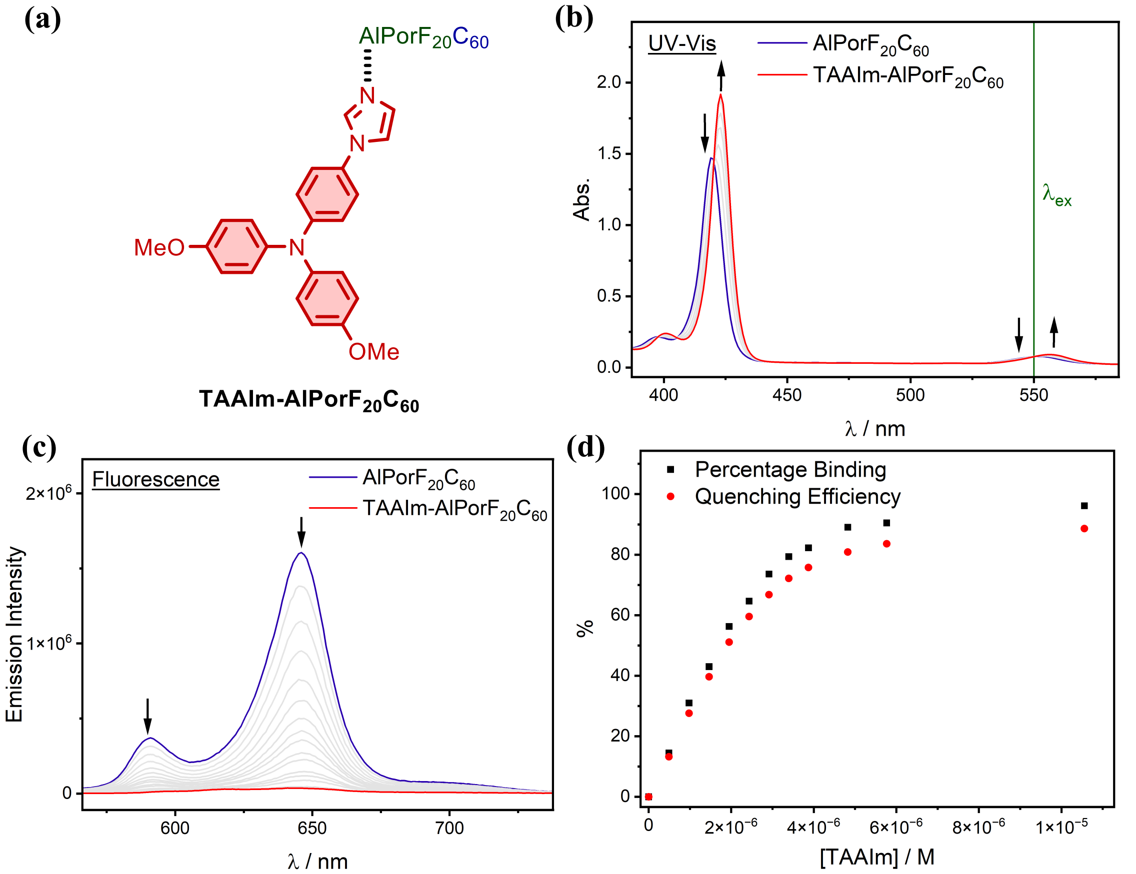

Figure 3.3 (a) Structure of **TAAIm-AlPorF$_{20}$C$_{60}$**. (b) UV-Vis (o-DCB, 293 K) titration of **AlPorF$_{20}$C$_{60}$** (c.a. 3.0 μM) with **TAAIm**, added up to 10.5 μM in 0.5 μM increments. The fluorescence excitation wavelength is illustrated with the green line at 550 nm, at the isosbestic point in the Q band. (c) Fluorescence (o-DCB, 293 K, $\lambda_{ex} = 550$ nm) titration of **AlPorF$_{20}$C$_{60}$** with **TAAIm**, showing the emission spectrum at each point. (d) Plot of the percentage binding and quenching efficiency against concentration of **TAAIm**. Percentage binding and quenching efficiency were calculated as described above.

The titration shows that as the percentage of bound **TAAIm-AlPorF$_{20}$C$_{60}$** increases, QE increases with a similar trend (Figure 3.3). This suggests that an intramolecular fluorescence quenching process exists in **TAAIm-AlPorF$_{20}$C$_{60}$**, which is assigned to the initial PET step, PET1, guided by the TA measurements later in this chapter. At each point of the titration, $\frac{\mathrm{QE}}{\mathrm{Percentage\ Binding}} \approx 92\%$, which gives an indication of the intrinsic quenching efficiency of the purely bound triad. Importantly, this titration alone does not provide direct evidence of PET – other intramolecular quenching processes, such as singlet-singlet energy transfer, are plausible.

As a reference, the same titration was performed with 1-methylimidazole (Figure 3.4). Minimal fluorescence quenching was observed, showing that it is not simply the presence of a Lewis base that leads to fluorescence quenching. Instead, these results imply that fluorescence quenching is caused by the electron-donating ability of **TAAIm**, which is further indirect evidence to support a PET-based fluorescence quenching mechanism.

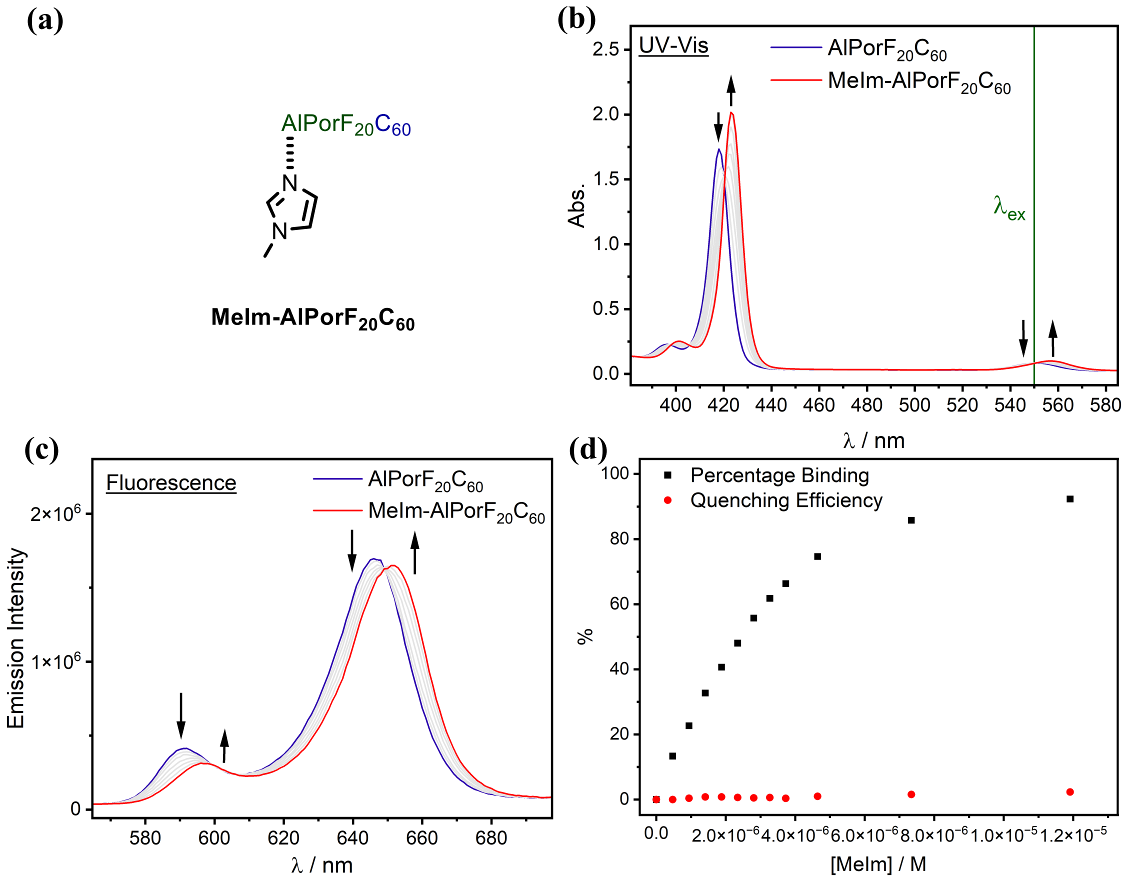

Figure 3.4 (a) Structure of **MeIm-AlPorF$_{20}$C$_{60}$**. (b) UV-Vis (o-DCB, 293 K) titration of **AlPorF$_{20}$C$_{60}$** (c.a. 3.0 μM) with **MeIm**, added up to 12.0 μM in 0.5 μM increments. The fluorescence excitation wavelength is illustrated with the green line at 550 nm, at the isosbestic point in the Q band. (c) Fluorescence (o-DCB, 293 K, λ_{ex} = 550 nm) titration of **AlPorF$_{20}$C$_{60}$** with **MeIm**, showing the emission spectrum at each point. (d) Plot of the percentage binding and quenching efficiency against concentration of **MeIm**. Percentage binding and quenching efficiency were calculated as described above.

To rule out a collisional, intermolecular fluorescence quenching process, the non-coordinating donor **TAA** was added to a solution of **AlPorF$_{20}$C$_{60}$** (Figure 3.5). Minimal fluorescence quenching was observed with equivalent concentrations of **TAA**, which confirms that the fluorescence quenching process in the triad is intramolecular.

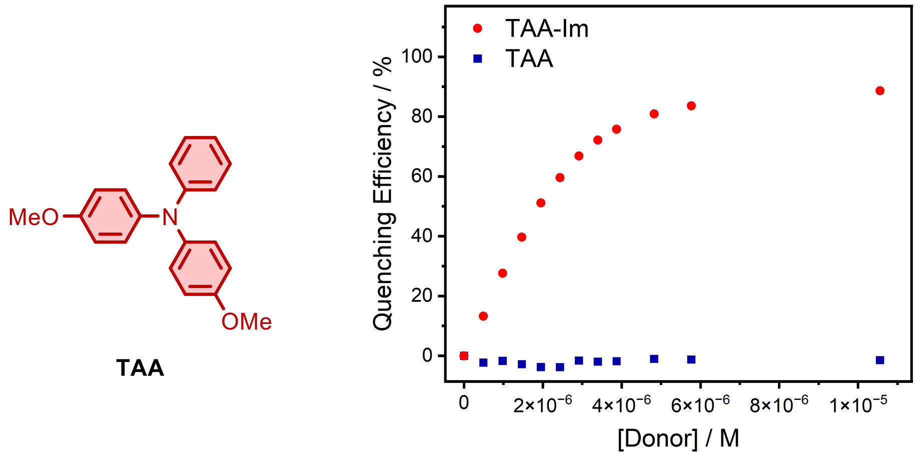

Figure 3.5 Left: Structure of the non-coordinating donor **TAA**. The synthesis of **TAA** is described in the appendix. Right: Plot showing quenching efficiency with increasing concentrations of **TAA** and **TAAIm** in a solution of **AlPorF₂₀C₆₀** at 3.0 μM (o-DCB, 293 K, λ_{ex} = 550 nm).

All the above measurements were carried out in 1,2-dichlorobenzene (o-DCB) – a polar, non-coordinating solvent with precedent for use with similar triads.[26] In toluene, which has a lower dielectric constant, minimal fluorescence quenching was observed (Figure 3.6), despite UV-Vis suggesting comparable binding strength. The dependence of fluorescence quenching on solvent polarity is consistent with PET: k_{PET1} is faster in more polar solvents due to the stabilisation of the charge-separated state.

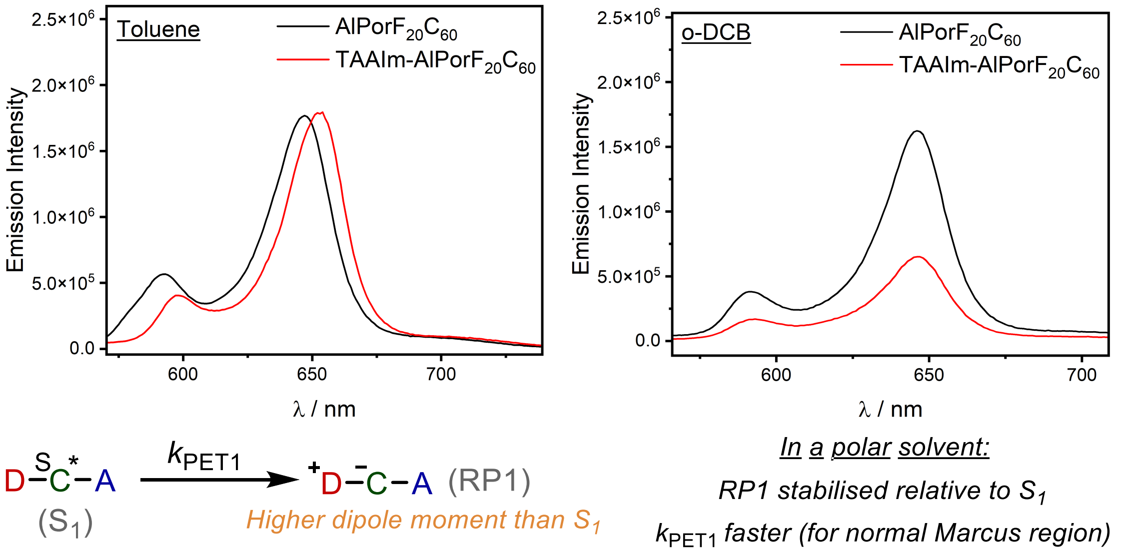

Figure 3.6 Comparison of fluorescence quenching in toluene and o-DCB, featuring the emission spectra (293 K, λ_{ex} = 550 nm) of **AlPorF₂₀C₆₀** (c.a. 3.0 μM) with the addition of 3.0 μM of **TAAIm**. The illustration shows the stabilisation of the charge-separated state formed through PET.

3.2.3 Fluorescence Quantum Yields

To quantify fluorescence quenching, fluorescence quantum yields were measured using absolute and relative methods. Absolute quantum yields were measured with an integrating sphere, which provides standard-less quantification, but produces poor accuracy when $\Phi_\mathrm{f} < 5\%$. In the relative method, each compound's steady-state emission intensity was compared to that of zinc tetraphenylporphyrin, **ZnTPP** ($\Phi_\mathrm{f} = 3.3\%$ in toluene)[32], using:

$$\Phi_\mathrm{f}^{X} = \Phi_\mathrm{f}^{St}\left(\frac{Abs_{St}}{Abs_X}\right)\left(\frac{\int I_X(v)\,dv}{\int I_{St}(v)\,dv}\right)\left(\frac{{n_x}^2}{{n_{St}}^2}\right) \qquad \text{Equation 3.3}$$

where X and St are the compound and standard respectively; Φ_f^{i} is the fluorescence quantum yield of compound i; Abs_i is the absorbance for compound i at the excitation wavelength (550 nm); $\int I_i(v)\,dv$ is the integrated emission intensity for compound i; and n_i is the refractive index of the solvent in which compound i was measured in. The measured quantum yields are summarised in Table 3.1. The quenching efficiency is redefined relative to **AlPorF$_{20}$Ph**: $\mathrm{QE} = 1 - \frac{\Phi_\mathrm{f}}{\Phi_\mathrm{f}(\mathrm{AlPorF_{20}Ph})}$.

Table 3.1 Fluorescence quantum yields for the triad, dyad and a reference complex, measured with absolute and relative methods. Measurements were performed (o-DCB, 293 K, $\lambda_{ex} = 550$ nm) at c.a. 5 µM. **TAAIm-AlPorF$_{20}$C$_{60}$** was prepared by addition of **TAAIm** up to 9 µM in a solution of **AlPorF$_{20}$C$_{60}$** at 5 µM. The averages were calculated by taking the mean, with the standard deviation reported as the uncertainty. Quenching efficiency (QE) is defined above, and its uncertainty was calculated using error propagation.

Compound	**Absolute Method**	**Relative Method**	**Average**	
	Φ_f	Φ_f	Φ_f	QE
AlPorF$_{20}$Ph	4.7 %	5.3%	5.0 ± 0.4 %	0 %
AlPorF$_{20}$C$_{60}$	4.0 %	4.7%	4.4 ± 0.5 %	13 ± 2 %
TAAIm-AlPorF$_{20}$C$_{60}$	0.6 %	0.3%	0.5 ± 0.2 %	91 ± 4 %

A high degree of uncertainty arises from the absolute quantum yields because $\Phi_\mathrm{f} < 5\%$.

However, a similar fluorescence quenching trend is found with both methods. Minimal fluorescence quenching was observed for **AlPorF$_{20}$C$_{60}$** relative to **AlPorF$_{20}$Ph**, which suggests that the fullerene electron acceptor is ineffective in producing PET in the porphyrin-acceptor dyad. In contrast, a high QE was found for **TAAIm-AlPorF$_{20}$C$_{60}$**, consistent with the previous quenching titration. The accuracy of Φ_f(Triad) risks being compromised by the emission contribution of unbound **AlPorF$_{20}$C$_{60}$** (which has higher Φ_f). However, relative to **AlPorF$_{20}$C$_{60}$**, QE(Triad) = 89 ± 4%, which is close to the intrinsic (purely bound) QE value of 92% calculated by titration (Figure 3.3). This suggests that unbound **AlPorF$_{20}$C$_{60}$** had a negligible impact on Φ_f(Triad) accuracy.

3.3 Time-Correlated Single Photon Counting

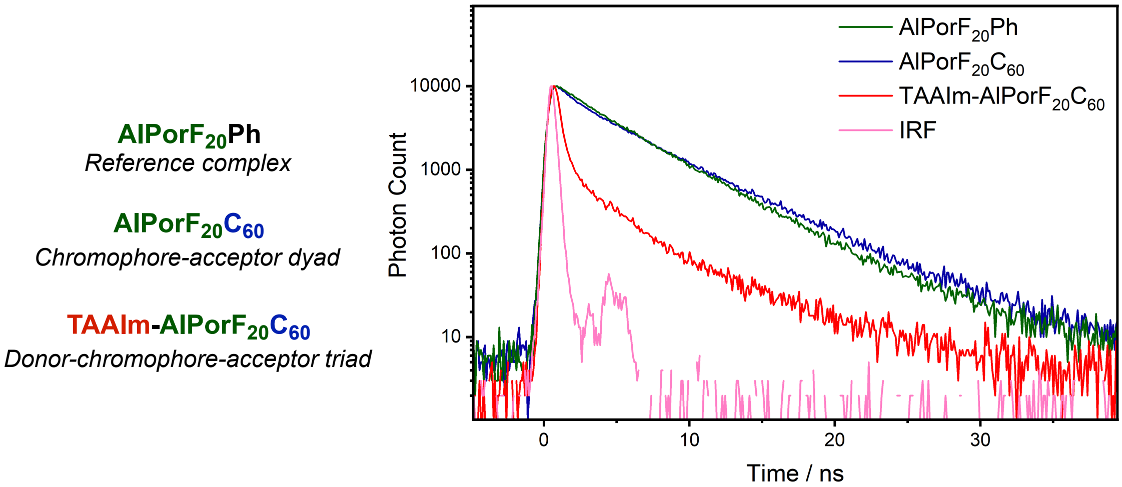

Figure 3.7 Fluorescence decay curves for **AlPorF$_{20}$Ph**, **AlPorF$_{20}$C$_{60}$**, and **TAAIm-AlPorF$_{20}$C$_{60}$**. The data were recorded using TCSPC (o-DCB, 293 K, λ_{ex} = 473 nm, λ_{det} = 650 nm). **TAAIm-AlPorF$_{20}$C$_{60}$** was prepared by addition of **TAAIm** up to 1 mM in a solution of **AlPorF$_{20}$C$_{60}$** at 5 µM. The instrument response function (IRF) is shown in pink.

The kinetics of PET were characterised with TCPSC. The fluorescence decay curve of **TAAIm-AlPorF$_{20}$C$_{60}$** shows a stark contrast to those of **AlPorF$_{20}$Ph** and **AlPorF$_{20}$C$_{60}$** (Figure 3.7). With **TAAIm-AlPorF$_{20}$C$_{60}$**, the logarithmic scale highlights the existence of a fast-decaying component (the triad), as well as a minor slow-decaying component which is assumed to be unbound **AlPorF$_{20}$C$_{60}$**. The faster fluorescence decay for the triad is a consequence of quenching due to rapid PET. The comparable decay gradients for

AlPorF₂₀Ph and **AlPorF₂₀C₆₀** suggest that Φ_{PET} is low for **AlPorF₂₀C₆₀**. These results are qualitatively consistent with the trend in quantum yields.

Fluorescence lifetimes were extracted by fitting exponential decays to the experimental data. As the lifetimes are comparable with the instrument response, the theoretical decay was reconvoluted with the IRF during fitting. The fitted exponential decays take the form:

$$I(t) = A + B_1 e^{-t/\tau_1} + B_2 e^{-t/\tau_2} + \cdots B_n e^{-t/\tau_n} \qquad \text{Equation 3.4}$$

where $I(t)$ is the emission intensity at time t; B_n is the initial intensity of fluorescent species n; and τ_n is the fluorescence lifetime of fluorescent species n.

Table 3.2 Fluorescence lifetimes and decay amplitudes for the triad, dyad and a reference complex. The parameters were extracted by fitting exponential decays to the TCSPC data (in Figure 3.7) with IRF reconvolution. $\sum B_n$ has been normalised to unity. The reported uncertainties are the standard deviations of the fitted parameters.

Compound	B_1	τ_1 / ns	B_2	τ_2 / ns
AlPorF₂₀Ph	1	4.25 ± 0.01	n/a	n/a
AlPorF₂₀C₆₀	1	4.61 ± 0.01	n/a	n/a
TAAIm-AlPorF₂₀C₆₀	0.96	0.40 ± 0.01	0.04	4.44 ± 0.04

The decay curves of **AlPorF₂₀Ph** and **AlPorF₂₀C₆₀** were fit with monoexponential functions. Their fluorescence lifetimes are comparable, which is consistent with the lack of fluorescence quenching in **AlPorF₂₀C₆₀**. The curve of **TAAIm-AlPorF₂₀C₆₀** was fit with a biexponential decay. The fast-decaying component with 96% amplitude is assigned to the bound triad. The slow-decaying component with 4% amplitude is assigned to the unbound **AlPorF₂₀C₆₀**, and this is confirmed by comparison of the fluorescence lifetimes (4.44 and 4.61 ns). With these results, an estimate for k_{PET1} can be calculated:

$$k_{\mathrm{PET1}} \approx \frac{1}{\tau_{\mathrm{f}}^{\mathrm{Triad}}} - \frac{1}{\tau_{\mathrm{f}}^{\mathrm{Reference}}} = \frac{1}{0.40} - \frac{1}{4.25} = 2.26 \pm 0.06\ \mathrm{ns}^{-1}$$

This value should only be interpreted as an estimate – the values of B_n and τ_n are correlated, which makes them difficult to accurately determine through fitting.

3.4 Transient Absorption Spectroscopy

To complement the fluorescence measurements, transient absorption (TA) spectroscopy was performed on **AlPorF$_{20}$C$_{60}$** and **TAAIm-AlPorF$_{20}$C$_{60}$**. These spectra were kindly measured and processed by Damyan Frantzov and Dr Kevin Henbest (Timmel group).

3.4.1 Introduction to TA Spectroscopy

Although fluorescence can provide indirect evidence of PET, it provides no information about the fate of an excited state molecule following PET. TA spectroscopy provides direct evidence for the different transient species formed after photoexcitation. Experimentally, this is achieved by photoexciting a sample with a pump laser beam, and then transiently recording the absorption spectrum of the sample with a probe laser beam. Subtraction of the ground state absorption spectrum from the transiently recorded spectra gives the absorbance difference, ΔA, as a function of time after laser excitation. Transient excited state species can be identified in the ΔA spectra through their characteristic spectral signatures. The signature of a radical pair, formed through PET, consists of the absorption profiles of a donor-based radical cation and an acceptor-based radical anion.

3.4.2 **AlPorF$_{20}$C$_{60}$** *(Chromophore-Acceptor Dyad)*

The TA spectrum of **AlPorF$_{20}$C$_{60}$** is shown in Figure 3.8. There is no evidence of PET to form a radical pair (no porphyrin cation signal at c.a. 650 nm), which is consistent with its lack of fluorescence quenching. At early times, the intense signal at 455 nm is assigned to the porphyrin S_1, through comparison with the literature for tetraarylporphyrins.[33] The kinetic profile shows the decay of the S_1 state, and the presence of a longer-lived species,

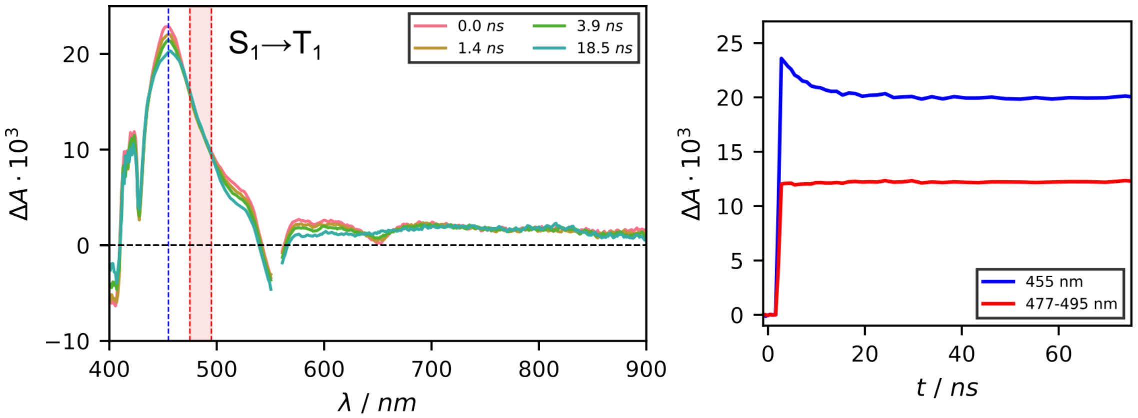

Figure 3.8 Left: TA spectrum (o-DCB, 293 K, λ_{ex} = 551 nm) of **AlPorF$_{20}$C$_{60}$**. The blue dotted line indicates the wavelength at the peak of the porphyrin S$_1$ band. The red shaded window indicates the isosbestic region, which confirms that the broad T$_1$ band at 18.5 ns is formed from the porphyrin S$_1$. Right: Kinetic profile showing the decay of S$_1$ into a longer-lived T$_1$ (in blue). The isosbestic behaviour at 477-495 nm is shown in red.

also absorbing at 455 nm, which has a slightly broader signal in the ΔA spectrum. This longer-lived state is assigned to the porphyrin T$_1$. The presence of isosbestic behaviour at 477-495 nm confirms that the T$_1$ state is formed from S$_1$ through intersystem crossing. The rate of decay of S$_1$ into T$_1$ is comparable with the fluorescence lifetime (on the order of nanoseconds). The porphyrin T$_1$ state is further investigated in Chapter 4.

3.4.3 **TAAIm-AlPorF$_{20}$C$_{60}$** (*Donor-Chromophore-Acceptor Triad)*

The TA spectrum of **TAAIm-AlPorF$_{20}$C$_{60}$** is shown in Figure 3.9. For the triad there is evidence of a radial pair, which is consistent with the fluorescence evidence for PET. The radical pair is identified in the early-time spectra (0-0.6 ns) by the broad peak at 780 nm, which corresponds to the radical cation of the **TAAIm** donor. To confirm this assignment, a UV-Vis spectrum of **TAAIm** was recorded following oxidation by **Thianthrenium BArF$_{20}$** (structure shown in Figure 3.9, synthesised by Dr Arnau Rubio[34]). The signal for a fullerene radical anion is typically found at ~1080 nm,[35] outside of the detection range of this experiment.

The existence of the radical cation from 0-0.6 ns indicates that PET1 is rapid relative to the time resolution of the experiment. This is consistent with the value of k_{PET1} estimated from the fluorescence lifetimes ($k_{\mathrm{PET1}} = 2.26\ \mathrm{ns}^{-1}$). The radical cation signal vanishes within a nanosecond, which is attributed to rapid radical pair recombination at the time resolution of this experiment. Consequently, the radical pair lifetime cannot be extracted from the data, but evidently $\tau_{\mathrm{RP1}} < 1$ ns.

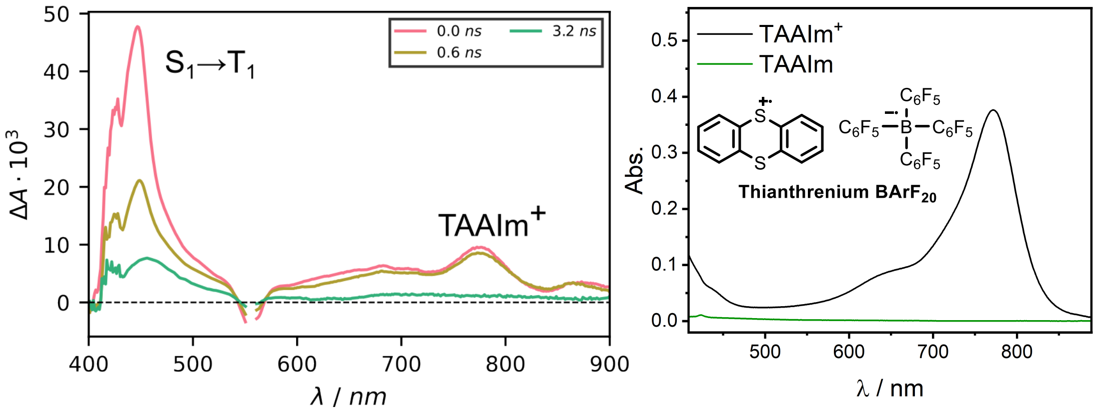

Figure 3.9 Left: TA spectrum (o-DCB, 293 K, $\lambda_{ex} = 557$ nm) of **TAAIm-AlPorF$_{20}$C$_{60}$**. At 455 nm, an intense porphyrin S_1 is present at 0 ns, which decays rapidly to a weak, broad T_1 band. At 780 nm, a broad feature if present at 0-0.6 ns which corresponds to the radical cation of the **TAAIm** donor. Right: UV-Vis spectrum (o-DCB, 293 K) showing the radical cation of **TAAIm**, formed through oxidation by **Thianthrenium BArF$_{20}$**. The spectrum of **TAAIm** at the same concentration is overlayed for reference.

At 0 ns, the porphyrin S_1 signal is present at 455 nm, as observed with **AlPorF$_{20}$C$_{60}$**. However, the decay of S_1 into T_1 yields a much less intense T_1 signal (relative to the peak S_1 intensity) in the triad. This is consistent with a lower Φ_{ISC} due to PET.

3.5 Summary and Discussion

Table 3.3 Summary of the key results from this chapter. The quenching efficiency is defined relative to **AlPorF$_{20}$Ph** as above. The listed τ_f values are for the major components of the fitted decay curves.

Compound	**Fluorescence**			**TA**	
	Quenching Efficiency	τ_f / ns	Quenching Observations	Radical Pair?	τ_{RP1}
AlPorF$_{20}$Ph	0 %	4.25 ± 0.01	n/a	n/a	n/a
AlPorF$_{20}$C$_{60}$	13 ± 2 %	4.61 ± 0.01	n/a	No	n/a
TAAIm-AlPorF$_{20}$C$_{60}$	91 ± 4 %	0.40 ± 0.01	Intramolecular, solvent-dependent	Yes	< 1 ns

These measurements demonstrate that the fluorescence of the triad **TAAIm-AlPorF$_{20}$C$_{60}$** is quenched relative to the reference **AlPorF$_{20}$Ph**. The quenching process is intramolecular, reduces τ_f, and its rate is influenced by solvent polarity – all indicative of PET. This conclusion is supported by TA spectroscopy, which suggests that PET occurs to form a radical pair which recombines within a nanosecond at room temperature.

We speculate that the rapid rate of radical recombination (< 1 ns) is due to slow electron transfer of the porphyrin radical anion to the fullerene (Figure 3.10). The low quantum yield of PET2 is supported by the lack of evidence for radical pair formation in **AlPorF$_{20}$C$_{60}$**. Literature redox potentials have been used to estimate the photochemical energy levels.[26] The poor thermodynamic driving force for PET2 is a potential reason for its poor quantum yield, and it suggests that C_{60} is an ineffective acceptor in this system.

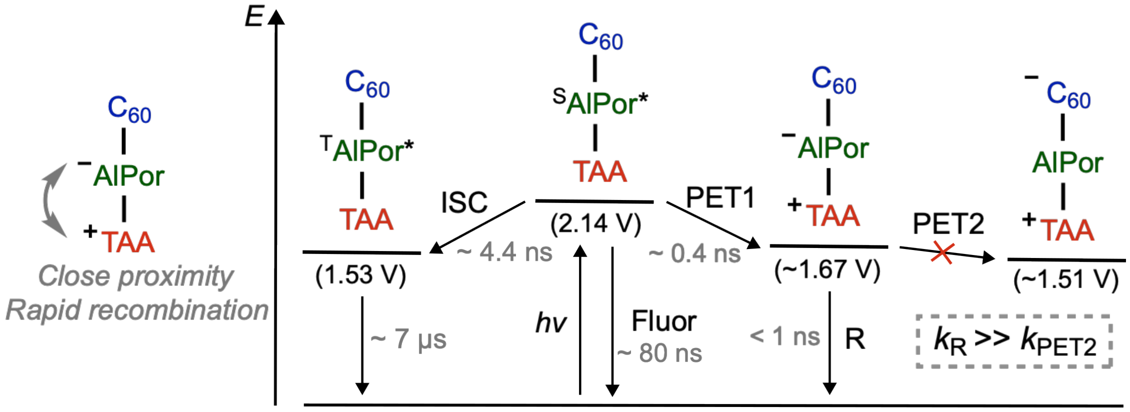

Figure 3.10 Photochemical scheme for the triad **TAAIm-AlPorF$_{20}$C$_{60}$** in o-DCB, based on the results of this chapter. The estimated lifetimes for each process are shown in grey. The natural lifetime is estimated from $\tau_f = \Phi_f\,\tau_{natural}$. The triplet lifetime is estimated from the TA spectrum of **AlPorF$_{20}$C$_{60}$**. Literature redox potentials have been used to estimate the energy level values relative to the ground state.[26] Energetic stabilisation arising from the electrostatics of the radical pairs, as described by the Weller equation, has been neglected as it is assumed to be negligible for the > 1 nm separated radicals.

The SCRPs generated in a triad must live for at least 100 ns to display magnetic field effects (see Chapter 1).[8] Therefore, this triad does not meet the molecular compass criteria. To inform the future molecular design of aluminium porphyrin compasses, it is important to understand why the structure of this triad produces a short radical pair lifetime. The above hypothesis suggests that the fullerene acceptor is ineffective in producing PET. In Chapter 4, this hypothesis is further investigated through the study of photogenerated triplets by transient electron spin resonance spectroscopy.

4 Investigating Triplet States in Aluminium Porphyrin Complexes

In Chapter 3, the triad was shown to undergo PET, generating a radical pair which rapidly recombines (within 1 ns) at room temperature. To further investigate the structural factors influencing this behaviour, transient electron spin resonance (trESR) spectroscopy was performed on both the triad and reference complexes. This research was conducted in collaboration with Dr Gabriel Moise and Damyan Frantzov (from the Timmel group).

4.1 Introduction to trESR

ESR is a class of spectroscopic techniques which probe transitions between the spin levels of a paramagnetic molecule in a magnetic field. These techniques enable the characterisation of both the electronic and spatial structure of a paramagnetic species.

In the presence of an external magnetic field, the M_S spin states of a molecule (with spin S) are split by the Zeeman interaction. Importantly, further energy level splittings arise due to electron-electron interactions and electron-nuclear hyperfine interactions.[36] In continuous-wave (CW) ESR, the transitions between these spin states are measured as a function of magnetic field strength, typically under continuous microwave irradiation at a fixed frequency. The parameters that govern the different spin interactions are then extracted from ESR spectra using numerical simulations of the spin energy levels.[37]

For the study of short-lived photogenerated paramagnetic species, a variation of CW ESR, named transient ESR, can be used to measure the ESR spectra as a function of time following a laser pulse. Due to the absence of phase-sensitive detection (by field modulation), trESR is usually unable to resolve signals from paramagnetic species in a Boltzmann state. However, trESR is sensitive to species which are highly spin polarised.

Spin polarisation refers to non-equilibrium and large population differences of spin states. In the presence of spin polarisation, ESR transitions can be absorptive and emissive (as opposed to the conventional ESR spectra of thermalised radicals which are purely absorptive). The spin polarised sublevel populations contain information about the mechanism through which a paramagnetic species is formed.[36] For example, spin polarisation emerges during the formation of molecular triplet states by spin-orbit coupling mediated intersystem crossing (ISC).[38]

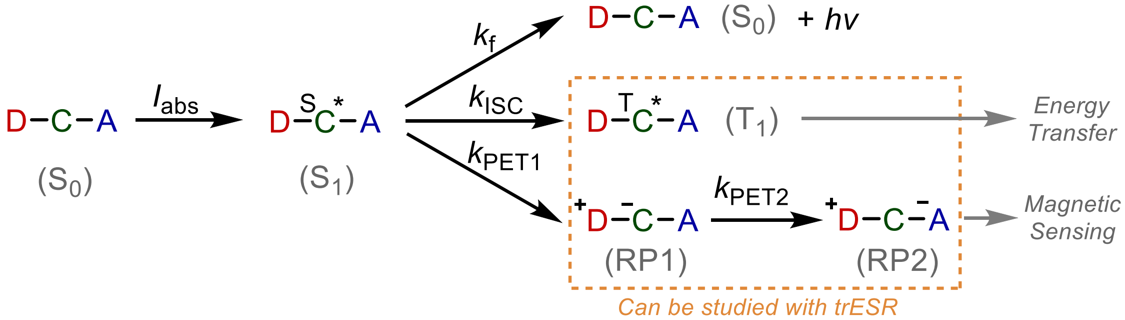

Figure 4.1 Simplified scheme showing the photochemical pathways of a donor-chromophore-acceptor (D-C-A) triad. For simplicity, the only S_1 decay processes are fluorescence (f), intersystem crossing (ISC) and photoinduced electron transfer (PET). I_{abs} is the rate of photon absorption. The order of sequential PET is assumed to be D→C followed by C→A, but the opposite ordering is also possible.

For triads, SCRPs can be observed by trESR if they are sufficiently long-lived, as the experimental time resolution is typically c.a. 10 ns.[39] The typical spectral features of a singlet-born SCRP are a pair of narrow emissive/absorptive doublets.[40,41] However, based on the results of Chapter 3, the radical pair formed in **TAAIm-AlPorF$_{20}$C$_{60}$** is too short-lived (< 1 ns) to be detected by trESR. In the absence of SCRP signatures, trESR can still be used to characterise the photophysics of a triad by measuring triplet states (Figure 4.1). For instance, if one of the triad components (eg. the chromophore) undergoes ISC to form a triplet, followed by energy transfer to generate a triplet on a different component (eg. the acceptor), then the latter will inherit the spin polarisation of the former.[42]

The trESR spectrum of a spin polarised triplet is easily distinguishable from that of a SCRP. The measurements in this thesis were performed with frozen solutions, and in this case, transitions are probed in molecules with all possible orientations with respect to the external magnetic field. Consequently, the triplet trESR spectrum typically features six turning points (two transitions for each of the three canonical directions as in Figure 4.2). The absorptive/emissive (A/E) pattern depends on the spin polarisation. The triplet spectral shape is further influenced by dipolar electron-electron interactions, commonly referred to as the zero-field splitting (ZFS). This splitting is defined by the ZFS parameters D and E. The magnitude of D is related to the electron-electron distance ($D \propto \langle\frac{1}{r^3}\rangle$), and the magnitude of E is related to the axial symmetry of the electron distribution ($E \propto \langle\frac{y^2-x^2}{r^5}\rangle$), where r is the distance between electron spins and x/y are the components of the interspin vector relative to the axis of maximum dipolar coupling (z).[36]

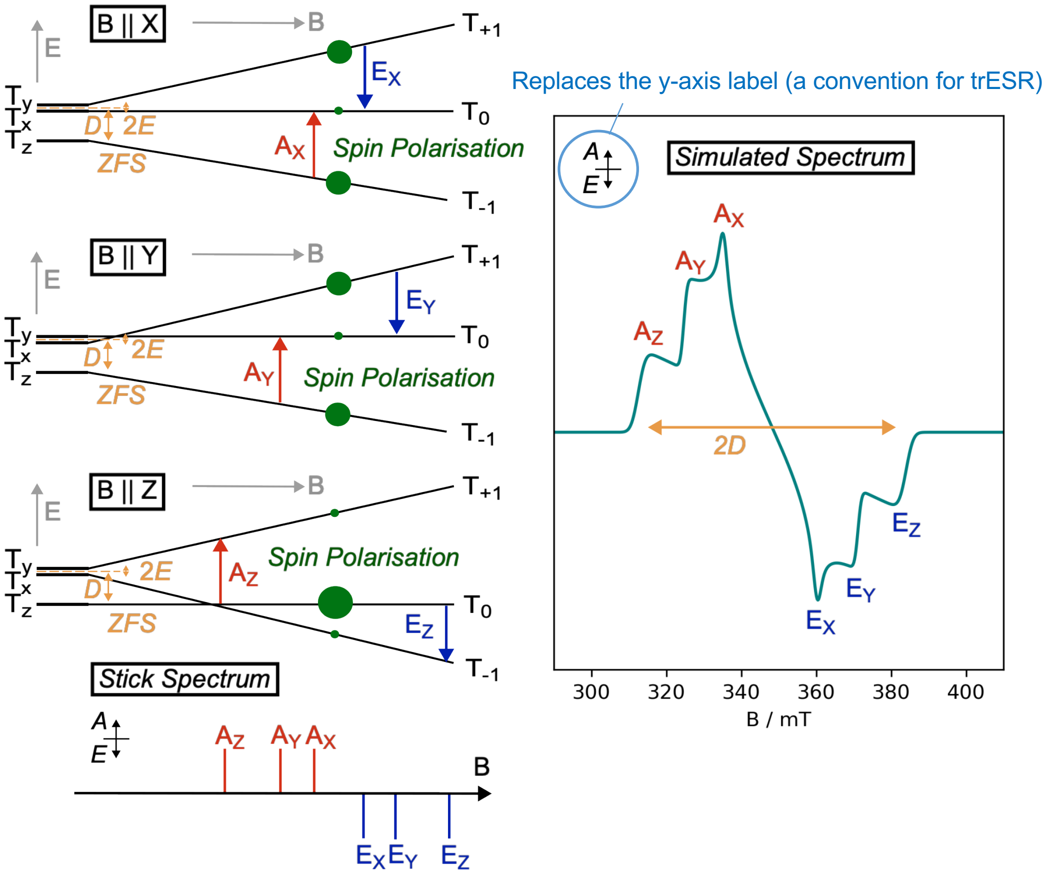

Figure 4.2 Left: energy level diagram for a molecular triplet ($S = 1$) in the presence of an externnal magnetic field aligned along the X, Y and Z molecular axes. The triplet sublevels are split by the Zeeman interaction as B increases. The zero-field splitting parameters of the triplet sublevels are shown in yellow. The spin polarisation of the ZFS sublevels ($P_X : P_Y : P_Z = 0 : 0 : 1$) is illustrated by the relative sizes of the green circles. The absorptive (A) and emissive (E) transitions in the field-domain spectrum (at fixed microwave frequency) are shown in red and blue. Right: simulated triplet spectrum ($D > 0$, $E > 0$, $P_X{:}P_Y{:}P_Z = 0{:}0{:}1$).

4.2 Triplets States in Aluminium Porphyrin Reference Complexes

Initially, the X-band (9.75 GHz) trESR spectra of the reference complexes **AlPorPh** and **AlPorF$_{20}$Ph** were recorded in 2-methyltetrahydrofuran at 80 K (the samples were degassed and flame sealed). With these spectra, the porphyrin triplets generated by ISC were characterised to facilitate the later assignment of the triad spectra. Additionally, the two trESR spectra were compared to investigate the potential impact of the C_6F_5 *meso*-side chains on the electronic structure of the porphyrin triplet state.

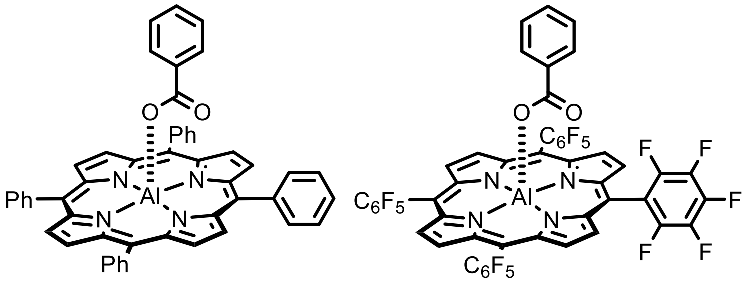

AlPorPh **AlPorF$_{20}$Ph**

Figure 4.3 Reference complexes **AlPorPh** and **AlPorF$_{20}$Ph**. Synthetic schemes are in the appendix.

4.2.1 AlPorPh

The trESR results and numerical simulations for **AlPorPh** are summarised in Figure 4.4 and Table 4.1. The time-dependence of the **AlPorPh** porphyrin triplet spectrum is unusual because the positions of the turning points appear to change through time (illustrated with grey dashed lines in Figure 4.4). For example, the high field maximum at early time (0-0.1 μs) shifts from 364 mT to 375 mT in the late time spectrum (0.4-0.5 μs). Attempts at modelling this kinetic behaviour using a time-dependent ESR simulation algorithm developed by Dr G. Moise (in collaboration with Dr C. Tait) failed to capture these spectral changes. In fact, the change in turning point positions can be reproduced only by employing a mixture of two different triplet spectra in the simulation (Triplet A and Triplet B in Figure 4.4). The best fits obtained with a single triplet simulation are included in the appendix.

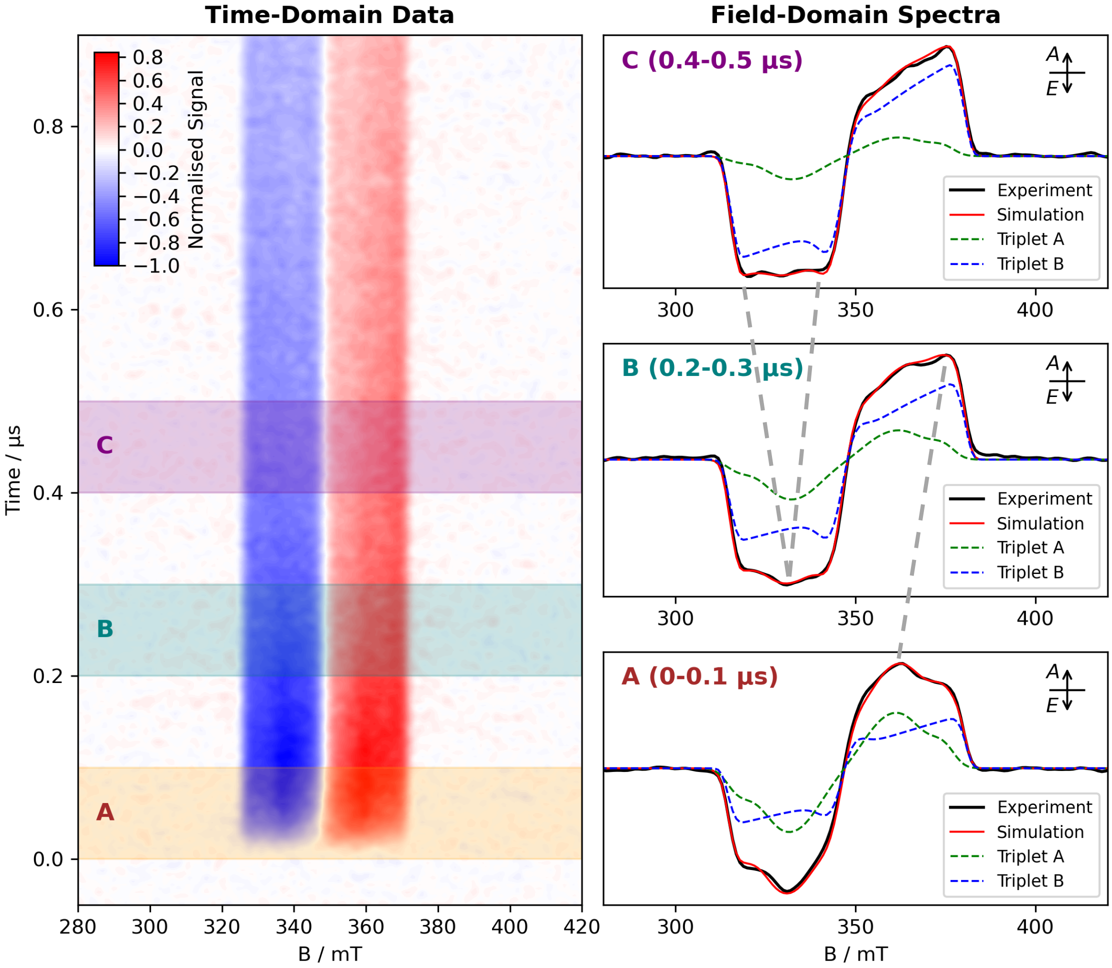

Figure 4.4 Left: trESR spectrum (2-MeTHF, X-band, 80 K, 532 nm, 10 mJ, 50 Hz) of **AlPorPh**, as a function of field and time after the laser pulse. Horizontal bands highlight the integration windows for the spectra on the right. Right: Field-domain spectra averaged over three different time windows after the laser pulse. The experimental signals are shown in black and the simulated signals in red. The contributions of each triplet to the overall simulated spectra are shown with dashed lines. The grey dashed lines highlight the unusual time dependence of the triplet turning points.

The inclusion of two triplets in the simulation was justified in a paper published by Panariti *et al.* during the course of this Part II project.[43,44] In this work, the authors propose that a dynamic Jahn-Teller effect produces two closely lying triplet states in metalloporphyrins with D_{4h} symmetry. The Panariti model features a thermally accessible vibrational mode that interconverts the two triplet states (Figure 4.5), and hence the effect is described as dynamic. The vibrational mode lifts the degeneracy of the E_u triplet and interconverts the ZFS axes, changing the sign of the ZFS parameter *E* between the two triplets (Figure 4.5).[43,44]

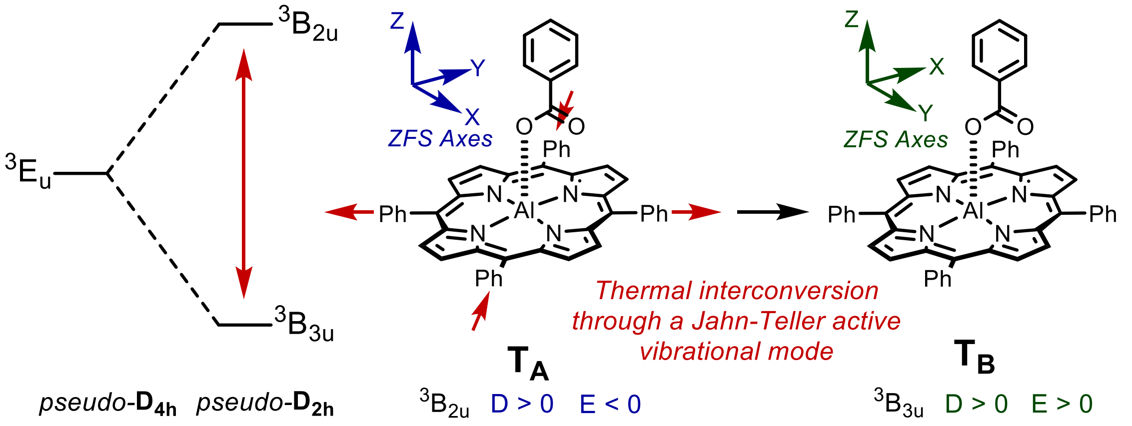

Figure 4.5 Dynamic Jahn-Teller model proposed by Panariti *et al.*[43,44] The point groups are labelled as *pseudo-* due to the presence of an axial ligand which reduces the porphyrin symmetry. A Jahn-Teller active vibration distorts the molecular symmetry to interconvert the triplet states, swapping the ZFS X and Y-axes and changing the sign of *E*. The symmetry of the reported vibrational mode is shown with red arrows.

Guided by this model, the simulated porphyrin triplets are assigned *E* values of opposite sign (Table 4.1). The positive sign of *D* is assigned by assuming an oblate spin distribution, as is standard for porphyrin monomers.[36,44] The magnitude of *D* and spin polarisation are similar for the two triplets. The relative contributions of the two triplets to the total spectrum change through time (increasing triplet A and decreasing triplet B), which is consistent with the proposed vibrational interconversion from triplet A to triplet B, albeit not direct evidence for such a mechanism.

Table 4.1 Zero-field splitting parameters, relative sublevel populations and relative weights for the triplet components of the simulated **AlPorPh** trESR spectrum.

Component	*D* / MHz	*E* / *D*	$P_x : P_y : P_z$	Relative Component Weight 0-0.1 µs	Relative Component Weight 0.2-0.3 µs	Relative Component Weight 0.4-0.5 µs
Triplet A	+876	-0.11	0.51 : 0.49 : 0	0.53	0.28	0.17
Triplet B	+927	+0.29	0.63 : 0.37: 0	0.47	0.72	0.83

4.2.2 **AlPorF$_{20}$Ph**

The trESR results and numerical simulations for **AlPorF$_{20}$Ph** are summarised in Figure 4.6 and Table 4.2. The trESR spectrum of **AlPorF$_{20}$Ph** is broader than that of **AlPorPh**, and the polarisation pattern is A/E instead of E/A (Figure 4.5). The symmetry of **AlPorF$_{20}$Ph** is also pseudo-D_{4h} and consequently, the spectrum features a high number

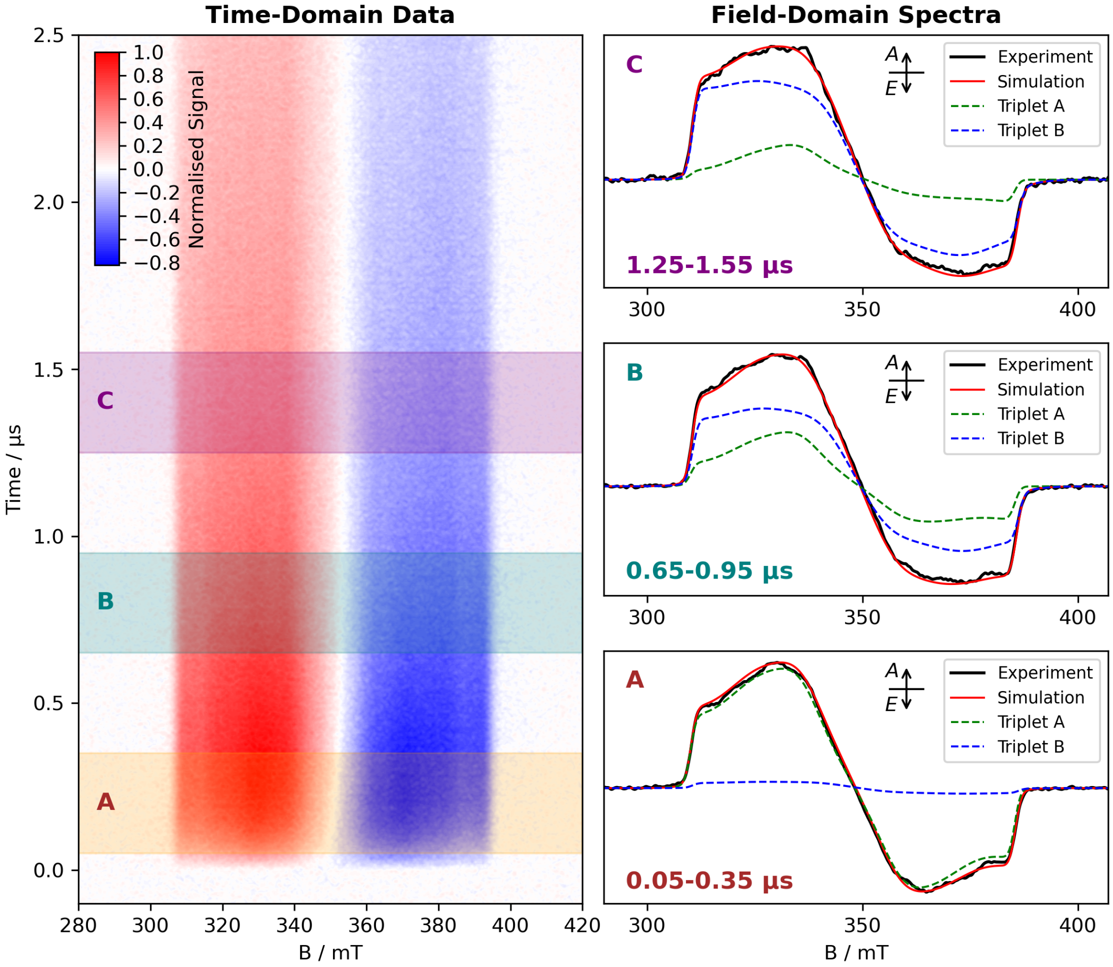

Figure 4.6 Left: trESR spectrum (2-MeTHF, X-band, 80 K, 532 nm, 10 mJ, 50 Hz) of **AlPorF$_{20}$Ph**, as a function of field and time after the laser pulse. Horizontal bands highlight the integration windows for the spectra on the right. Right: Field-domain spectra averaged over three different time windows after the laser pulse. The experimental signals are shown in black and the simulated signals in red. The contributions of each triplet to the overall simulated spectra are shown with dashed lines.

of turning points that were best simulated with two interconverting triplets as before. The simulated triplets feature a higher ZFS parameter *D* than those of **AlPorPh**, which accounts for the broader spectrum (Table 4.2). Additionally, the inversion of polarisation pattern from E/A to A/E is accounted for by a change in ZFS sublevel population: from majority T_X/T_Y in **AlPorPh** to majority T_Z population in **AlPorF$_{20}$Ph**. A quantitative comparison of the triplet kinetics between **AlPorPh** and **AlPorF$_{20}$Ph** is precluded by the fact that the two trESR spectra were acquired with different resonators, and hence have different time-domain distortions due to the instrument response factor (Q-factor).

Table 4.2 Zero-field splitting parameters, relative sublevel populations and relative weights for the triplet components of the simulated **AlPorF$_{20}$Ph** trESR spectrum.

Component	D / MHz	E / D	$P_X : P_Y : P_Z$	Relative Component Weight		
				0.05-0.35 μs	0.65-0.95 μs	1.25-1.55 μs
Triplet A	+1049	+0.12	0.16 : 0 : 0.84	0.95	0.41	0.26
Triplet B	+1051	-0.20	0 : 0.06 : 0.94	0.05	0.59	0.74

While we are unable to explain the origins of the observed changes in D and P_X:P_Y:P_Z between **AlPorPh** and **AlPorF$_{20}$Ph**, a similar observation has been reported in magnesium porphyrins.[45] A possible explanation is that the pentafluorophenyl *meso*- side chains affect the vibrational modes of the porphyrin. This could influence the vibronic contribution to the ISC mechanism, impacting the spin polarisation.[38] Additionally, such a change could impact the average electron-electron distance, affecting D accordingly. Further work, outside of the scope of this thesis, is presently being carried out in the Timmel group to test this hypothesis, guided by DFT calculations.

4.3 Triplet States in Aluminium Porphyrin Dyads

To elucidate the impact of the electron acceptors and donors on the porphyrin triplet features, X-band (9.75 GHz) trESR spectra were measured for the chromophore-acceptor and donor-chromophore dyads (at 80 K, degassed and flame sealed in o-DCB).

4.3.1 **AlPorF$_{20}$C$_{60}$** *(Chromophore-Acceptor Dyad)*

The trESR results and numerical simulations for **AlPorF$_{20}$C$_{60}$** are summarised in Figure 4.7 and Table 4.3. The trESR spectra of **AlPorF$_{20}$C$_{60}$** were measured with different excitation wavelengths to investigate energy transfer pathways. The trESR spectra (averaged between 0.25-0.35 μs) show two features with A/E polarisation patterns, neither of which match the characteristics of a SCRP (a pair of narrow E/A doublets). Based on the previous measurement of **AlPorF$_{20}$Ph** (Figure 4.6), the broad weak signal is assigned to a porphyrin triplet. By comparison with the literature, the sharper central signal can be assigned to a fullerene triplet.[46] As the photoexcitation wavelength is varied, the relative intensities of each triplet vary in accordance with the contribution of each species to the absorption spectrum (Figure 4.7). This indicates that the porphyrin and fullerene triplets are not formed through triplet-triplet energy transfer (the relative intensities would be independent of wavelength). Instead, the triplets are likely being formed through ISC. To further support this, the exclusive T_Z population of the porphyrin triplet (Table 4.3) matches the ISC-generated triplet spin polarisation in **AlPorF$_{20}$Ph**.

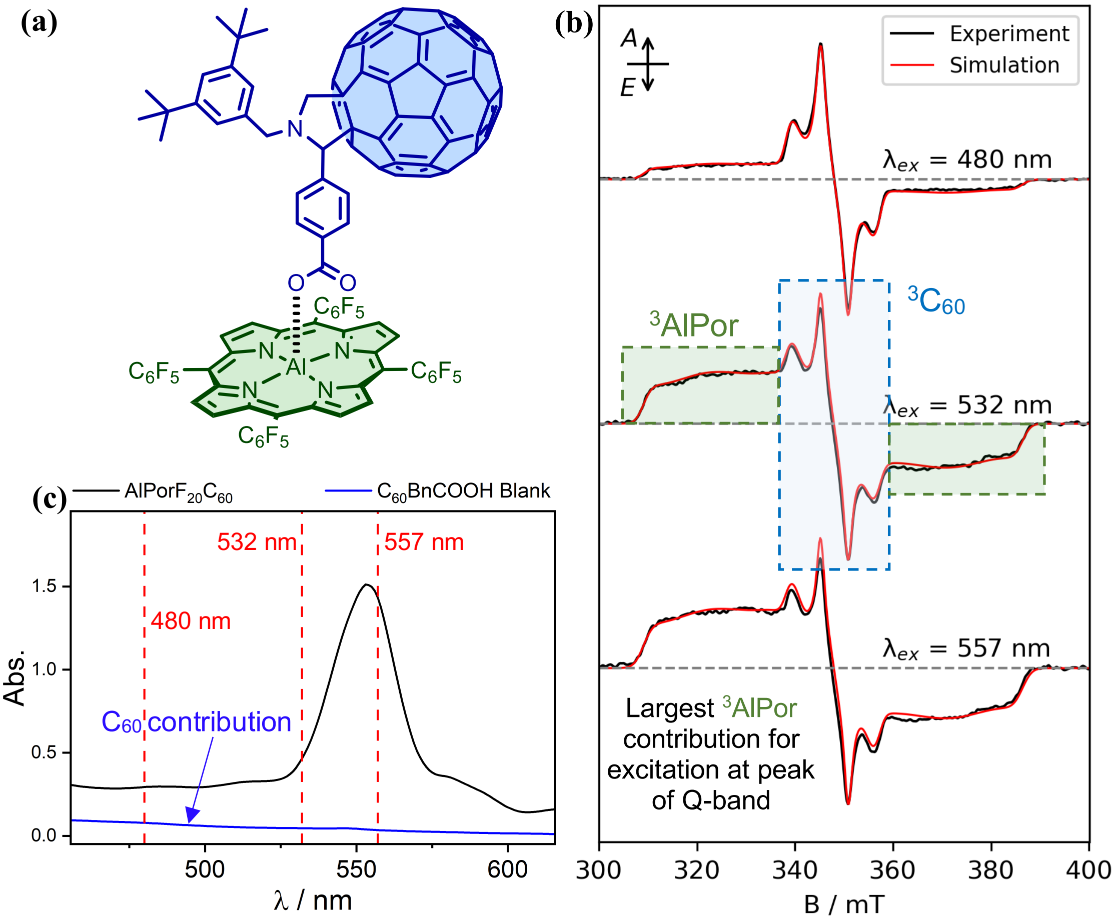

Figure 4.7 (a) **AlPorF$_{20}$C$_{60}$** structure. (b) Stacked trESR spectra (o-DCB, X-band, 1 mJ, 20 Hz) of **AlPorF$_{20}$C$_{60}$** at 80 K with different excitation wavelengths, averaged from 0.25-0.35 µs after the laser pulse. The experimental signals are shown in black and the simulated signals in red. (c) UV-Vis spectrum of **AlPorF$_{20}$C$_{60}$** (o-DCB, 293 K) at the same concentration as the ESR sample (c.a. 100 µM). The vertical red lines indicate the different excitation wavelengths. The spectrum of **C$_{60}$BnCOOH** at the same [C$_{60}$], overlayed in blue, shows the relative contribution of fullerene absorption to the triad spectrum.

Table 4.3 Zero-field splitting parameters and relative sublevel populations for the triplet components of the **AlPorF$_{20}$C$_{60}$** trESR spectrum. The relative triplet weights are given for each excitation wavelength.

Component	D / MHz	E / D	$P_X : P_Y : P_Z$	Relative Component Weight 480 nm	 532 nm	 557 nm
Porphyrin Triplet	+1080	-0.19	0 : 0 : 1	0.22	0.51	0.55
Fullerene Triplet	+266	+0.13	0 : 0.42 : 0.58	0.78	0.49	0.45

4.3.2 **TAAIm-AlPorF$_{20}$Ph** *(Donor-Chromophore Dyad)*

The trESR results and numerical simulations for **TAAIm-AlPorF$_{20}$Ph** are summarised in Figure 4.8 and Table 4.4. The trESR spectrum of **TAAIm-AlPorF$_{20}$Ph** displays a signal that is assigned to a porphyrin triplet, based on the similarity in spectral width to the reference **AlPorF$_{20}$Ph** and its A/E polarisation pattern. However, crucially, the spectral shape for **TAAIm-AlPorF$_{20}$Ph** is different to **AlPorF$_{20}$Ph**. This is reflected by the introduction of T_Y population and a higher D value in the simulated triplet. The change in spin polarisation suggests that coordination of **TAAIm** influences the mechanism of triplet formation.

To explore whether this effect was a result of the change in coordination geometry from 5-coordinate to 6-coordinate, the reference compound **MeIm-AlPorF$_{20}$Ph** was also measured. The trESR results and numerical simulations are also shown in Figure 4.8 and Table 4.4. The shape of the porphyrin triplet signal of **MeIm-AlPorF$_{20}$Ph** is similar to **AlPorF$_{20}$Ph**, which is reflected in the absence of T_Y population. The difference between the spectra of **TAAIm-AlPorF$_{20}$Ph** and **MeIm-AlPorF$_{20}$Ph** confirms that it is the presence of the **TAAIm** electron donor that influences the porphyrin triplet spin polarisation, and not simply the presence of a dative ligand.

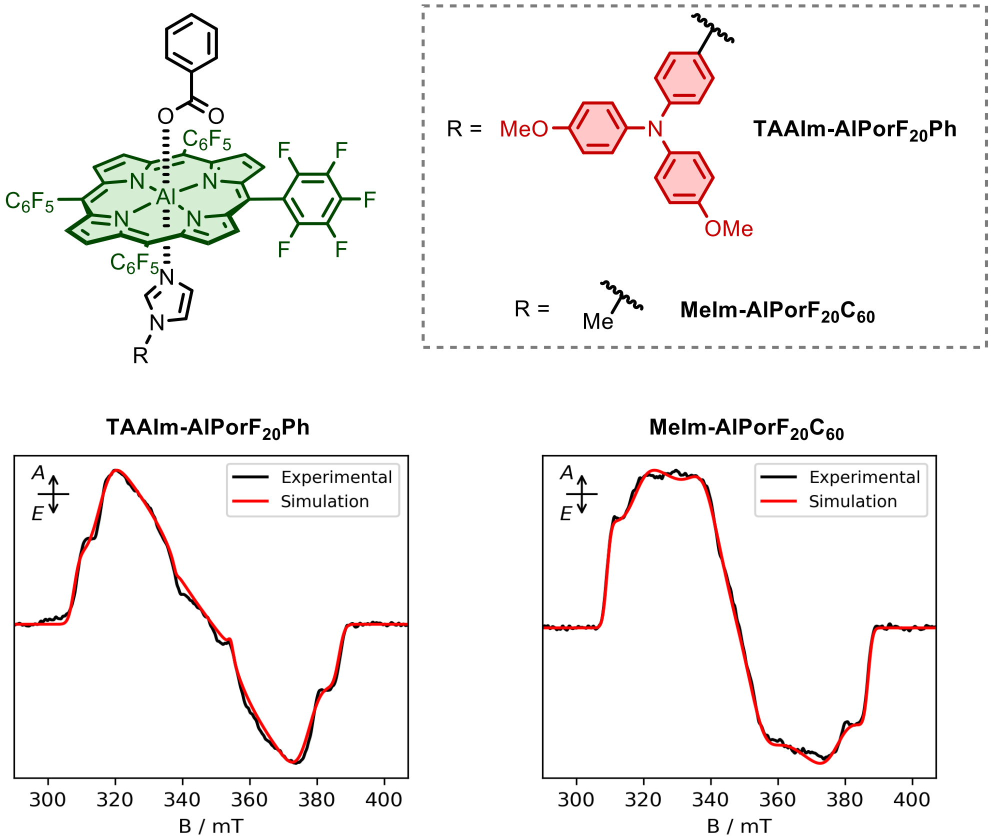

Figure 4.8 Top: structures of **TAAIm-AlPorF$_{20}$Ph** and **MeIm-AlPorF$_{20}$Ph**. Bottom: trESR spectra (o-DCB, X-band, 80 K, 557 nm, 1 mJ, 20 Hz), averaged from 0.25-0.35 µs after laser pulse for **TAAIm-AlPorF$_{20}$Ph** (left) and **MeIm-AlPorF$_{20}$Ph** (right). The experimental signals are shown in black and the simulated signals in red.

Table 4.4 Zero-field splitting parameters and relative sublevel populations for the porphyrin triplets in **TAAIm-AlPorF$_{20}$Ph** and **MeIm-AlPorF$_{20}$Ph**.

Compound	*D* / MHz	*E* / *D*	$P_X : P_Y : P_Z$
TAAIm-AlPorF$_{20}$Ph	+1104	-0.19	0 : 0.38 : 0.62
MeIm-AlPorF$_{20}$Ph	+1086	-0.18	0 : 0 : 1

4.4 Triplet States in an Aluminium Porphyrin Triad

Finally, the donor-chromophore-acceptor interactions in the triad, **TAAIm-AlPorF$_{20}$C$_{60}$**, were probed by investigating its photogenerated triplet states with X-band (9.75 GHz) trESR. As with the **AlPorF$_{20}$C$_{60}$** dyad, the trESR spectra were recorded with different excitation wavelengths to investigate the possibility of energy transfer. The spectra were measured at 80 K in o-DCB (degassed and flame-sealed). The trESR results and numerical simulations are summarised in Figure 4.9 and Table 4.5.

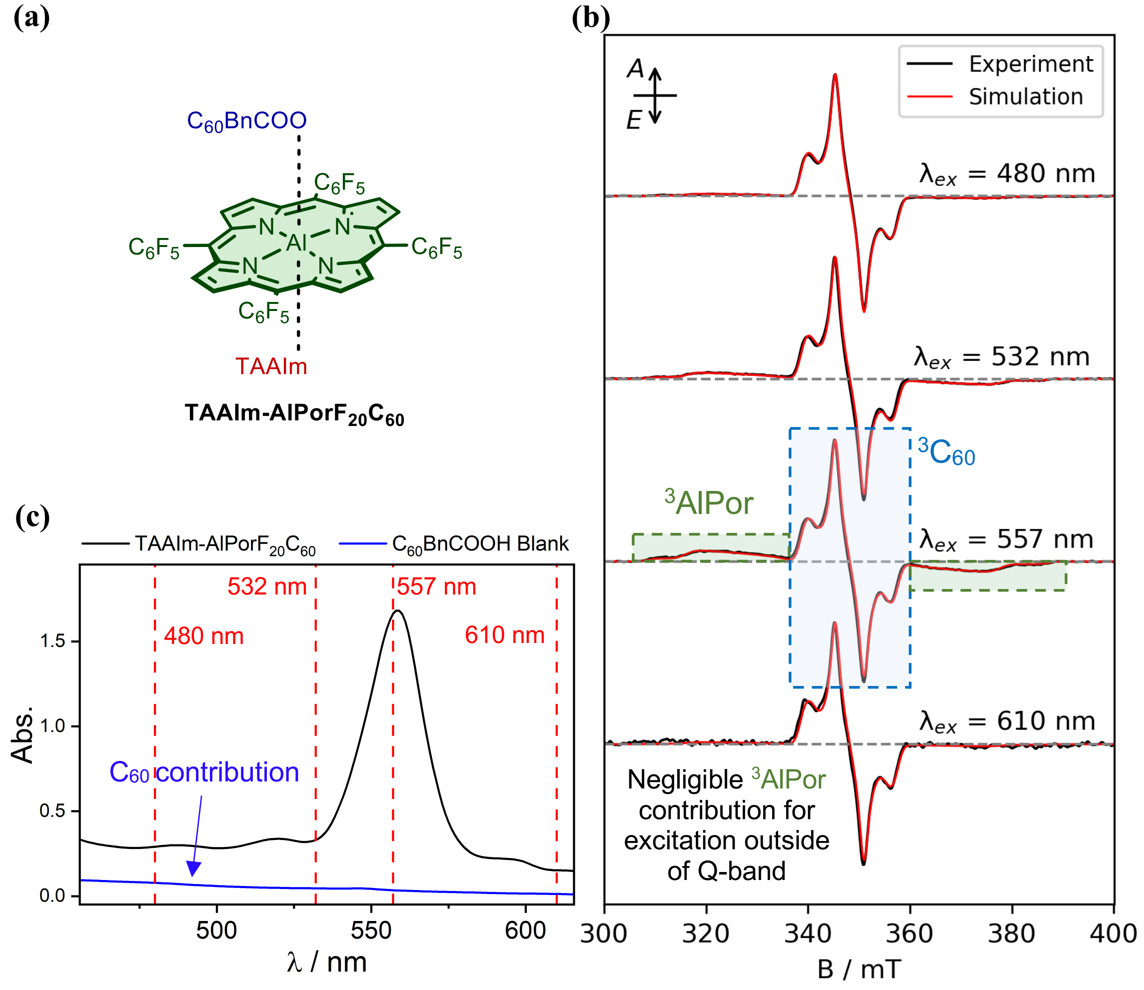

Figure 4.9 (a) Structure of the triad **TAAIm-AlPorF$_{20}$C$_{60}$**. (b) Stacked trESR spectra (o-DCB, X-band, 1 mJ, 20 Hz) of **TAAIm-AlPorF$_{20}$C$_{60}$** at 80 K with different excitation wavelengths, averaged from 0.25-0.35 µs after the laser pulse. The experimental signals are shown in black and the simulated signals in red. (c) UV-Vis spectrum of **TAAIm-AlPorF$_{20}$C$_{60}$** (o-DCB, 293 K) at the same concentration as the ESR sample (c.a. 100 µM). The vertical red lines indicate the different excitation wavelengths. The spectrum of **C$_{60}$BnCOOH** at the same [C$_{60}$], overlayed in blue, shows the relative contribution of fullerene absorption to the triad spectrum.

Table 4.5 Zero-field splitting parameters and relative sublevel populations for the triplet components of the simulated **TAAIm-AlPorF$_{20}$C$_{60}$** trESR spectrum. The relative triplet weights are given for each excitation wavelength.

Component	*D* / MHz	*E* / *D*	P$_X$: P$_Y$: P$_Z$	Relative Component Weight			
				480 nm	532 nm	557 nm	610 nm
Porphyrin Triplet	+1100	-0.19	0 : 0.50 : 0.50	0.07	0.18	0.28	0.07
Fullerene Triplet	+265	+0.13	0 : 0.39 : 0.61	0.93	0.82	0.72	0.93

There is no evidence of a SCRP (a pair of E/A doublets) in the trESR spectra of the triad, which is consistent with the rapid (< 1 ns) radical recombination observed by TA (Chapter 3). The TA measurements were performed at 293 K, whilst the trESR measurements were at 80 K, so lowering the temperature does not sufficiently decelerate the recombination for a SCRP to be detected with the ~10 ns time resolution of trESR.

Similarly to **AlPorF$_{20}$C$_{60}$**, the triad trESR spectra contain a sharp A/E signal that is assigned to a fullerene triplet, and a broader A/E signal that is assigned to a porphyrin triplet. However, the triad spectra show several differences to the **AlPorF$_{20}$C$_{60}$** spectra, which indicate that **TAAIm** influences the photochemistry. Firstly, the intensity of the porphyrin triplet relative to the fullerene triplet is much weaker in **TAAIm-APorF$_{20}$C$_{60}$**. Additionally, the triad porphyrin triplet is slightly broader and its spin polarisation pattern is different – the same effect which was observed in Figure 4.8 for **TAAIm-AlPorF$_{20}$Ph** vs. **MeIm-AlPorF$_{20}$C$_{60}$**. The changes in the porphyrin signal are accounted for by the introduction of T_Y population and a higher D value in the triad porphyrin triplet, which suggest that the donor **TAAIm** influences the mechanism of triplet formation.

4.5 Summary and Discussion

Unfortunately, no SCRP signal was observed in the trESR spectra of the triad at 80 K, which is attributed to rapid recombination of the radical pair on the timescale of the experiment. This is consistent with the TA measurements (Chapter 3), and suggests the need for further tuning of the triad structure to produce a viable molecular compass. To guide this, a comparison of the porphyrin triplet parameters by trESR reveals information about the effectiveness of the electron donor and acceptor. Figure 4.10 and Table 4.6 provide a summary of the key results from this chapter.

Table 4.6 Summary of the key parameters for the simulated porphyrin triplets of compounds in this chapter.

Compound	D / MHz	E / D	$P_X : P_Y : P_Z$	Coordination No.
AlPorF$_{20}$Ph (Triplet B)	+1051	-0.20	0 : 0.06 : 0.94	5
AlPorF$_{20}$C$_{60}$	+1080	-0.19	0 : 0 : 1	5
MeIm-AlPorF$_{20}$Ph	+1086	-0.19	0 : 0 : 1	6
TAAIm-AlPorF$_{20}$Ph	+1104	-0.19	0 : 0.38 : 0.62	6
TAAIm-AlPorF$_{20}$C$_{60}$	+1100	-0.19	0 : 0.50 : 0.50	6

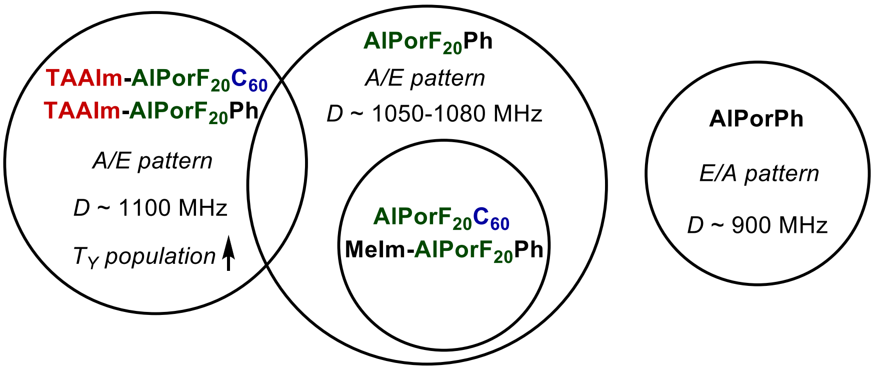

Figure 4.10 Illustration conveying the differences between the porphyrin triplets. The degree of overlap between the circles represents the similarity between the porphyrin triplets parameters.

An important observation is that the donor, **TAAIm**, influences the mechanism of porphyrin triplet formation (because the triplet sublevel populations change). This is consistent with the findings of Chapter 3: binding of **TAAIm** quenches fluorescence through PET. The failure of the **C$_{60}$COOH** acceptor to influence the porphyrin triplet polarisation is consistent with the hypothesis proposed in Chapter 3, suggesting that the reason for the short radical pair lifetime is the failure of fullerene acceptor to produce PET. Additionally, the photogenerated fullerene triplet appears to be formed through intersystem crossing – not through energy transfer interactions with the porphyrin.

To generate a long-lived SCRP for magnetic sensing, the rate of electron transfer from porphyrin to acceptor must be increased. This could be achieved by lowering the oxidation potential of the porphyrin (by tweaking the *meso*- side chains), or by choosing a different acceptor with a higher reduction potential. These conclusions inform the design of future porphyrin-based molecular compasses, and demonstrate the value of synthetic modularity for optimising the sensing ability of such systems.

5 Conclusions

The biomimetic sensing of magnetic fields offers a promising route towards the development of highly accurate, sensitive, and tunable molecular compasses. Aluminium porphyrin triads provide an attractive framework for such molecules, due to the modularity provided by their axial bonding. In this thesis, the photochemical characterisation of a molecular compass candidate was achieved through the synthesis and spectroscopic investigation of a series of aluminium porphyrin complexes. This work demonstrates the importance of modularity in the optimisation of triad structure for magnetic field effects. Future work in this area should focus on structural changes to the porphyrin or electron acceptor to drive porphyrin-acceptor electron transfer.

Chapter 2 presented the synthesis of an aluminium porphyrin triad, **TAAIm-AlPorF$_{20}$C$_{60}$**, alongside several reference complexes.

Chapter 3 described a spectroscopic study of photoinduced electron transfer in **TAAIm-AlPorF$_{20}$C$_{60}$**. The results of fluorescence and TA spectroscopy confirmed that a radical pair is formed in the triad through photoinduced electron transfer. However, the radical pair is too short-lived to display magnetic field effects.

Chapter 4 presented a transient ESR investigation into photogenerated triplet states in **TAAIm-AlPorF$_{20}$C$_{60}$** and other aluminium porphyrin complexes. New evidence for the dynamic Jahn-Teller behaviour of D_{4h} metalloporphyrins was discovered. Comparing the spectral signatures of various aluminium porphyrin triplet states provided insight into the short-lived radical pair lifetime, guiding the future design of aluminium porphyrin complexes for magnetic sensing.

6 Experimental Procedures

6.1 General Methods

Commercially available reagents and solvents were used without further purification unless otherwise specified. Anhydrous solvents were obtained from a MBraun MBSPS-5-BenchTop solvent purification system. Reactions involving air-sensitive materials were performed under argon using standard Schlenk line techniques. Thin-layer chromatography (TLC) was performed on Merck TLC silica gel 60 F_{254}. UV light was used for visualisation when necessary. Column chromatography was performed on Merck silica gel 60 (230-400 mesh ASTM) under a positive pressure of nitrogen.

Chloroform-d for NMR was stored over K_2CO_3. NMR spectra were recorded on a Bruker Avance III HD equipped with either a 9.4 T magnet or a 11.7 T magnet. Chemical shift values are referenced against residual solvent peaks. MALDI-TOF mass spectra were obtained on an Autoflex MALDI-TOF/TOF instrument, using *trans*-2-[3-(4-*tert*-butylphenyl)-2-methyl-2-propenylidene] malononitrile (DCTB) as a matrix. ESI-MS spectra were obtained on a Waters ACQUITY RDa mass spectrometer equipped with an ESI probe. FT-IR spectra were acquired on a Bruker 27 FT-IR spectrometer.

6.2 Synthetic Procedures

Synthetic procedures for new compounds are given below and their spectra are given in the appendix.

Procedures for known compounds synthesised by literature methods are given in the appendix. Where significant modifications have been made to literature methods, the procedures for known compounds are given below.

$C_{60}COO^tBu$

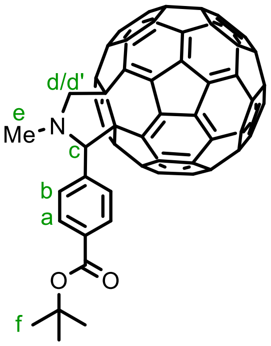

This new compound was synthesised by adapting a literature procedure.[23] C_{60} (100 mg, 140 µmol, 1.00 eq), *N*-methylglycine (25 mg, 280 µmol, 2.00 eq) and *tert*-butyl 4-formylbenzoate, **1**, (143 mg, 700 µmol, 5.00 eq) were placed under an argon atmosphere and dissolved in dry toluene (100 mL). The reaction mixture was heated to reflux for 90 minutes. The formation of the product was monitored by TLC (toluene : ethyl acetate = 99:1 *v/v*, $R_f = 0.40$). After cooling to room temperature, the solvent was removed and the crude product was purified by silica column chromatography (toluene : ethyl acetate = 99:1 *v/v*) to yield a brown solid (40 mg, 30%).

^{1}H NMR (400 MHz, $CDCl_3$) δ 8.06 (d, $J = 8.0$ Hz, 2H, H_a), 7.89 (br s, 2H, H_b), 5.02 (s + d, $J = 9.4$ Hz, 2H, $H_c + H_d$), 4.30 (d, $J = 9.4$ Hz, 1H, $H_{d'}$), 2.81 (s, 3H, H_e), 1.59 (s, 9H, H_f).

MALDI-TOF Found *m/z* 896.30 (calculated for $[C_{70}H_{10}NO_2]^+$ fragment = 896.07).

FT-IR (only selected signals) ν = 1714 cm^{-1}.

$C_{60}BnCOO^tBu$

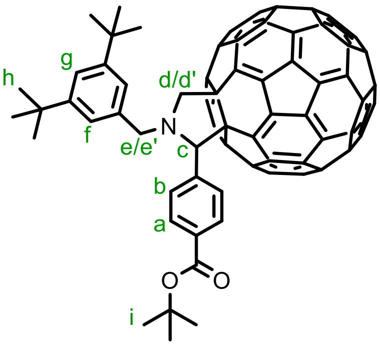

This new compound was prepared by adapting a literature procedure.[23] C_{60} (100 mg, 140 µmol, 1.00 eq), (3,5-di-*tert*-butylbenzyl)glycine, **3**, (77 mg, 280 µmol, 2.00 eq) and *tert*-butyl 4-formylbenzoate, **1**, (143 mg, 700 µmol, 5.00 eq) were placed under an argon atmosphere and dissolved in dry toluene (100 mL). The reaction mixture was heated to reflux for 90 minutes. The formation of the product was monitored by TLC (toluene : PE 40-60 = 1:1 *v/v*, $R_f = 0.50$). After cooling to room temperature, the solvent was removed and the crude product was purified by silica column chromatography (toluene : PE 40-60 = 1:1 *v/v*) to yield a brown solid (70 mg, 44%).

^{1}H NMR (400 MHz, $CDCl_3$) δ 8.07 (d, J = 8.8 Hz, 2H, H_a), 7.97 (br s, 2H, H_b), 7.47 (d, J = 1.8 Hz, 2H, H_f), 7.45 (t, J = 1.8 Hz, 1H, H_g), 5.26 (s, 1H, H_c), 4.96 (d, J = 9.5 Hz, 1H, H_d), 4.50 (d, J = 13.7 Hz, 1H, H_e), 4.22 (d, J = 9.5 Hz, 1H, $H_{d'}$), 3.81 (d, J = 13.7 Hz, 1H, $H_{e'}$), 1.59 (s, 9H, H_i), 1.41 (s, 18H, H_h).

MALDI-TOF Found *m/z* 1140.17 (calculated for $[C_{88}H_{39}NO_2]^+$ = 1141.30).

FT-IR (only selected signals) ν = 1716 cm^{-1}.

C_{60}BnCOOH

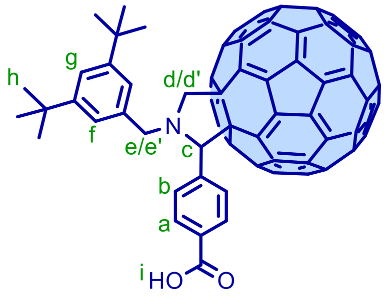

This new compound was prepared by adapting a literature procedure.[47] To a solution of **C_{60}BnCOO^{t}Bu** (70.0 mg, 61.0 μmol) in dichloromethane (15.0 mL) was added trifluoroacetic acid (5.0 mL). The reaction mixture was stirred for 24 hours under argon and the solution was then diluted with toluene (15.0 mL). The solvents were removed under a gentle stream of nitrogen and the product was washed with petroleum ether 40-60 (2 x 20 mL). After drying *in vacuo*, the product was obtained as a brown solid (64 mg, 96%).

^{1}H NMR (400 MHz, $CDCl_3$) δ 8.19 (d, J = 8.6 Hz, 2H, H_a), 8.05 (br s, 2H, H_b), 7.47 (s, 1H, H_g), 7.45 (s, 2H, H_f), 5.32 (s, 1H, H_c), 5.09 (d, J = 9.9 Hz, 1H, H_d), 4.58 (d, J = 13.7

Hz, 1H, H$_e$), 4.29 (d, J = 9.9 Hz, 1H, H$_{d'}$), 3.94 (d, J = 13.7 Hz, 1H, H$_{e'}$), 3.62 (br s, 1H, H$_i$), 1.41 (s, 18H, H$_h$).

MALDI-TOF Found m/z 1087.67 (calculated for $[C_{84}H_{31}NO_2]^+$ = 1085.23).

FT-IR (only selected signals) ν = (broad) 1687 cm^{-1}.

AlPorF$_{20}$C$_{60}$

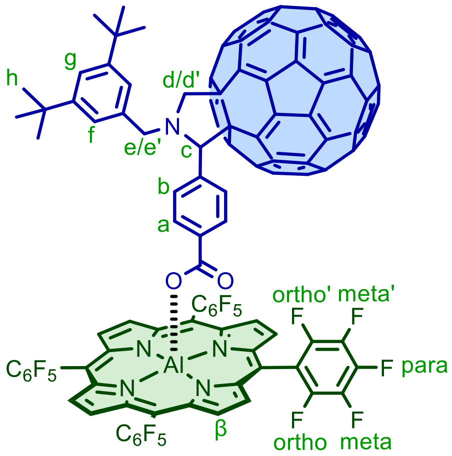

This new compound was prepared with a novel method. **AlPorF$_{20}$OH** (5.0 mg, 4.9 μmol, 1.0 eq) and **C$_{60}$BnCOOH** (8.0 mg, 7.4 μmol, 1.5 eq) were suspended in $CDCl_3$ (3.0 mL). The mixture was sonicated for 5 minutes. To the mixture was added anhydrous sodium sulfate. The reaction mixture was stirred for 30 minutes and the formation of the condensation product was monitored by UV-Vis (increasing intensity of the porphyrin absorption bands) and NMR. After solvent removal, the product was obtained as a dark purple solid that could not be separated from the excess **C$_{60}$BnCOOH.** NMR suggested quantitative conversion of **AlPorF$_{20}$OH**.

^{1}H NMR (400 MHz, $CDCl_3$) δ 9.11 (s, 8H, H$_β$), 7.31 (t, J = 1.8 Hz, 1H, H$_g$), 7.15 (d, J = 1.8 Hz, 2H, H$_f$), 6.85 (br s, 2H, H$_b$), 5.15 (br s, 2H, H$_a$), 4.68 (d + s, J = 9.5 Hz, 2H, H$_c$ + H$_d$), 3.95 (d, J = 13.6 Hz, 1H, H$_e$), 3.89 (d, J = 9.5 Hz, 1H, H$_{d'}$), 3.32 (d, J = 13.6 Hz, 1H, H$_{e'}$), 1.27 (s, 18H, H$_h$).

^{19}F NMR (376 MHz, $CDCl_3$ / CD_3OD = 9:1 *v/v*) δ -134.64 (d, J = 22.6 Hz, 1F, F$_{ortho}$), -138.71 (s, 1F, F$_{ortho'}$), -151.50 (s, 1F, F$_{para}$), -160.81 (t, J = 22.6 Hz, 1F, F$_{meta}$), -162.33 (s, 1F, F$_{meta'}$).

MALFI-TOF: Found *m/z* 2082.81 (calculated for $[C_{128}H_{38}AlF_{20}N_5O_2]^+$ = 2083.25), 999.33 (calculated for $[C_{44}H_8AlF_{20}N_4]^+$ fragment = 999.02).

UV-Vis (o-DCB, 293 K) λ_{max} / nm (ε / μM^{-1} cm^{-1}): 419 (0.45), 552 (0.02).

N-(4-(1*H*-imidazol-1-yl)phenyl)-4-methoxy-*N*-(4-methoxyphenyl)aniline, TAAIm

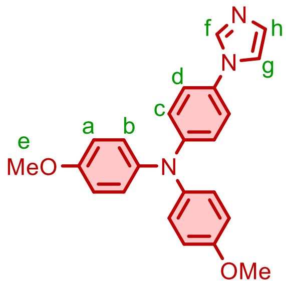

This known compound was synthesised according to a modified literature procedure.[48] **4** (100 mg, 0.26 mmol, 1.0 eq), imidazole (76 mg, 1.10 mmol, 4.3 eq), copper(I) iodide (40 mg, 0.21 mmol, 0.8 eq), 1,10-phenanthroline (38 mg, 0.21 mmol, 0.8 eq) and potassium carbonate (310 mg, 2.20 mmol, 8.6 eq) were dried under vacuum for 20 minutes and then suspended in dry dimethylformamide (1.0 mL). The reaction mixture was stirred at 150 °C for 24 hours under an argon atmosphere. After cooling to room temperature, the mixture was diluted with chloroform (50 mL) and filtered under gravity. Solvent was removed from the filtrate to give the crude product, which was purified by silica column chromatography (chloroform : ethyl acetate = 1:1 *v/v*, R_f = 0.40). A dark yellow oil was obtained (69 mg, 71%).

^{1}H NMR (400 MHz, $CDCl_3$) δ 7.77 (br s, 1H, H_f), 7.17-7.20 (br d, 2H, $H_g + H_h$), 7.15 (d, J = 9.0 Hz, 2H, H_c), 7.07 (d, J = 9.0 Hz, 4H, H_b), 6.97 (d, J = 9.0 Hz, 2H, H_d), 6.85 (d, J = 9.0 Hz, 4H, H_a), 3.80 (s, 6H, H_e).

ESI-MS: Found *m/z* 372.17 (calculated for $[C_{23}H_{22}N_3O_2]^+$ = 372.17).

UV-Vis (o-DCB, 293 K) λ_{max} / nm (ε / μM^{-1} cm^{-1}): 306 (0.02)

TAAIm-AlPorF$_{20}$C$_{60}$

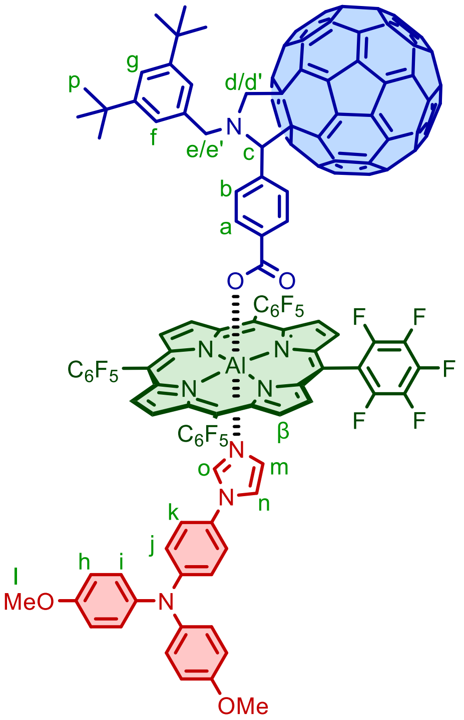

This new compound was prepared through the self-assembly of **TAAIm** and **AlPorF$_{20}$C$_{60}$** in solution. The formation of the bound complex was monitored by UV-Vis titration (see Chapter 2), yielding a binding constant of $K_a = (2.7 \pm 0.6) \times 10^6$ M^{-1} in 1,2-dichlorobenzene.

Evidence of self-assembly was observed for a range of concentrations: ~ 3-100 μM by UV-Vis and ~ 5 mM by ^{1}H NMR. Binding was observed in other non-coordinating solvents such as toluene and chloroform. No binding was observed in coordinating solvents such as methanol, 2-methyltetrahydrofuran and acetonitrile.

^{1}H NMR (400 MHz, CDCl$_3$) δ 9.04 (s, 8H, H$_\beta$), 7.30 (t, J = 1.8 Hz, 1H, H$_g$), 7.18 (d, J = 1.8 Hz, 2H, H$_f$), 6.85 (br s, 2H, H$_b$), 6.79 (d, J = 9.0 Hz, 4H, H$_i$), 6.71 (d, J = 9.0 Hz, 4H, H$_h$), 6.33 (d, J = 8.9 Hz, 2H, H$_j$), 5.46 (d, J = 8.9 Hz 2H, H$_k$), 5.12 (br s, 2H, H$_a$), 4.78 (m, 2H, H$_m$ + H$_n$), 4.67 (d + s, J = 9.5 Hz, 2H, H$_c$ + H$_d$), 3.95 (d, J = 13.6 Hz, 1H, H$_e$), 3.89 (d, J = 9.5 Hz, 1H, H$_{d'}$), 3.72 (s, 6H, H$_l$) 3.32 (d, J = 13.6 Hz, 1H, H$_{e'}$), 1.27 (s, 18H, H$_p$).

UV-Vis (o-DCB, 293 K) λ_{max} / nm (ε / μM^{-1} cm^{-1}): 423 (0.59), 556 (0.03).

The characterisation of **TAAIm-AlPorF$_{20}$C$_{60}$** by fluorescence, trESR and TA is given elsewhere in this thesis.

6.3 UV-Vis and Fluorescence Spectroscopy

UV-Vis steady-state absorption spectra were measured on a Perkin Elmer Lambda 20 spectrophotometer. The temperature of the cuvette holder was controlled using a PTP-1 Peltier unit. The measurements were carried out in a 1 cm path length quartz cuvette. For UV-Vis titrations, the raw data were processed to account for dilution of the porphyrin host. The titrations were analysed by fitting to a 1:1 binding isotherm in Origin.

Fluorescence spectra were acquired using an Edinburgh Instruments FS5 spectrofluorometer equipped with a thermostatic sample holder (SC-20). Absolute quantum yields were measured using an integrating sphere (SC-30). Fluorescence lifetimes were measured in the time-correlated single photon counting (TCSPC) mode using a picosecond pulsed diode laser (EPL-475, λ=473.4 nm) for excitation. The TCSPC data were analysed by reconvolution with the instrument response function using Fluoracle.

6.4 Electron Spin Resonance Spectroscopy

Sample solutions were prepared to a concentration of ca. 100 μM in either 2-methyl-tetrahydrofuran, toluene, or 1,2-dichlorobenzene. The solutions were inserted inside 4 mm o.d. quartz tubes which were sealed under vacuum following several freeze-pump-thaw cycles. For measurements in 1,2-dichlorobenzene at 293 K, the solutions were inserted inside 1.6 mm o.d. quartz tubes which were sealed under vacuum following several freeze-pump-thaw cycles and then placed inside a 4 mm o.d. quartz tube.

trESR spectra were recorded at X-band using a Bruker Elexsys E580/E680 spectrometer equipped with a MD4/MD5 resonator. Photoexcitation was performed using an Opotek Opolette OPO pumped by an Nd:YAG operating at 20 Hz, or at 50 Hz using an EKSPLA pumped by an Nd:YAG. Unless otherwise specified, the excitation energy was ca. 1 mJ with a repetition rate of 20 Hz. All data analysis and simulations were performed using the EasySpin package in MATLAB.[37] The trESR spectra were corrected to a common microwave frequency of 9.75 GHz. The data was baseline corrected in both time and field domains to remove baseline drift.

Bibliography

1. Mouritsen, H. "Magnetoreception in birds and its use for long-distance migration." In *Sturkie's Avian Physiology (Sixth Edition)*, 7th ed, Academic Press, San Diego, 2022, pp 233–256.
2. Wiltschko, W.; Wiltschko, R., *Science*, 1972, **176**, 62–64.
3. Schulten, K.; Swenberg, C. E.; Weller, A., *Z. Phys. Chem*, 1978, **111**, 1–5.
4. Fay, T. P.; Lindoy, L. P.; Manolopoulos, D. E.; Hore, P. J., *Faraday Discuss.*, 2020, **221**, 77–91.
5. Timmel, C. R.; Till, U.; Brocklehurst, B.; Mclauchlan, K. A.; Hore, P. J., *Mol. Phys.*, 1998, **95**, 71–89.
6. Steiner, U. E.; Ulrich, T., *Chem. Rev.*, 1989, **89**, 51–147.
7. Lewis, A. M.; Fay, T. P.; Manolopoulos, D. E.; Kerpal, C.; Richert, S.; Timmel, C. R., *J. Chem. Phys.*, 2018, **149**, 034103.
8. Hore, P. J.; Mouritsen, H., *Annu. Rev. Biophys.*, 2016, **45**, 299–344.
9. Kerpal, C.; Richert, S.; Storey, J. G.; Pillai, S.; Liddell, P. A.; Gust, D.; Mackenzie, S. R.; Hore, P. J.; Timmel, C. R., *Nat. Commun.*, 2019, **10**, 3707.
10. Maeda, K.; Henbest, K. B.; Cintolesi, F.; Kuprov, I.; Rodgers, C. T.; Liddell, P. A.; Gust, D.; Timmel, C. R.; Hore, P. J., *Nature*, 2008, **453**, 387–390.
11. Mani, T., *Chem. Phys. Rev.*, 2022, **3,** 021301.
12. Lin, N.; Tsuji, M.; Bruzzese, I.; Chen, A.; Vrionides, M.; Jian, N.; Kittur, F.; Fay, T. P.; Mani, T., *J. Am. Chem. Soc.*, 2025, **147**, 11062–11071.
13. Kodis, G.; Liddell, P. A.; Moore, A. L.; Moore, T. A.; Gust, D., *J. Phys. Org. Chem.*, 2004, **17**, 724–734.
14. Riese, S.; Brand, J. S.; Mims, D.; Holzapfel, M.; Lukzen, N. N.; Steiner, U. E.; Lambert, C., *J. Chem. Phys.*, 2020, **153**, 054306.
15. Gouterman, M., *J. Mol. Spectrosc.*, 1961, **6**, 138–163.
16. Giribabu, L.; Rao, T. A.; Maiya, B. G., *Inorg. Chem.*, 1999, **38**, 4971–4980.
17. Shetti, V. S.; Pareek, Y.; Ravikanth, M., *Coord. Chem. Rev.*, 2012, **256**, 2816–2842.
18. Zarrabi, N.; Poddutoori, P. K., *Coord. Chem. Rev.*, 2021, **429**, 213561.
19. Davidson, G. J.; Tong, L. H.; Raithby, P. R.; Sanders, J. K., *Chem. Commun.*, 2006, No. 29, 3087–3089.
20. Bagaki, A.; Gobeze, H. B.; Charalambidis, G.; Charisiadis, A.; Stangel, C.; Nikolaou, V.; Stergiou, A.; Tagmatarchis, N.; D'Souza, F.; Coutsolelos, A. G., *Inorg. Chem.*, 2017, **56**, 10268–10280.
21. Davidson, G. J. E.; Lane, L. A.; Raithby, P. R.; Warren, J. E.; Robinson, C. V.; Sanders, J. K. M., *Inorg. Chem.*, 2008, **47**, 8721–8726.
22. Rousseaux, S. A. L.; Gong, J. Q.; Haver, R.; Odell, B.; Claridge, T. D. W.; Herz, L. M.; Anderson, H. L., *J. Am. Chem. Soc.*, 2015, **137**, 12713–12718.
23. Poddutoori, P. K.; Sandanayaka, A. S. D.; Hasobe, T.; Ito, O.; van der Est, A., *J. Phys. Chem. B.*, 2010, **114**, 14348–14357.

24. Poddutoori, P. K.; Zarrabi, N.; Moiseev, A. G.; Gumbau-Brisa, R.; Vassiliev, S.; van der Est, A., *Chem. Eur. J.*, 2013, **19**, 3148–3161.
25. Poddutoori, P. K.; Lim, G. N.; Sandanayaka, A. S.; Karr, P. A.; Ito, O.; D'Souza, F.; Pilkington, M.; van der Est, A., *Nanoscale*, 2015, **7**, 12151–12165.
26. Zarrabi, N.; Seetharaman, S.; Chaudhuri, S.; Holzer, N.; Batista, V. S.; van der Est, A.; D'Souza, F.; Poddutoori, P. K., *J. Am. Chem. Soc.*, 2020, **142**, 10008–10024.
27. Zarrabi, N.; Holzer, N.; Lim, G. N.; Obondi, C. O.; van der Est, A.; D'Souza, F.; Poddutoori, P. K., *J. Porphyr. Phthalocyanines*, 2022, **26**, 407–417.
28. Di Carlo, G.; Orbelli Biroli, A.; Pizzotti, M.; Tessore, F.; Trifiletti, V.; Ruffo, R.; Abbotto, A.; Amat, A.; De Angelis, F.; Mussini, P. R., *Chem. Eur. J.*, 2013, **19**, 10723–10740.
29. Maggini, M.; Scorrano, G.; Prato, M., *J. Am. Chem. Soc.*, 1993, **115**, 9798–9799.
30. Wu, Y.; Wang, Z.; Liang, M.; Cheng, H.; Li, M.; Liu, L.; Wang, B.; Wu, J.; Prasad Ghimire, R.; Wang, X.; Sun, Z.; Xue, S.; Qiao, Q., *ACS Appl. Mater. Interfaces*, 2018, **10**, 17883–17895.
31. Dahl Jensen, J.; Jakobsen, R. K.; Yao, Z.; Laursen, B. W., *Chem. Eur. J.*, 2023, **29**, e202301077.
32. Strachan, J.-P.; Gentemann, S.; Seth, J.; Kalsbeck, W. A.; Lindsey, J. S.; Holten, D.; Bocian, D. F., *J. Am. Chem. Soc.*, 1997, **119**, 11191–11201.
33. Grzegorzek, N.; Mao, H.; Michel, P.; Junge, M. J.; Lorenzo, E. R.; Young, R. M.; Krzyaniak, M. D.; Wasielewski, M. R.; Chernick, E. T., *J. Phys. Chem. A.*, 2020, **124**, 6168–6176.
34. Kopp, S. M.; Gotfredsen, H.; Hergenhahn, J.; Rodríguez-Rubio, A.; Deng, J.-R.; Zhu, H.; Stawski, W.; Anderson, H. L., *Chem.*, 2024, **10**, 3410–3427.
35. El-Khouly, M. E.; Ito, O.; Smith, P. M.; D'Souza, F., *J. Photochem. Photobiol. C.*, 2004, **5**, 79–104.
36. Richert, S.; Tait, C. E.; Timmel, C. R., *J. Mag. Res.*, 2017, **280**, 103–116.
37. Stoll, S.; Schweiger, A., *J. Mag. Res.*, 2006, **178**, 42–55.
38. Marian, C. M., *Wiley Interdiscip. Rev. Comput. Mol. Sci.*, 2012, **2**, 187–203.
39. Bittl, R.; Weber, S., *Biochim. Biophys. Acta. - Bioenergetics*, 2005, **1707**, 117–126.
40. van der Est, A.; Poddutoori, P. K "Time-resolved EPR in artificial photosynthesis." In *Photosynthesis: Structures, Mechanisms, and Applications*, Springer International Publishing, 2017, pp 359–387.
41. Mi, Q.; Ratner, M. A.; Wasielewski, M. R., *J. Phys. Chem. A*, 2010, **114**, 162–171.
42. Di Valentin, M.; Tait, C.; Salvadori, E.; Ceola, S.; Scheer, H.; Hiller, R. G.; Carbonera, D., *J. Phys. Chem. B*, 2011, **115**, 13371–13380.
43. Carella, A.; Ciuti, S.; Wiedemann, H. T.; Kay, C. W.; van der Est, A.; Carbonera, D.; Barbon, A.; Poddutoori, P. K.; Di Valentin, M., *J. Mag. Res.*, 2023, **353**, 107515.
44. Panariti, D.; Carella, A.; Ciuti, S.; Barbon, A.; Holzer, N.; Poddutoori, P. K.; Kandrashkin, Y. E.; van der Est, A.; Di Valentin, M., *J. Chem. Phys.*, 2025, **162**.
45. Yamauchi, S.; Matsukawa, Y.; Ohba, Y.; Iwaizumi, M., *Inorg. Chem.*, 1996, **35**, 2910–2914.
46. Terazima, M.; Hirota, N.; Shinohara, H.; Saito, Y., *Chem. Phys. Lett.*, 1992, **195**, 333–338.
47. Zhou, S.; Feng, Y.; Chen, M.; Li, Q.; Liu, B.; Cao, J.; Sun, X.; Li, H.; Hao, J., *Chem. Commun.* 2016, **52**, 12171–12174.
48. Tingare, Y. S.; Li, M.; Teng, S.; Lin, J.; Su, C.; Lin, S.; Lew, X.; Tsai, H.; Ghosh, D.; Nie, W.; Yeh, B.; Li, W., *Sol. RRL*, 2024, **8**, 2300817.
49. Armstrong, A.; Brackenridge, I.; Jackson, R. F.; Kirk, J. M., *Tetrahedron Lett.*, 1988, **29**, 2483–2486.
50. Kelber, J. B.; Panjwani, N. A.; Wu, D.; Gómez-Bombarelli, R.; Lovett, B. W.; Morton, J. J.; Anderson, H. L., *Chem. Sci.*, 2015, **6**, 6468–6481.
51. Dubey, R. K.; Kumpulainen, T.; Efimov, A.; Tkachenko, N. V.; Lemmetyinen, H., *Eur. J. Org. Chem.*, 2010, **2010**, 3428–3436.
52. Zhang, Y.; Wu, F.; Chen, L.; Zhang, F.; Ji, Y.; Shen, W.; Li, M.; Guo, Q.; Su, W.; He, R., *Sol. Energy Mater. Sol. Cells*, 2020, **212**, 110534.

Appendix I: Experimental Procedures for the Synthesis of Known Compounds

5,10,15,20-Tetrakis(3,5-di-*tert*-butylphenyl)porphyrin, H_2Por^tBu

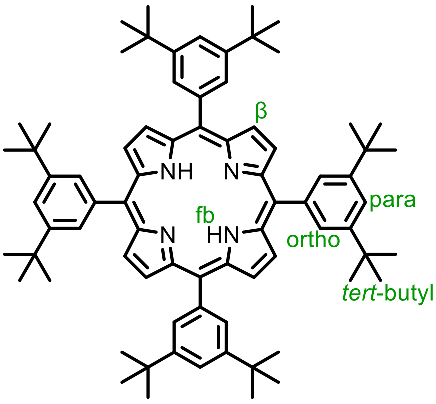

This known compound was synthesised according to a literature procedure.[28] 3,5-Di-*tert*-butylbenzaldehyde (5.00 g, 22.9 mmol, 4.00 eq) and freshly distilled pyrrole (1.59 mL, 22.9 mmol, 4.00 eq) were dissolved in dichloromethane (2.50 L). The solution was purged with nitrogen for 1 hour. Trifluoroacetic acid (1.60 mL, 21.0 mmol, 3.60 eq) was added, and the mixture was shielded from light and stirred at room temperature for 3 hours. At this point DDQ (7.80 g, 34.4 mmol, 6.00 eq) was added and the reaction stirred for 40 minutes. An excess of triethylamine (14.5 mL, 104 mmol, 18.2 eq) was added and stirring was continued overnight. After solvent removal, the remaining solid was re-suspended in methanol and the suspension was filtered. The solid residue was washed further with methanol to yield the product as a purple powder (2.51 g, 41%).

^{1}H NMR (400 MHz, $CDCl_3$) δ 8.89 (s, 8H, H_β), 8.09 (d, J = 1.8 Hz, 8H, H_{ortho}), 7.79 (t, J = 1.8 Hz, 4H, H_{para}), 1.52 (s, 72H, $H_{\textit{tert}\text{-butyl}}$), -2.67 (s, 2H, H_{fb}).

MALFI-TOF: Found *m/z* 1062.44 (calculated for $[C_{76}H_{94}N_4]^+$ = 1062.75).

UV-Vis ($CHCl_3$, 293 K) λ_{max} / nm: 420, 451, 516, 552, 591, 647.

5,10,15,20-tetrakis(perfluorophenyl)porphyrin, H_2PorF_{20}

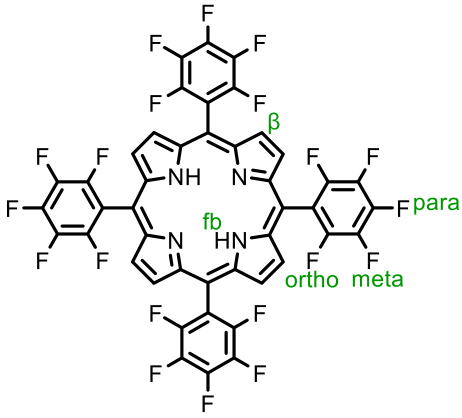

This known compound was synthesised by modifying a literature procedure.[26] 2,3,4,5,6-Pentafluorobenzaldehyde (1.27 g, 6.48 mmol, 3.85 eq) and freshly distilled pyrrole (0.452 g, 6.74 mmol, 4.00 eq) were dissolved in dichloromethane (270 mL). The solution was purged with argon for 1 hour. To the argon-saturated solution was added boron trifluoride diethyl etherate (0.10 mL, 0.81 mmol, 0.50 eq) dropwise, and the solution was shielded from light and stirred for 3 hours under argon. DDQ (1.17 g, 5.15 mmol, 3.06 eq) was added and stirring was continued overnight (18 hours). The resulting dark brown suspension was concentrated to c.a. 100 mL and passed through a short plug of silica, eluting with dichloromethane. After solvent removal, the crude solid was resuspended in methanol (200 mL). The insoluble solid was isolated by vacuum filtration and washed with several portions of methanol to obtain a purple solid (200 mg, 13%).

^{1}H NMR (400 MHz, $CDCl_3$) δ 8.91 (s, 8H, H_β), -2.91 (s, 2H, H_{fb}).

^{19}F NMR (376 MHz, $CDCl_3$) δ -136.5 (dd, ^{3}J = 22.5 Hz, ^{5}J = 7.5 Hz, 8F, F_{ortho}), -151.2 (t, J = 22.5 Hz, 4F, F_{para}), -161.3 (td, ^{3}J = 22.5 Hz, ^{5}J = 7.5 Hz, 8F, F_{meta}).

MALFI-TOF: Found *m/z* 974.06 (calculated for $[C_{44}H_{10}F_{20}N_4]^+$ = 974.06).

UV-Vis ($CHCl_3$, 293 K) λ_{max} / nm: 410, 505, 581.

AlPorOH

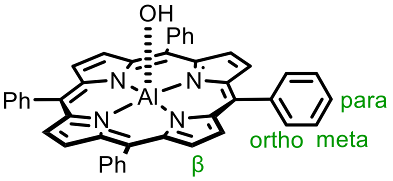

This known compound was synthesised according to a literature procedure.[19] Tetraphenylporphyrin (100 mg, 163 μmol, 1.00 eq) was dissolved in dry toluene (6.00 mL) and the solution was saturated with argon by several freeze-pump-thaw cycles. Trimethylaluminium (240 μL, 2.0 M in hexanes, 490 μmol, 3.00 eq) was added to the solution and the reaction was stirred at room temperature for 4 hours. Water (1.0 mL) was then added and stirring was continued for 30 minutes. The reaction mixture was concentrated by rotary evaporation, diluted with dichloromethane and dried over anhydrous sodium sulfate. After filtration and solvent removal, the product was washed with hexanes to give a dark green solid (80 mg, 75%).

^{1}H NMR (400 MHz, CDCl$_3$) δ 9.05 (s, 8H, H$_\beta$), 8.20 (br s, 8H, H$_{\text{ortho}}$), 7.77 (m, 12 H, H$_{\text{meta}}$ + H$_{\text{para}}$).

UV-Vis (CHCl$_3$, 293 K) λ_{max} / nm: 413, 545.

AlPor^{t}BuOH

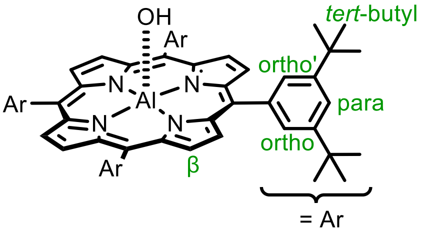

This known compound was synthesised according to the same literature procedure as above (see **AlPorOH**). The product was obtained as a dark purple solid (91 %).

^{1}H NMR (400 MHz, CDCl$_3$) δ 9.11 (s, 8H, H$_\beta$), 8.19 (s, 4H, H$_{\text{ortho}}$), 7.99 (s, 4H, H$_{\text{ortho'}}$), 7.79 (m, 4H, H$_{\text{para}}$), 1.51 (s, 72H, H$_{\textit{tert}\text{-butyl}}$).

MALFI-TOF: Found *m/z* 1104.41 (calculated $[C_{76}H_{93}AlN_4O]^+$ = 1104.72), 1087.41 (calculated for $[C_{76}H_{92}AlN_4]^+$ = 1087.71).

UV-Vis ($CHCl_3$, 293 K) λ_{max} / nm: 418, 549.

AlPorF$_{20}$OH

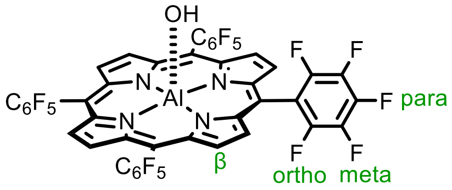

This known compound was synthesised by modifying a literature procedure.[26] **H_2PorF$_{20}$** (200 mg, 205 µmol, 1.00 eq) was dissolved in dry toluene (14.0 mL) and the solution was saturated with argon by several freeze-pump-thaw cycles. Trimethylaluminium (0.40 mL, 2.0 M in hexanes, 800 µmol, 3.9 eq) was added to the solution and the reaction was stirred at room temperature for 24 hours. Water (0.4 mL) was then added and stirring was continued for 17 hours. Solvent was removed and the crude solid was redissolved in methanol (100 mL). Insoluble aluminium salts were removed by filtration. The solvent was removed from the filtrate and the resultant solid washed with hexanes until removal of the dark green impurity. The pure product was a purple solid (136 mg, 65%).

^{1}H NMR (400 MHz, CD_3OD) δ 9.26 (s, 8H, H_β)

^{19}F NMR (376 MHz, CD_3OD) δ -139.98 (m, 8F, F_{ortho}), -155.83 (t, J = 20.7 Hz, 4F, F_{para}), -165.32 (td, ^3J = 20.7 Hz, ^5J = 7.5 Hz, 4F, F_{meta}).

MALFI-TOF: Found *m/z* 1016.41 (calculated for $[C_{44}H_9AlF_{20}N_4O]^+$ = 1016.03).

UV-Vis (CH_3OH, 293 K) λ_{max} / nm: 419, 554.

AlPorPh

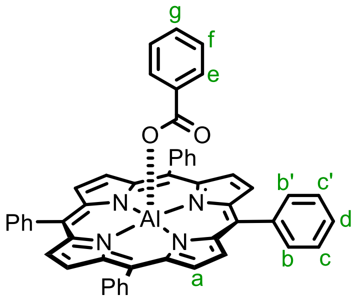

This known compound was synthesised by following a modified literature procedure.[23] **AlPorOH** (10.0 mg, 15.2 µmol, 1.00 eq) and benzoic acid (1.9 mg, 15.2 µmol, 1.00 eq) were dissolved in dry toluene (3.00 mL). The solution was stirred at 70 °C for 17 hours under an argon atmosphere. The solution was dried over sodium sulfate and the solvent was removed. Washing with hexanes (2 x 4 mL) gave the product as a dark green solid (7 mg, 60%).

^{1}H NMR (400 MHz, CDCl$_3$) δ 9.06 (s, 8H, H$_a$), 8.16 (s + s, 8H, H$_b$ + H$_{b'}$), 7.75 (m, 12 H, H$_c$ + H$_{c'}$ + H$_d$), 6.73 (t, J = 7.4 Hz, 1H, H$_g$), 6.42 (t, J = 7.4 Hz, 2H, H$_f$), 5.12 (d, J = 7.4 Hz, 2H, H$_e$).

UV-Vis (CHCl$_3$, 293 K) λ_{max} / nm: 419, 555

AlPorF$_{20}$Ph

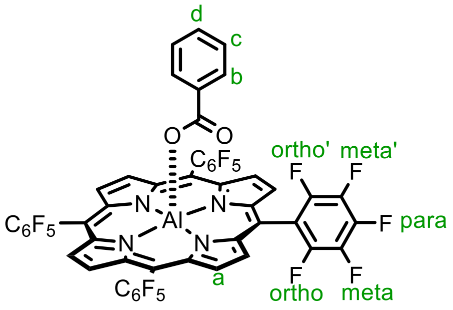

This known compound was synthesised by following a modified literature procedure.[26] **AlPorF$_{20}$OH** (5.60 mg, 5.50 µmol, 1.00 eq) and benzoic acid (0.67 mg, 5.50 µmol, 1.00 eq) were dissolved in dry dichloromethane (1.80 mL). Methanol (0.20 mL) was added to help the **AlPorF$_{20}$OH** dissolve. The solution was stirred for 1 hour under argon and then dried over sodium sulfate. Filtration and solvent removal gave the product as a purple solid (quantitative).

^{1}H NMR (400 MHz, CDCl$_3$) δ 9.15 (s, 8H, H$_a$), 6.62 (t, J = 7.7 Hz, 1H, H$_d$), 6.30 (t, J = 7.7 Hz, 2H, H$_c$), 5.05 (d, J = 7.7 Hz, 2H, H$_b$).

^{19}F NMR (376 MHz, $CDCl_3$) δ -134.96 (d, J = 22.0 Hz, 4F, F_{ortho}), -137.27 (d, J = 18.6 Hz, 4F, $F_{ortho'}$), -150.85 (t, J = 22.0 Hz, 4F, F_{para}), -160.73 (t, J = 22.0 Hz, 4F, F_{meta}), -161.43 (t, J = 18.6 Hz, 4F, $F_{meta'}$).

UV-Vis (o-DCB + 1% CH_3OH, 293 K) λ_{max} / nm: 418, 550.

***tert*-Butyl 4-formylbenzoate, 1**

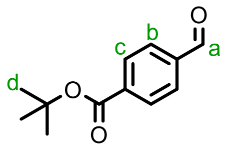

This known compound was synthesised by adapting a literature procedure.[49] 4-Formylbenzoic acid (1.00 g, 6.66 mmol, 1.00 eq) was dried under vacuum for 20 minutes, placed under an argon atmosphere and dissolved in dry tetrahydrofuran (6.00 mL). In a separate flask, *tert*-butyl 2,2,2-trichloroacetimidate (2.91 g, 13.3 mmol, 2.00 eq) was partially dissolved in cyclohexane (14.00 mL) and placed under an argon atmosphere. The second solution was slowly added to the first. Boron trifluoride diethyl etherate (250 µL, 2.00 mmol, 0.30 eq) was added dropwise and the mixture was stirred vigorously for 20 minutes at room temperature. The mixture changed from a milky suspension to a clear solution within this time. After stirring, the solution was diluted with 5% (*w/v*) aqueous sodium hydrogen carbonate solution (200 mL) and the product was extracted with ethyl acetate (2 x 100 mL). The combined organic phase was washed with water (100 mL) and brine (100 mL), and dried with anhydrous sodium sulfate. The crude product was purified by silica column chromatography (PE 40-60 : ethyl acetate = 95:5 → 8:2 *v/v*). Drying *in vacuo* yielded the product as a white solid (490 mg, 36%).

^{1}H NMR (400 MHz, $CDCl_3$) δ 10.09 (s, 1H, H_a), 8.14 (d, J = 8.4 Hz, 2H, $H_{b/c}$), 7.92 (d, J = 8.4 Hz, 2H, $H_{b/c}$), 1.61 (s, 9H, H_d).

ESI-MS: Found *m/z* 207.10 (calculated for $[C_{12}H_{15}O_3]^+$ = 207.10).

C_{60}COOH

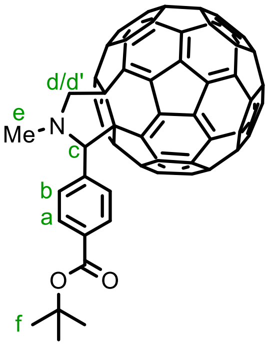

This known compound[23] was synthesised by adapting a literature procedure.[47] **C_{60}COO^{t}Bu** (20.0 mg, 21 µmol) was dissolved in dichloromethane (8.0 mL). To this solution was added trifluoroacetic acid (2.0 mL) dropwise. The reaction was stirred for 24 hours under argon and the solution was then diluted with toluene (150 mL). The solvents were removed under a gentle stream of nitrogen and the product was washed with petroleum ether 40-60 (2 x 20 mL). After drying *in vacuo*, the product was obtained as a brown solid with poor solubility (18 mg, 96%).

^{1}H NMR (400 MHz, tetrahydrofuran-d_8) δ 8.09 (d, J = 8.7 Hz, 2H, H_a), 7.97 (br s, 2H, H_b), 5.12 (s, 1H, H_c), 5.08 (d, J = 9.5 Hz, 2H, H_d), 4.34 (d, J = 9.5 Hz, 2H, $H_{d'}$), 2.81 (s, 3H, H_a), 2.74 (br s, H_f).

tert-Butyl (3,5-di-*tert*-butylbenzyl)glycinate, 2

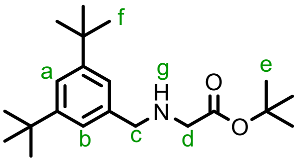

This known compound was synthesised by adapting a literature procedure.[50] *tert*-Butyl sarcosinate hydrochloride (500 mg, 2.98 mmol, 1.00 eq), 3,5-di-*tert*-butylbenzaldehyde (521 mg, 2.39 mmol, 0.80 eq) and triethylamine (420 µL, 3.00 mmol, 1.00 eq) were suspended in methanol. The suspension was heated to 35 °C and stirred vigorously to encourage the solid to dissolve. After 10 minutes, the mixture was cooled to 0 °C and sodium borohydride (226 mg, 5.97 mmol, 2.00 eq) was added in portions. The reaction was stirred at room temperature overnight. Water (25 mL) was then added to the flask and the product was extracted with ethyl acetate (2 x 50 mL). The combined organic layers were washed with water (2 x 50 mL) and brine (50 mL), and dried over anhydrous magnesium sulfate. The solvent was removed and the crude product purified by silica column chromatography (chloroform : ethyl acetate = 9:1 *v/v*). After drying *in vacuo* the product was obtained as a white solid (450 mg, 57%).

^{1}H NMR (400 MHz, $CDCl_3$) δ 7.33 (t, *J* = 2.0 Hz, 1H, H_a), 7.16 (d, *J* = 2.0 Hz, 2H, H_b), 3.78 (s, 2H, H_c), 3.34 (s, 2H, H_d), 1.90 (s, 1H, H_g), 1.48 (s, 9H, H_e), 1.33 (s, 18H, H_f).

ESI-MS: Found *m/z* 334.27 (calculated for $[C_{21}H_{36}NO_2]^+$ = 334.27).

(3,5-Di-*tert*-butylbenzyl)glycine, 3

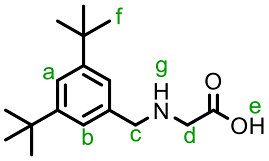

This known compound was synthesised by following a literature procedure.[51] To a solution of **2** (450 mg, 1.35 mmol) in dichloromethane (9.00 mL) was added trifluoroacetic acid (9.00 mL). The solution was stirred at room temperature for 24 hours and then the solvents were removed under a gentle stream of nitrogen. The product was redissolved in chloroform (100 mL), washed with water (100 mL) and brine (100 mL), and dried with anhydrous sodium sulfate. Drying *in vacuo* for 4 hours gave the product as a white solid (343 mg, 92%).

^{1}H NMR (400 MHz, $CDCl_3$) δ 9.29 (br s, 2H, H_e + H_g), 7.39 (t, *J* = 1.8 Hz, 1H, H_a), 7.35 (d, *J* = 1.8 Hz, 2H, H_b), 4.18 (s, 2H, H_c), 3.51 (s, 2H, H_d), 1.28 (s, 18H, H_f).

ESI-MS: Found *m/z* 278.21 (calculated for $[C_{17}H_{29}NO_2]^+$ = 278.21).

4-Bromo-*N*,*N*-bis(4-methoxyphenyl)aniline, 4

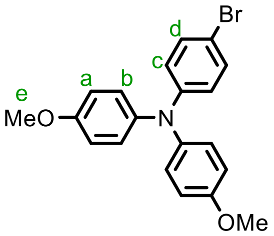

This known compound was synthesised according to a literature procedure.[30] 4-Bromoaniline (500 mg, 2.91 mmol, 1.00 eq), 4-iodoanisole (1.70 g, 7.27 mmol, 2.50 eq), copper(I) iodide (111 mg, 0.58 mmol, 0.2 eq), 1,10-phenanthroline (105 mg, 0.58 mmol, 0.2 eq) and potassium hydroxide (1.30 g, 23.3 mmol, 8.00 eq) were dried under vacuum for 20 minutes and dissolved in dry toluene (10.0 mL). The reaction mixture was heated to reflux for 24 hours under an argon atmosphere. After cooling to room temperature, the reaction mixture was diluted with dichloromethane (50 mL) and washed with water (4 x 50 mL). The organic layer was dried over anhydrous magnesium sulfate and the solvent was removed. The crude product was purified by silica column chromatography (PE 40-60 : dichloromethane = 9:1 → 1:1 *v/v*). Recrystallisation from ethanol : water = 95:5 (*v/v*) at 75 °C yielded the product as pale orange crystals (507 mg, 45%).

^{1}H NMR (400 MHz, CDCl$_3$) δ 7.73 (d, J = 8.9 Hz, 2H, H$_{a/b}$), 7.02 (d, J = 8.9 Hz, 4H, H$_{c/d}$), 6.82 (d, J = 9.0 Hz, 4H, H$_{c/d}$), 6.79 (d, J = 9.0 Hz, 2H, H$_{a/b}$), 3.79 (s, 6H, H$_e$).

ESI-MS: Found *m/z* 383.05 (calculated for $[C_{20}H_{18}BrNO_2]^+$ = 383.05).

4-Methoxy-*N*-(4-methoxyphenyl)-*N*-phenylaniline, TAA

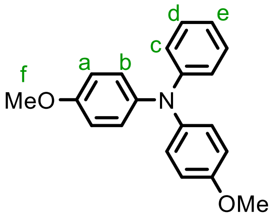

This known compound was synthesised by following a literature procedure.[52] Aniline (200 µL, 2.20 mmol, 1.00 eq), 4-iodoanisole (1.26 g, 5.37 mmol, 2.50 eq), copper(I) iodide (82.0 mg, 0.43 mmol, 0.20 eq), 1,10- phenanthroline (77.0 mg, 0.43 mmol, 0.20 eq) and potassium *tert*-butoxide (1.93 g, 17.20 mmol, 8.00 eq) were dissolved in dry toluene (12.0 mL). The flask was quickly evacuated and backfilled with argon (several cycles) and the reaction mixture was heated at reflux for 24 hours. After cooling to room temperature, the mixture was diluted with dichloromethane (20 mL) and washed with water (4 x 15 mL). The combined organic phase was dried with anhydrous magnesium sulfate and the solvent was evaporated. The crude product was purified by silica column chromatography (PE 40-60 : ethyl acetate = 98:2 → 80:20 *v/v*). Recrystallisation from methanol at 60 °C yielded the product as white crystals (283 mg, 43%).

^{1}H NMR (400 MHz, $CDCl_3$) δ 7.16 (t, J = 8.0 Hz, 2H, $H_{c/d}$), 7.04 (d, J = 9.1 Hz, 4H, $H_{a/b}$), 6.93 (d, J = 8.0 Hz, 2H, $H_{c/d}$), 6.86 (t, J = 8.0 Hz, 1H, H_e), 6.81 (d, J = 9.1 Hz, 4H, $H_{a/b}$), 3.79 (s, 6H, H_f).

ESI-MS: Found *m/z* 306.15 (calculated for $[C_{20}H_{20}NO_2]^+$ = 306.15).

Zinc tetraphenylporphyrin, ZnTPP

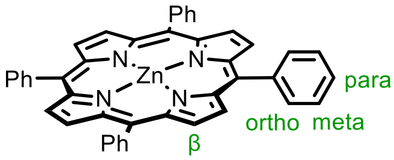

This known compound was synthesised by adapting a group procedure. To a solution of tetraphenylporphyrin (500 mg, 0.81 µmol, 1.00 eq) in chloroform (85.0 mL) was added zinc acetate dihydrate (928 mg, 4.23 mmol, 5.20 eq) in methanol (10.0 mL). The reaction was stirred for 1 hour. Solvent was removed and the crude product was redissolved in chloroform (50.0 mL). The solution was eluted through a short silica plug with chloroform. Solvent removal *in vacuo* gave the product as a purple solid (456 mg, 83%).

^{1}H NMR (400 MHz, $CDCl_3$) δ 8.95 (s, 8H, H_β), 8.23 (dd, ^{3}J = 7.6 Hz, ^{5}J = 1.7 Hz, 8H, H_{ortho}), 7.68-7.84 (m, 12H, $H_{meta} + H_{para}$).

UV-Vis (Toluene, 293 K) λ_{max} / nm: 410, 505, 581.

Appendix II: Characterisation Data of New Compounds

$C_{60}COO^tBu$

^{1}H NMR (400 MHz, $CDCl_3$)

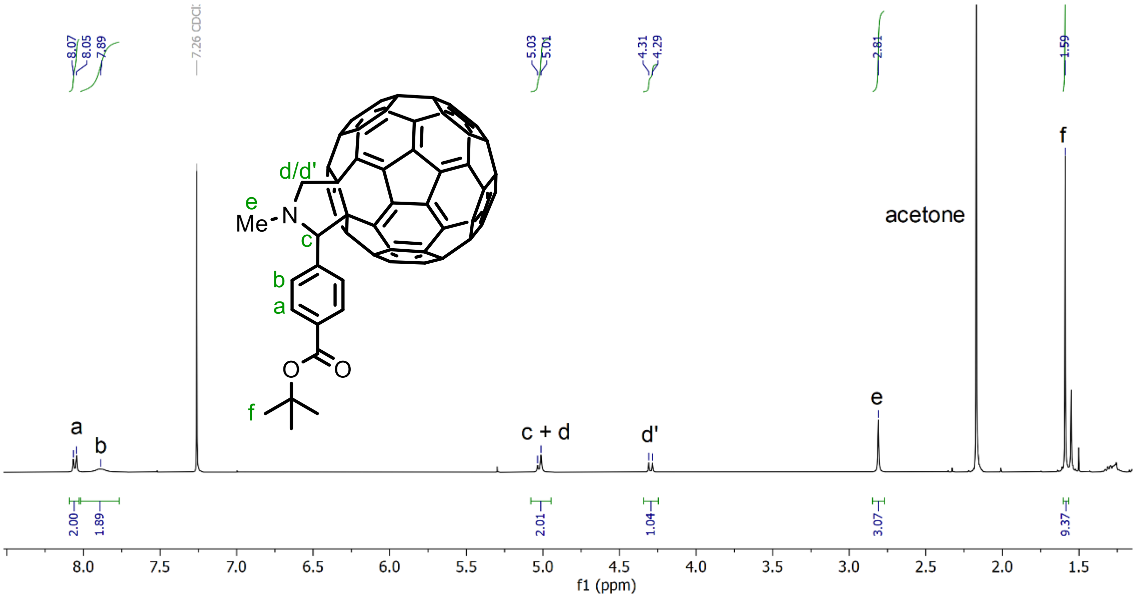

MALDI-TOF

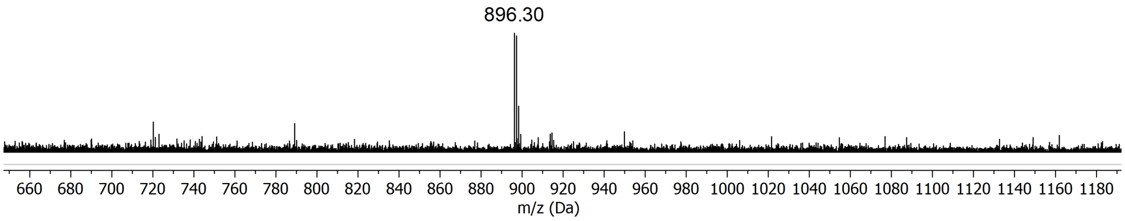

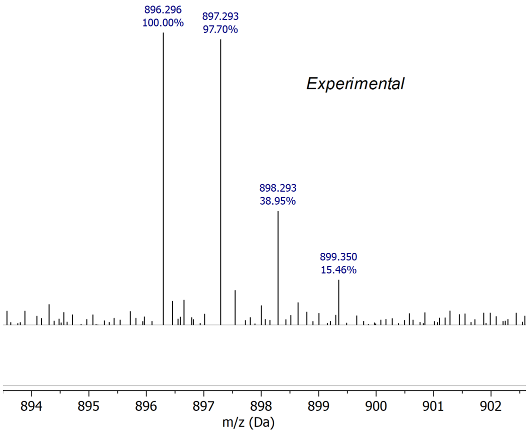

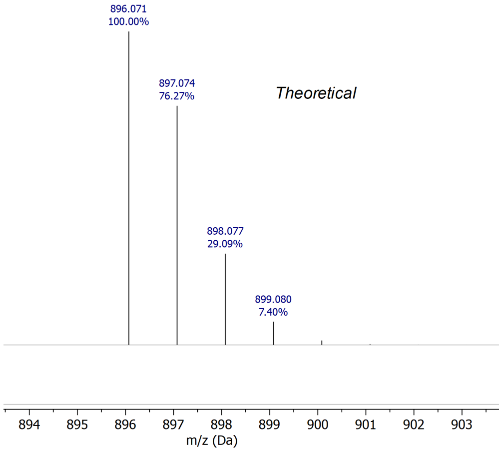

FT-IR

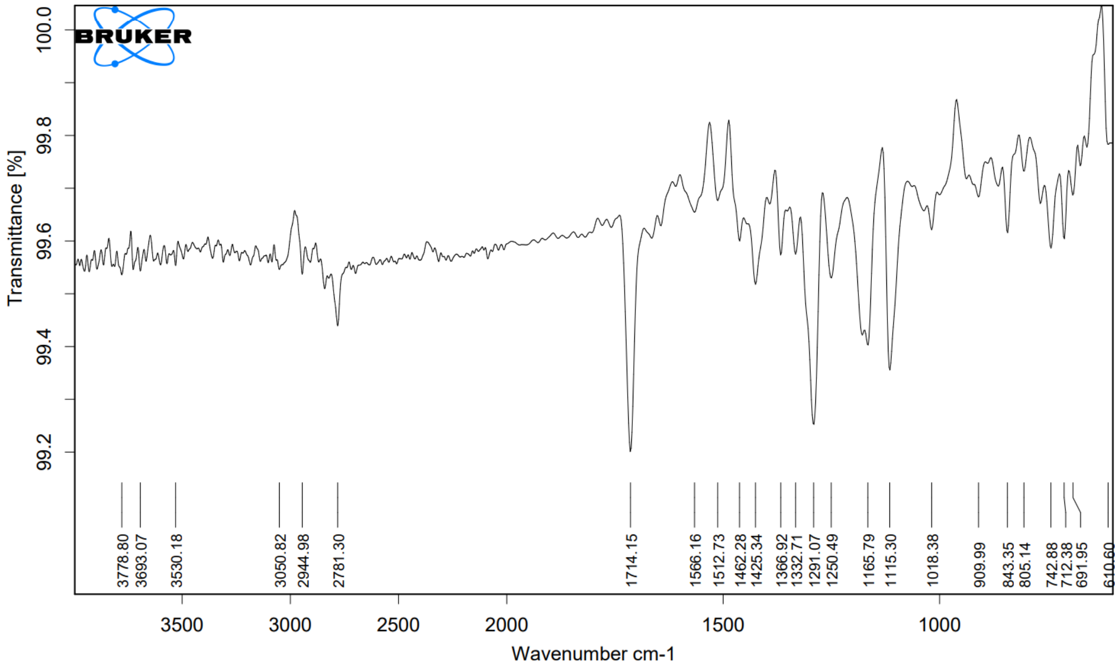

$C_{60}BnCOO^{t}Bu$

^{1}H NMR (400 MHz, $CDCl_3$)

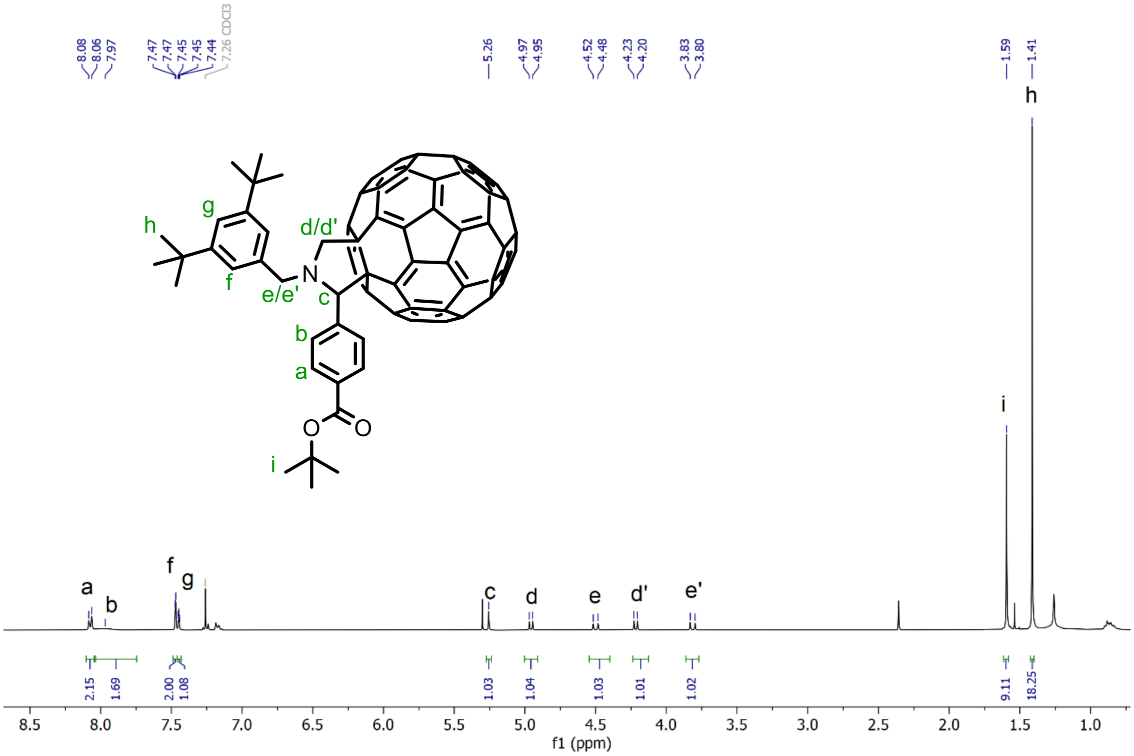

MALDI-TOF

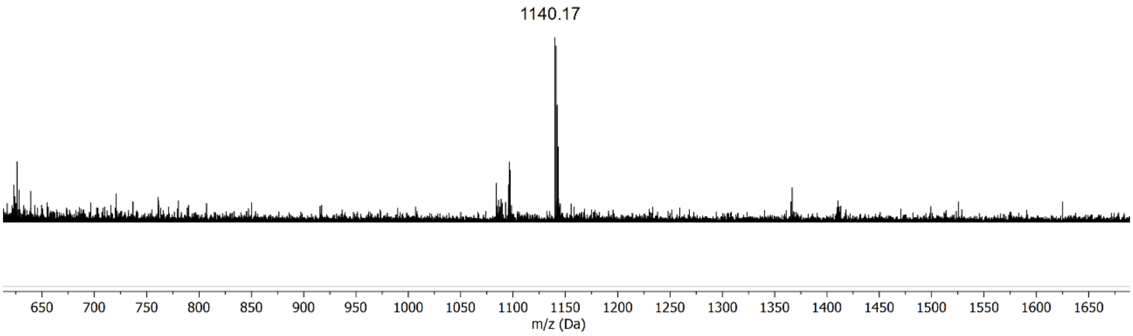

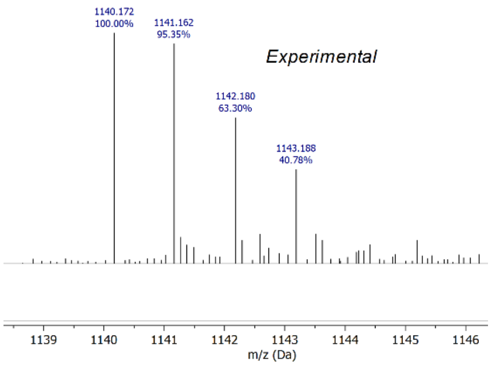

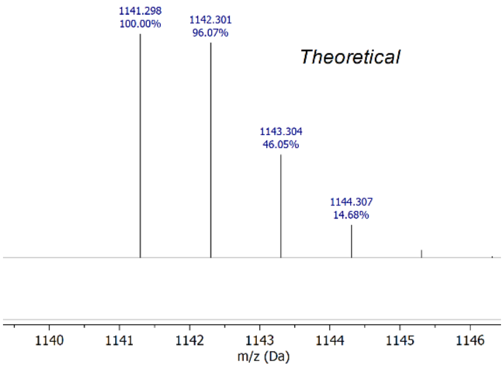

FT-IR

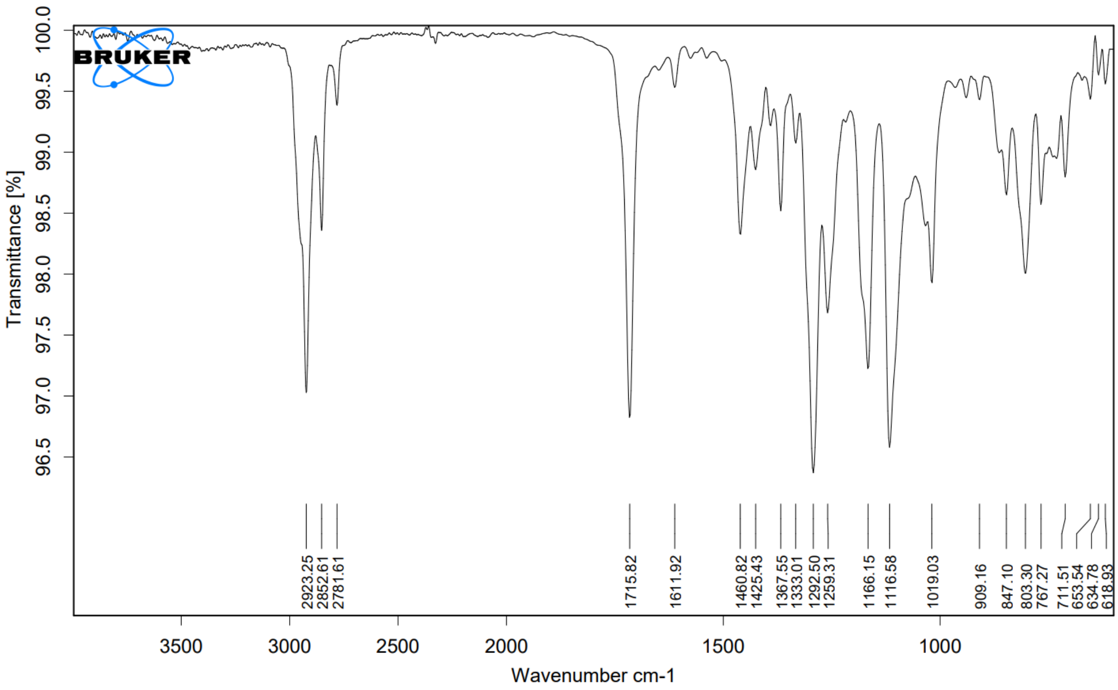

C_{60}BnCOOH

^{1}H NMR (400 MHz, $CDCl_3$)

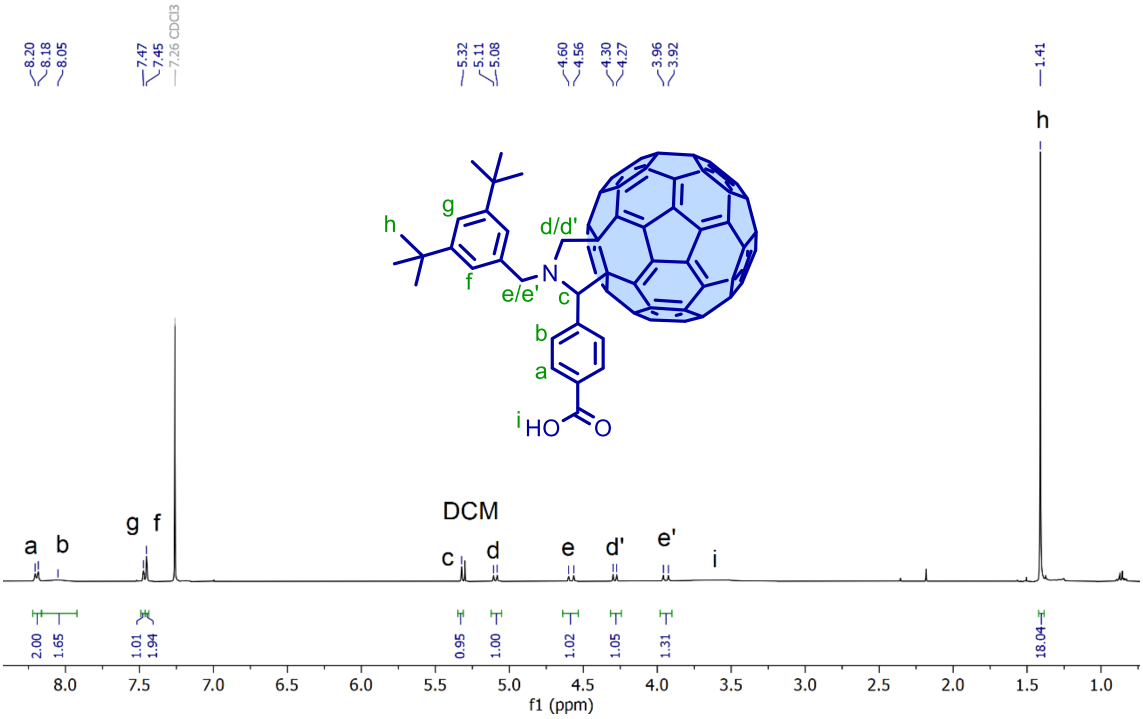

MALDI-TOF

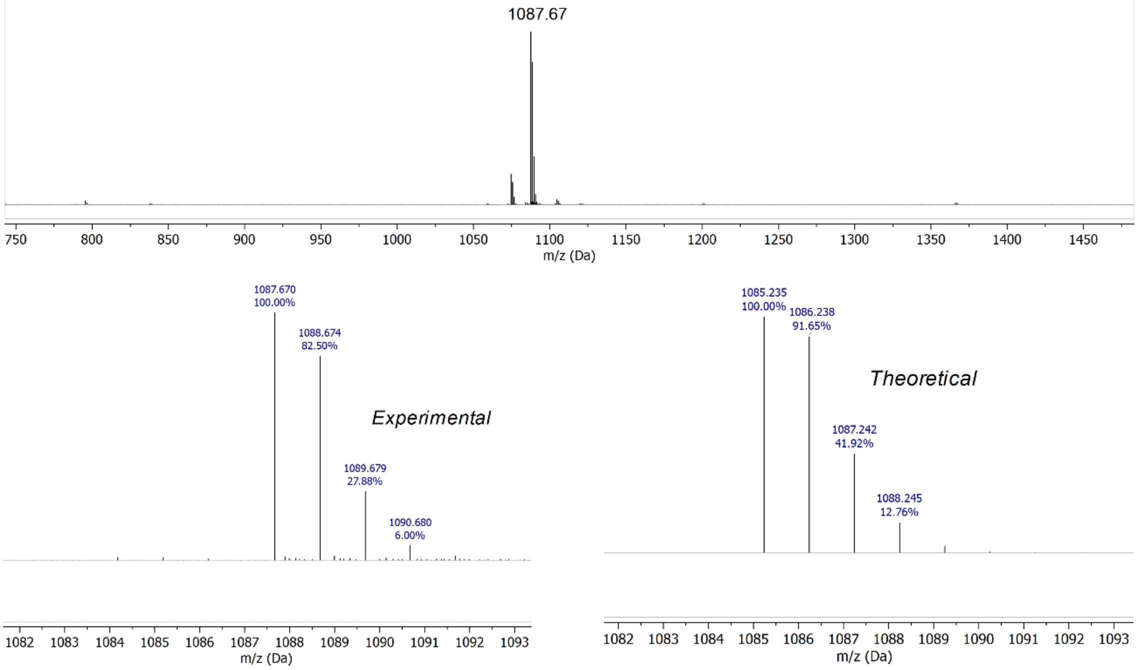

FT-IR

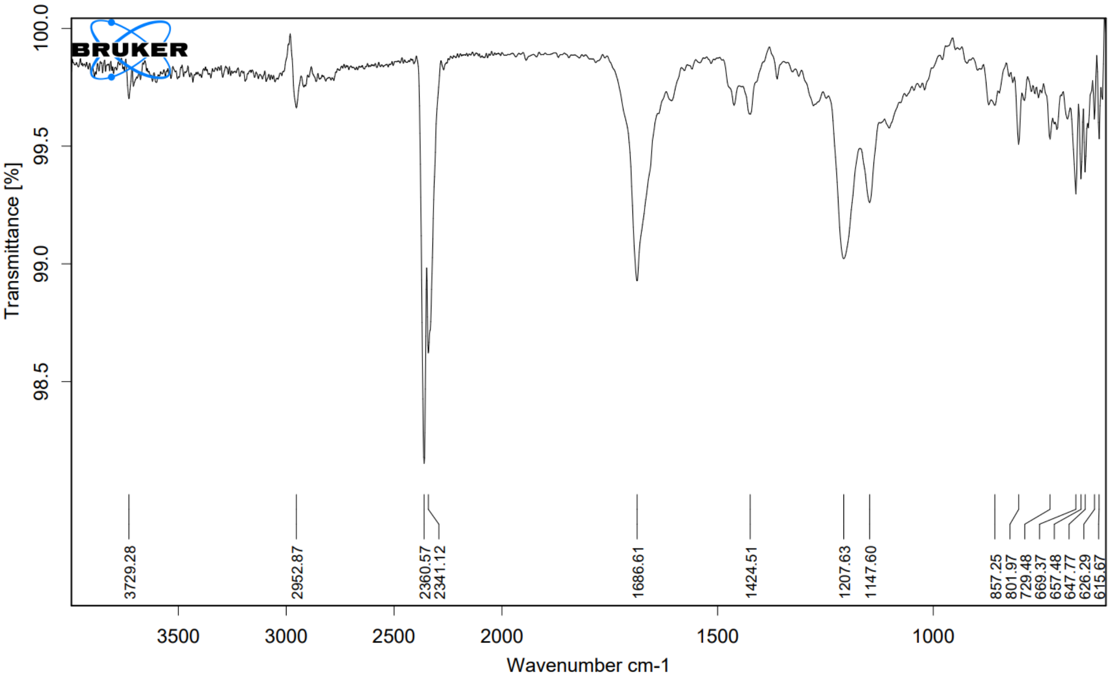

AlPorF$_{20}$C$_{60}$

^{1}H NMR (400 MHz, CDCl$_3$)

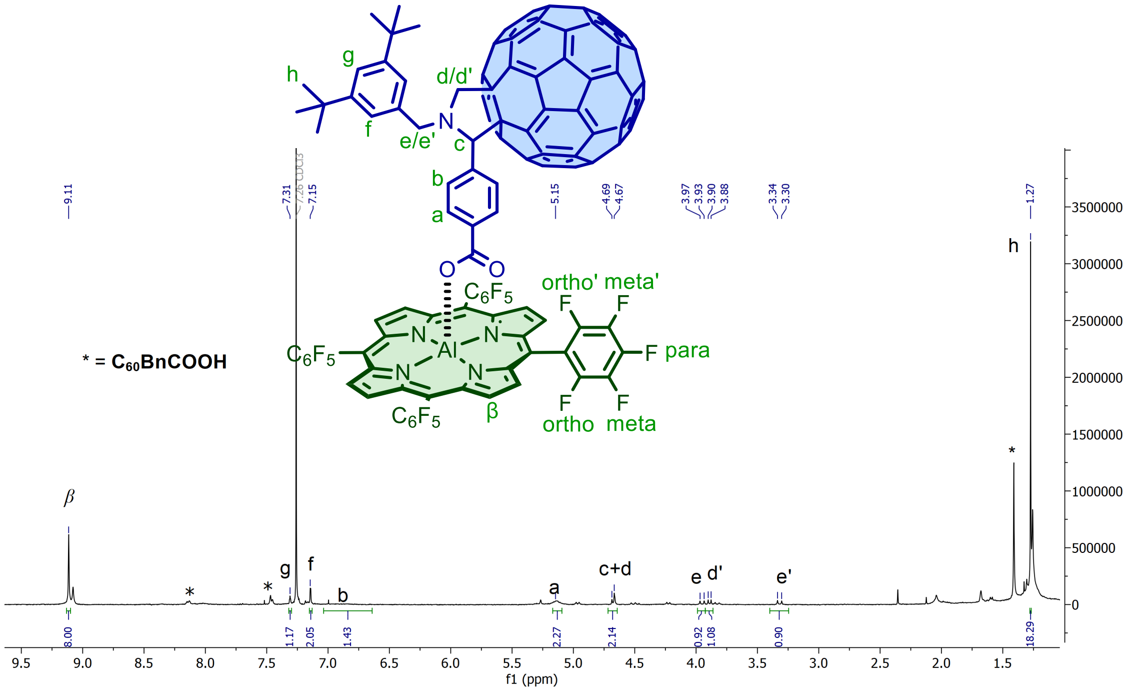

^{19}**F NMR** (376 MHz, $CDCl_3$ / CD_3OD)

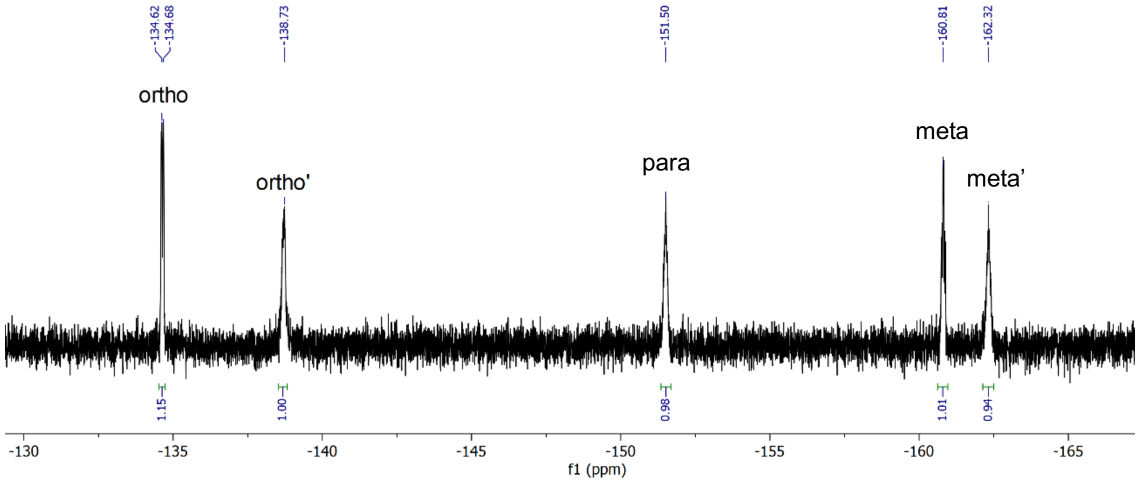

MALDI-TOF

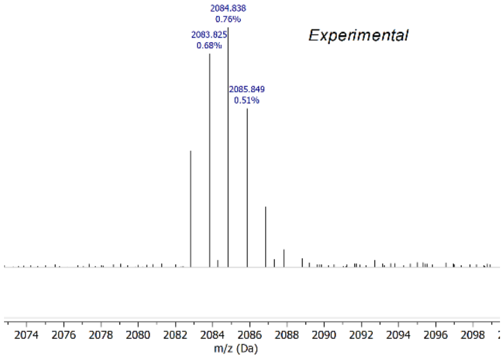

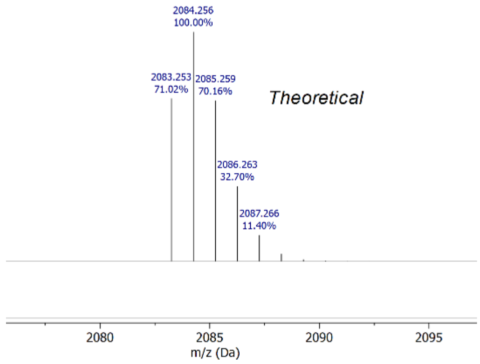

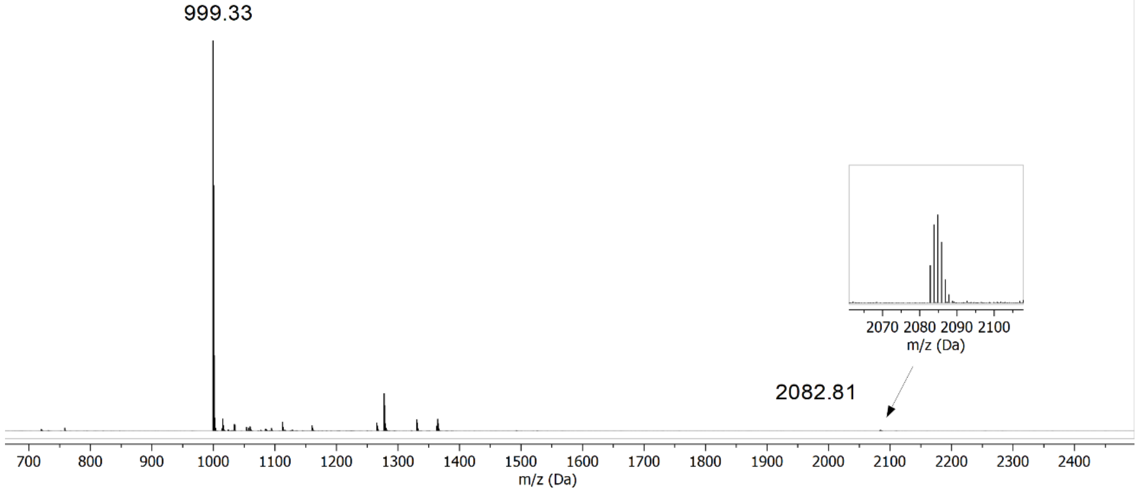

UV-Vis (o-DCB, 293 K)

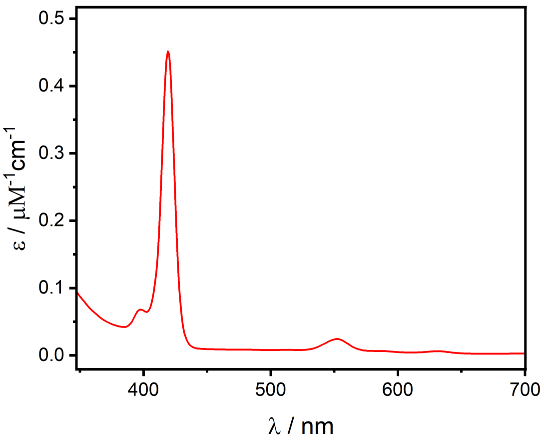

TAAIm-AlPorF$_{20}$C$_{60}$

UV-Vis (o-DCB, 293 K)

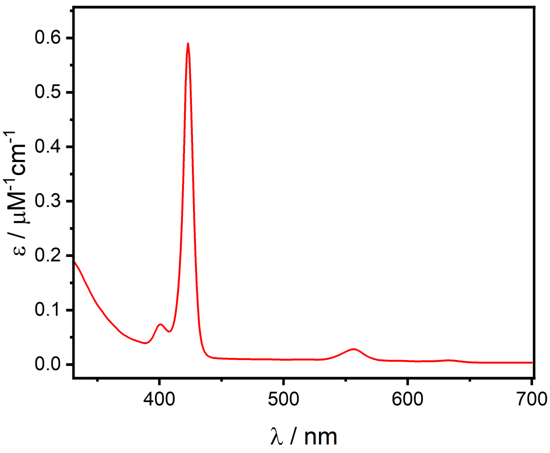

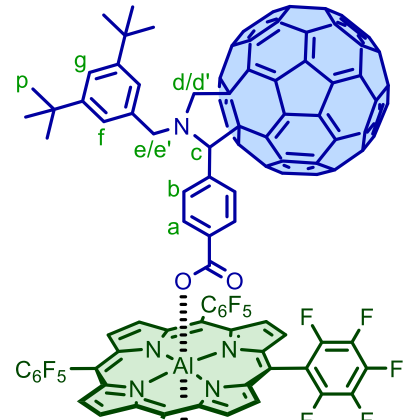

^{1}H NMR (400 MHz, CDCl$_3$)

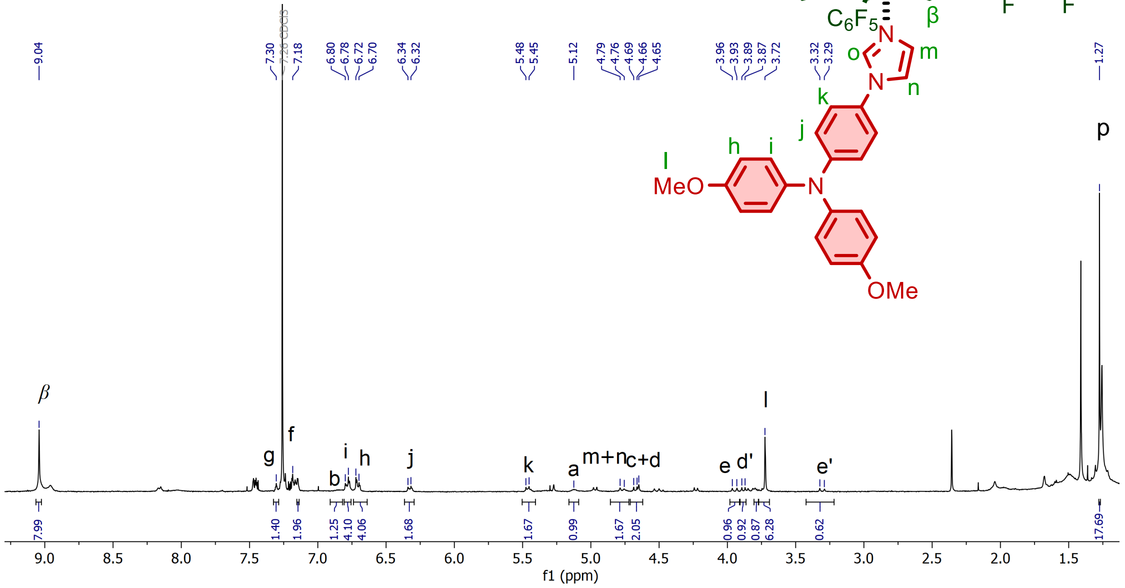

Appendix III: Supporting UV-Vis and trESR Spectra

UV-Vis Titration of AlPor^{t}BuPh with MeIm

o-DCB, 293K

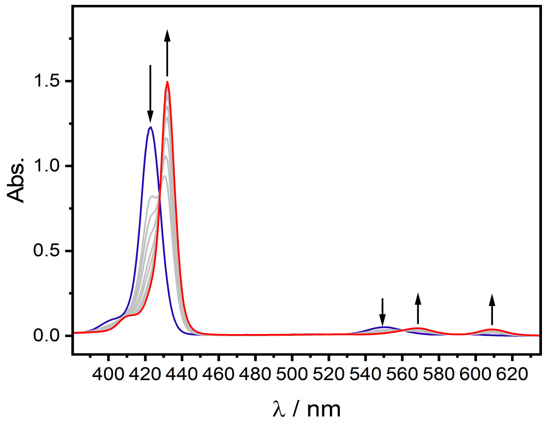

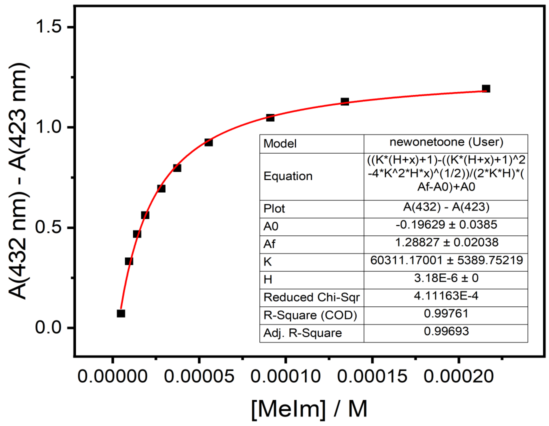

Model	newonetoone (User)
Equation	((K*(H+x)+1)-((K*(H+x)+1)^2 -4*K^2*H*x)^(1/2))/(2*K*H)*(Af-A0)+A0
Plot	A(432) - A(423)
A0	-0.19629 ± 0.0385
Af	1.28827 ± 0.02038
K	60311.17001 ± 5389.75219
H	3.18E-6 ± 0
Reduced Chi-Sqr	4.11163E-4
R-Square (COD)	0.99761
Adj. R-Square	0.99693

UV-Vis Titration of AlPorF$_{20}$Ph with py

o-DCB, 293K

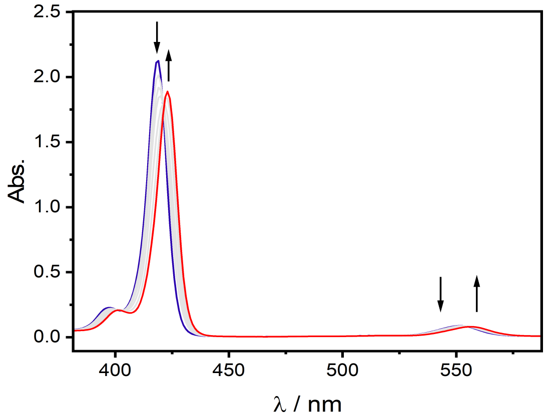

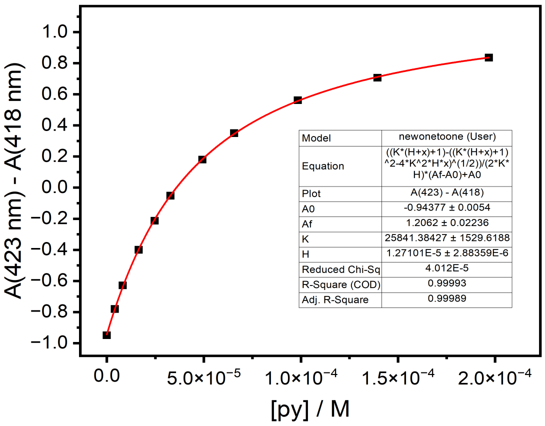

Model	newonetoone (User)
Equation	((K*(H+x)+1)-((K*(H+x)+1) ^2-4*K^2*H*x)^(1/2))/(2*K* H)*(Af-A0)+A0
Plot	A(423) - A(418)
A0	-0.94377 ± 0.0054
Af	1.2062 ± 0.02236
K	25841.38427 ± 1529.6188
H	1.27101E-5 ± 2.88359E-6
Reduced Chi-Sq	4.012E-5
R-Square (COD)	0.99993
Adj. R-Square	0.99989

UV-Vis Titration of AlPorF$_{20}$Ph with MeIm

o-DCB, 293K

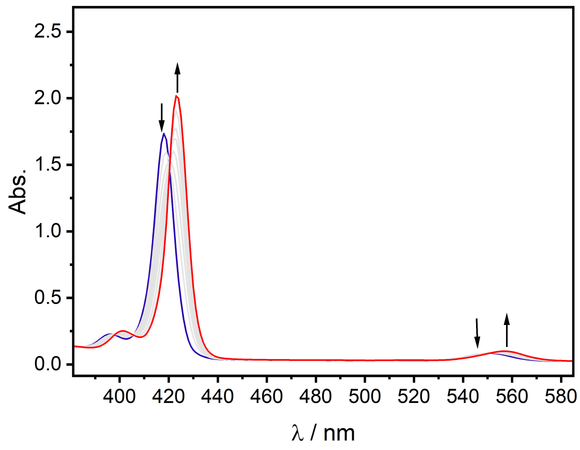

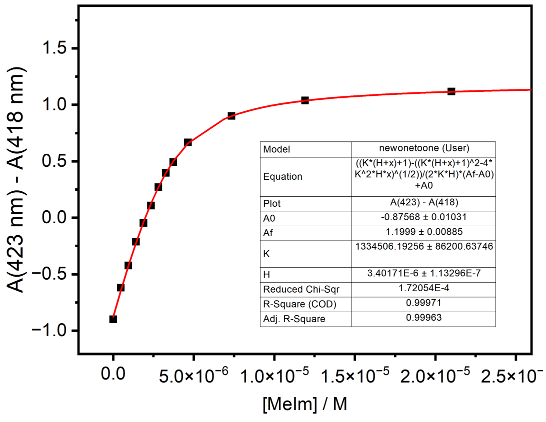

Model	newonetoone (User)
Equation	((K*(H+x)+1)-((K*(H+x)+1)^2-4* K^2*H*x)^(1/2))/(2*K*H)*(Af-A0) +A0
Plot	A(423) - A(418)
A0	-0.87568 ± 0.01031
Af	1.1999 ± 0.00885
K	1334506.19256 ± 86200.63746
H	3.40171E-6 ± 1.13296E-7
Reduced Chi-Sqr	1.72054E-4
R-Square (COD)	0.99971
Adj. R-Square	0.99963

trESR Spectrum of AlPorPh (best fit obtained with single triplet simulation)

Experimental conditions are the same as in Figure 4.4

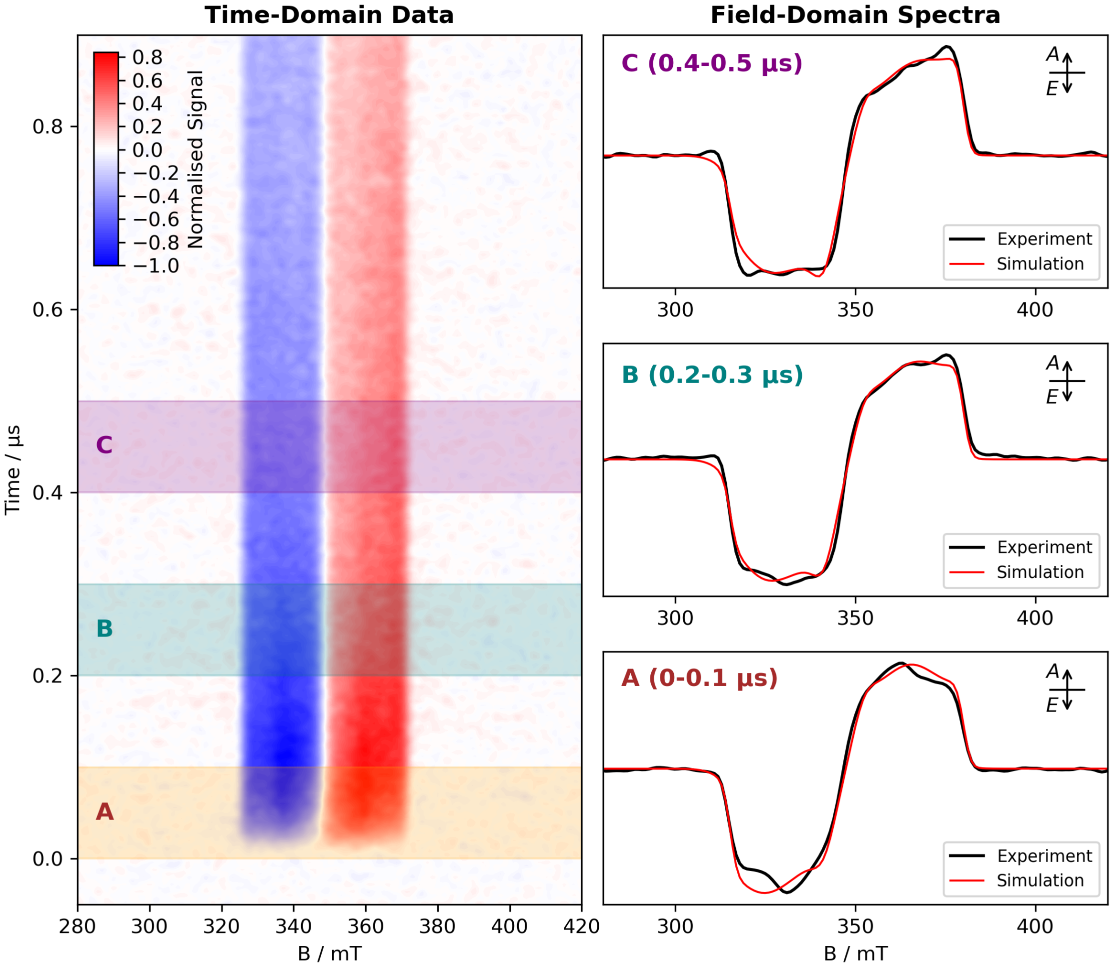

Component	*D* / MHz	*E* / *D*	$P_X : P_Y : P_Z$
Single Porphyrin Triplet	+904	+0.22	0.22 : 0 : 0.78

trESR Spectrum of AlPorF$_{20}$Ph (best fit obtained with single triplet simulation)

Experimental conditions are the same as in Figure 4.6

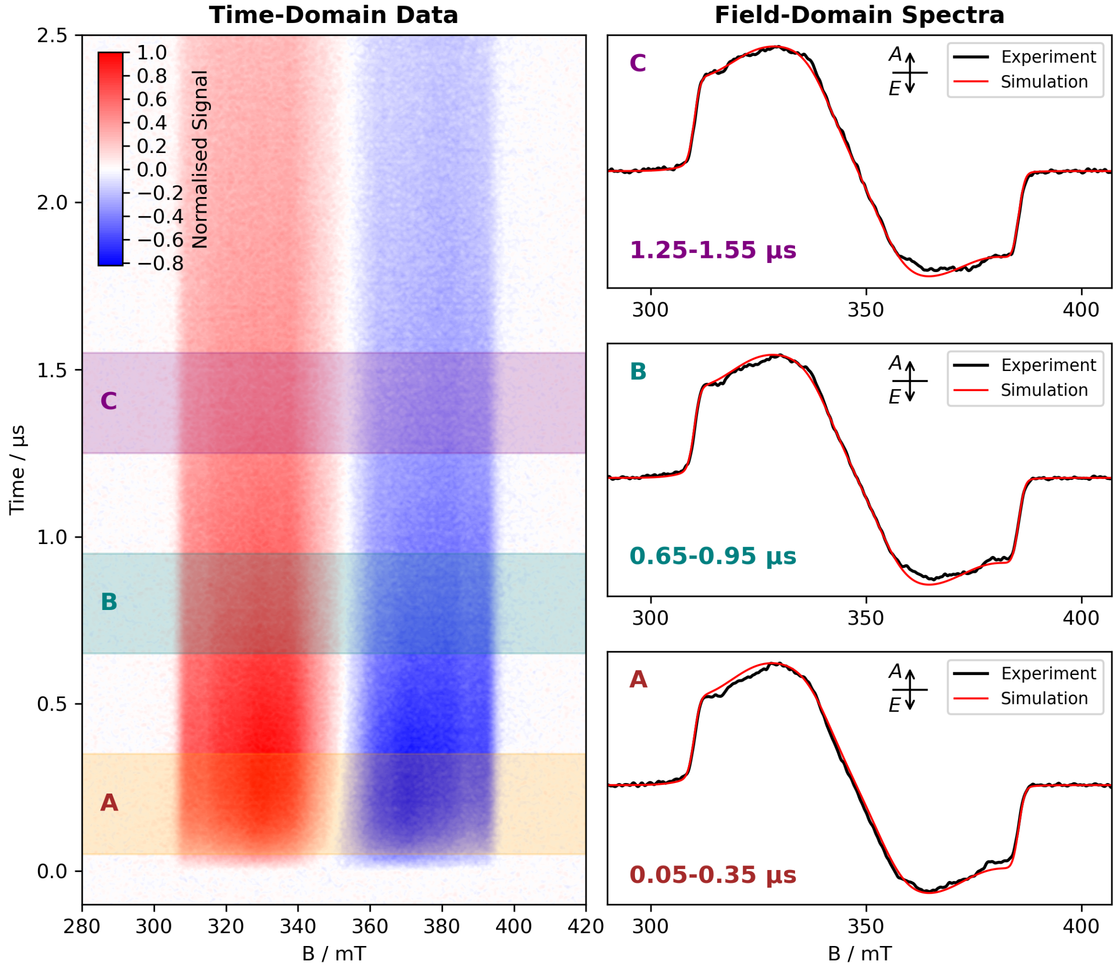

Component	D / MHz	E / D	$P_X : P_Y : P_Z$
Single Porphyrin Triplet	+1047	+0.14	0.53 : 0.47 : 0